MASTER THESIS

Nanoimprint meets microfluidics: development of high-resolution metal wires from nanoparticle ink filled capillaries

Author	**Bc. Barbora Křivová**
Study programme	Nanotechnology
Supervisor of the master thesis	Mgr. Milan Vůjtek, Ph.D.
Specialist consultant	Dr. Helmut Schift

Olomouc 2019

Declaration of originality

I declare that this thesis is my own work and that it contains literature which I cite in the list of Bibliography.

In Olomouc, May 20, 2019

. . . .

Acknowledgements

Bibliografická identifikace

Jméno a příjmení autora	Bc. Barbora Křivová
Název práce	Spojení nanoimprintu s mikrofluidikou: Vývoj vodičů připravených pomocí plnění kapilár inkoustem obsahujícím nanočástice
Typ práce	Diplomová
Pracoviště	Katedra experimentální fyziky
	Paul Scherrer Institut (PSI), Švýcarsko
Vedoucí práce	Mgr. Milan Vůjtek, Ph.D.
Specialista konzultant	Dr. Helmut Schift
Rok obhajoby práce	2019

Abstrakt — V této diplomové práci je prezentován nový úsporný způsob přípravy kovových vodivých drátků v sub-mikrometrovém měřítku. Předložený proces je složen z metod, které jsou založeny na aplikaci inkoustu s obsahem nanočástic stříbra na předem vzorovaný polymerní substrát. Drátky jsou připraveny pomocí geometrického vymezení kapilárního plnění, které umožňuje rozlišení za hranicí rozlišení dosažitelného typickými inkoustovými technikami. Metody spin-coatingu a aerosol jet printingu, které jsou obvykle používány pro jiné účely, jsou diskutovány vzhledem k povrchovému omezení inkoustového šíření a tím přípravě drátků, které mohou být využity pro výrobu elektrodových řad a optických mřížek. Dále jsou diskutovány dvě metody spékání s ohledem na dodatečné zmenšení rozměrů struktur, ale zároveň udržení vysoké vodivosti. Navrhnutý proces je úsporný a univerzální způsob přípravy tištěné elektroniky, čímž se stává kandidátem pro budoucí techniku přípravy nanoelektroniky.

Klíčová slova	nanoimprint, mikrofluidika, inkoust obsahující nanočástice
Počet stran	85
Jazyk	anglický

Bibliographical identification

Autor's first name and surname	Bc. Barbora Křivová
Title	Nanoimprint meets microfluidics: development of high-resolution metal wires from nanoparticle ink filled capillaries
Type of thesis	Master
Department	Department of Experimental Physics
	Paul Scherrer Institut (PSI), Switzerland
Supervisor of the master thesis	Mgr. Milan Vůjtek, Ph.D.
Specialist consultant	Dr. Helmut Schift
The year of presentation	2019
Abstract	A novel process for obtaining low-cost metal conductive wires in sub-micrometer range is presented in this diploma thesis. The methods are based on applying nanoparticle-based silver inks on pre-patterned polymer substrates, and wire fabrication is beyond the typical resolution of inking techniques by capillary filling and geometrical confinement. The method of spin-coating and aerosol jet printing, usually used for different purposes, are discussed with the respect to surface confinement and wire fabrication for manufacturing of electrode arrays and optical gratings. Two sintering post-processes are described to further decrease the structure dimensions while maintaining high wire conductivity. Thus, a low-cost and versatile process for printed electronics fabrication is designed as a candidate for future nanoelectronics production.
Keywords	nanoimprint, microfluidics, nanoparticle ink
Number of pages	85
Language	English

Contents

Introduction

Due to the trend of miniaturization and enhanced complexity of electronics as predicted by Moore's law, the objective of nowadays research is to optimize and develop fabrication processes with the emphasis on efficiency, up-scalability of a technique and range of suitable depositing materials. Therefore, there is a rapidly growing interest for low-cost manufacturing technologies which would replace lithography-based approaches (photolithography, electron lithography, nanoimprint lithography) expensive for high volume manufacturing. Therefore, additive techniques such as gravure printing and inkjet printing are favoured because they avoid vacuum processes, but suffer from limited resolution often much larger than 20 µm. Novel ink writing techniques such as aerosol jet printing are non-contact and locally addressable but continuous techniques, and enable higher resolution because they enable to pattern a surface without significant spreading. The ability to deposit ink in an almost dry fashion makes it suitable for printing over topography and with sharp boundaries. However, resolutions can barely go below 10 µm that makes them unsuitable for sub-micron patterning.

In this thesis, pre-patterned substrates are used which allow the deposition of ink onto capillaries with defined designs and shapes. By segregation and geometrical confinement, low-resolution deposition technique can be used for the fabrication of wires with structural details equal or even smaller than the size of capillaries. This method even works for uniform coating techniques such as spin-coating which is used for covering large areas and thus is a low cost and up-scalable technique, as long as the liquid ink can be confined and dried within the capillaries in a defined way, avoiding short-cuts between neighbouring wires. Due to their ability to balance the solvent content and deposition parameters, spin-coating and aerosol jet printing are similar in their behaviour to control the confinement within capillaries.

The aim of the present diploma thesis is to provide novel utilization of the two fabrication techniques with their comparison of usability for fabrication of sub-micrometer range conductive metal structures. Spin-coating and aerosol jet printing will be applied for silver nanoparticle-based ink deposition on pre-patterned substrates.

Pre-patterned substrates with specific sub-micrometer topography, made by V-grooves separated by plateaus, should not only allow resolution much smaller than the resolution of the applied additive processes and even the V-grooves dimensions, but also control over the location and shape of the fabricated structure. Moreover, two sintering postprocesses will be tested and discussed as methods for further tuning of resolution and conductivity of fabricated structures: conventional thermal sintering and flash light sintering which additionally support polymer substrate flattening which increases the product application.

Results from the diploma thesis were already published in two articles and presented with a poster on the 17th conference on Nanoimprint and Nanoprint Technologies in Portugal. [1, 2]

1 Theoretical Part

1.1 Flexible Electronics

Printed flexible electronics, characterized by its resistance to bending, twisting and folding, is one of the major and important aspects of modern electronics. The ability of new mechanical properties has the potential to extend and replace the classical silicone-based components for low-cost and large-area devices with many new promising applications. [3] These elements can cover novel applications in areas such as environmental and biological monitoring [4–6], energy harvesting and storage, flexible displays, smart textiles and radio frequency identification. [3, 7] Specifically, stretchable wearable sensors continuously monitoring health indicators [8, 9], electronic skin, self-powered devices, solar cells and photovoltaic devices [10], printed organic thin-film transistors [11, 12], supercapacitors [13], fuel cells, triboelectric and thermoelectric generators are mostly investigated. [9]

To obtain required characteristics and performance of the printed device, the selection of an optimal conductive ink, flexible substrate and printing method is of main importance and have to be optimized with the emphasis on device application. [8, 14]

1.2 Inks for Printed Electronics

While applying specific fabrication technique usually specific ink properties are required. Generally, printing inks should have good printability, ability of high resolution printing, good adhesion to deposition substrate, minimum printer maintenance and long shelf life. Therefore, the important physical properties as viscosity, surface tension and its wettability of specific substrate should be considered during ink selection. [14]

Printing inks for flexible electronics fabrication are usually highly diluted dispersions containing conductive components. These main functional components depending on the used material can be in the form of metal nanoparticles (Ag, Au, Cu, Al, Ni), nanowires (Ag), sheets (graphene), single or multi-walled nanotubes (C), conductive polymers as well as organometallic compounds. Also, metal precursors converted into conductive compounds by post-printing process can be applied. Other special requirements resulting from the printing technique are applied in the form of functional components. For example, in the case of printing head or nozzle utilization, the specific compound size is limited due to probability of the printing device clogging. Therefore, smaller particles with average particle diameter of $30-50\,\mathrm{nm}$ are mostly preferred. [14–16]

Considering product applications in flexible electronics, the main physical properties such as conductivity, optical transparency, and stability of the printed pattern to bending and twisting has to be determined. Discussing particle containing inks, highly conductive metals such as gold (electrical conductivity $\sigma = 4.42 \cdot 10^{-6}\,\Omega^{-1} \cdot \mathrm{cm}^{-1}$) and

mainly silver ($\sigma = 6.3 \cdot 10^{-6}\,\Omega^{-1} \cdot cm^{-1}$) are the mostly used materials for electronics printing. There is an objection to replace them for Cu ($\sigma = 5.96 \cdot 10^{-6}\,\Omega^{-1} \cdot cm^{-1}$), Al ($\sigma = 3.78 \cdot 10^{-6}\,\Omega^{-1} \cdot cm^{-1}$) or Ni ($\sigma = 1.43 \cdot 10^{-6}\,\Omega^{-1} \cdot cm^{-1}$) due to the high price of the noble metals. However, strong oxidation decreases the final conductivity. Long-term stability can be preserved only by suitable ambient conditions i.e. the fabrication process under an inert atmosphere; or by individual particle coating with capping agent (generally alkanethiols, long chain carboxylic acids, polymers) or other metal and thus forming core–shell particles. [14]

Low viscosity metal-based inks have to possess long-term stability also in the dispersion where possible aggregation and sedimentation can occur. Since the selected stabilizer and the composition of the liquid vehicle of the ink affect the shelf life and the overall performance of the ink, their selection is of a great importance. Nevertheless, the stabilizer usually composed of organics acts as an electrical insulator and has to be removed in order to enable metal sintering into a conductive metallic structure. [14]

1.3 Flexible Substrates

The ideal substrate for printed conductive pattern is low cost, unlimitedly flexible, bendable, foldable and conformable to uneven surfaces with negligible variation in conductivity. [8] Substrates that possess such properties (i.e. polymers, paper and textile fabrics) strongly affect the printed device performance also by their optical transparency, electrical and structural characteristics in complex which determine their utilization. [14]

Polymers are widely used for flexible electronic fabrication due to their low weight and suitability for large-scale manufacturing. They possess high stability moreover supported by water and oxidation resistance which allows their utilization under several conditions. The main representatives are polyimide (PI), polyethylene terephthalate (PET), polyethylene naphthalate (PEN), polycarbonate (PC), poly(ether sulfone) (PES), polyarylate (PAR) and poly(methyl methacrylate) (PMMA). PMMA is used in this work for the suitability for imprint and its thermal properties. [5, 6, 14]

Polymer materials are excellent substrates for electronics devices due to their easy processing and mechanical properties as well. One of the most promising polymer properties is stretchability which was reported for non-conductive polymers such as poly(dimethylsiloxane) (PDMS), polyurethanes (PU) and multiblock copolymer styrene-–ethylene–butadiene–styrene (SEBS). Recently, conductive polymers and composites based on poly(3,4-ethylenedioxythiophene) (PEDOT) with poly(styrene sulfonate) (PEDOT:PSS) were also reported. The conductivity together with high degree of mechanical deformability allows intimate contact with their surrounding and thus highly enhances the efficiency of sensing. Therefore, PEDOT is mainly discussed in biomedicine for continuous nontoxic sensing and reducing scaring due to possible tunability of its composition. The initial stretchability is only up to around $10\,\%$. However, many strategies on the enhancing have been recorded. [9]

The main challenge of polymer treatment is represented by their low thermal stability. The glass-transition temperature (T_g) of most common polymer films is less

than 150 °C, e.g. 60 – 80 °C for PET, 120 – 125 °C for PEN, 140 – 150 °C for PC and 100 – 120 °C for PMMA which results in the irreversible deformation or damage of printed device under high working temperatures i.e. due to high current applications or sintering post-process. [14, 17, 18]

Paper is another low-cost substrate allowing excellent printing compatibility. However, special chemical pre-printing treatment has to be provided to suppress numerous undesired paper characteristics e.g. water and solvent absorption, porosity and unfavourable surface energy. The manufacturing process enables paper to obtain additional functionalities such as low gas permeability, transparency or superhydrophobicity. Nevertheless, paper substrates are also not capable of post-printing processing with temperatures higher than 150 °C. [14, 19]

The third mostly used substrates are textiles. The composition of numerous individual fibers makes the binging of printed structure on the deposition substrate significantly difficult. Moreover, the print quality is strongly limited by the surface roughness and capillary forces in woven fabrics which is crucial for printing of continuous conductive circuits. On the other hand, fibre composition allows high porosity for easy water absorption and air transmission which supports their washability and interaction with surrounding. Therefore, their highest importance occurs in the field of clothing with integrated electronics i.e. electronic textile, smart textile or wearable electronics due to possible communication with human skin. [8, 14]

1.4   Printing Techniques for Flexible Electronics

Due to a pressure on electronics miniaturization, the nowadays research is oriented on invention of modern techniques or pushing the limits of currently known technologies to obtain high resolution electrical elements. Conventional electronic device manufacturing is mainly based on traditional methods such as electroless plating and photolithography. [20] These usually subtractive techniques are multi-stage processes generally generating a large amount of wasted materials which require high-cost equipment and often application of environmentally undesirable chemicals. [14]

Therefore, additive manufacturing, presenting low cost and up-scalable techniques based on material addition to form the product structure, is being intensively investigated for printed electronics. Techniques represented by this concept are uncomplicated two step processes which include printing and curing of the printed patterns. Their connection to micro-electronics presents the potential to revolutionize the conventional fabrication methods and offers fast manufacturing of customized objects with tailored product design and thus to fulfill the request of individual specific applications. [14, 21]

The additive printing of microelectronics is based on various solid and liquid-based technologies. While usually a functional material in the form of a powder (plastic, ceramic, metal) is applied and converted into a continuous solid layer by selective layer by layer laser sintering (SLS), electron beam melting (EBM) etc. in solid-based methods; liquid-phase patterning technologies gained recently more interest. For example, a very famous technique is 3D printing which provides a 3D objects by layer-by-layer process and thus computer-controlled fabrication along the z-axis. [14, 22]

Inkjet printing, which is a fast, low-cost non-contact and easily up-scalable technique was already modified into higher resolution electrohydrodynamic jet printing, a technique that instead of pneumatic control (used in ink jet printing) uses electric fields to create a fluid flow necessary to deliver ink on a substrate. [6,14] Nevertheless, liquid-phase printing techniques are still largely limited by high requirements on functional inks or the maximal produced features with resolution of less than 10 µm. [11,23]

For example, screen printing is based on pressing an ink through a patterned stencil with a squeegee. The process is compatible with a wide variety of functional inks and substrates. The printing resolution is still highly dependent on the quality of the screen mask which presents the finest possible resolution. Due to low resolution of the lithography emulsion, mesh dimensions restrict the improvement of the mask finer patterns. [23]

On the other hand, gravure, reverse-offset and flexography printing enable high speed, high-resolution patterning (up to 5 µm line width), high throughput and scalability by roll-to-roll deposition. However, many requirements in the form of special ink properties, very precisely engraved printing surface with specific surface tension of printing features are attributed for adequate pattern printing which limits the techniques application. [7,11]

Nevertheless, the opportunity to use self-assembly of molecules or micro- or nanoscopic particles within droplets of deposited ink on pre-patterned substrates is presented in this thesis. The position of ink settlement is limited by the substrate pattern by which fabricated shape can be controlled and the resolution enhanced. There is no need of specific technique for ink deposition, thus almost any chosen non-contact technique can overcome the ink or substrate requirements.

The core of the idea using particle self-assembly on pre-patterned substrate by spin-coating process is demonstrated in Figure 1.1. Diluted ink containing micro or nanoscopic particles is deposited, spin-coated on pre-patterned substrate. The technique allows the deposition of ink by spreading over the whole substrate. However, the deposited ink is partly withheld in the pre-patterned structure where the particles self-assemble. In this case, a polymer substrate with V-groove profile was designed for improving particle sedimentation properties due to tilted sidewalls. The difference is presented by splitting of the ink by Λ-ridges into lines with a V-groove profile. During solvent evaporation, the smoothness of the side walls supports particle sedimentation to the bottom of the V-groove and thus formation of a line due to the pattern structure. Nanoparticles start to merge and agglomerate in continuous lines which are much thinner than the original V-groove width due to the solvent evaporation. Depending on the particle concentration in the solution, line width can be reduced even to the sub-100 nm range scale.
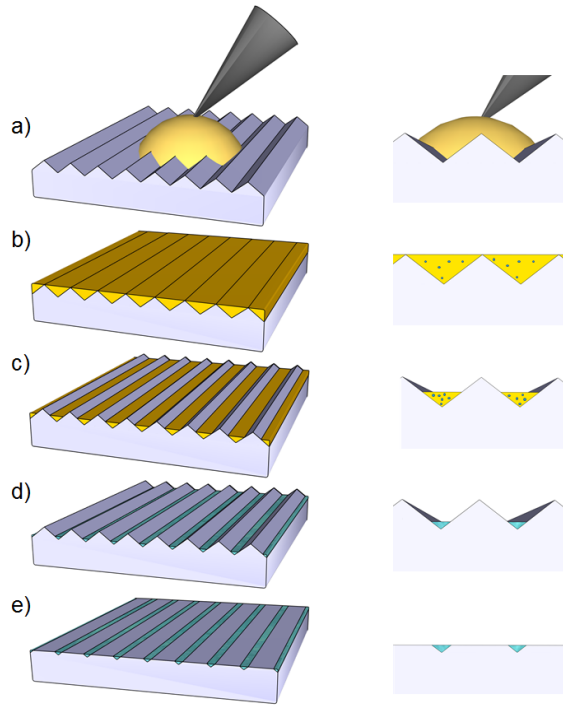
Figure 1.1: *Schematics of self-forming metal lines prepared by spin-coating on "PMMA 1S" substrate. On the left side, the overall view is shown, on the right side magnified cross-section of the patterned substrate is presented. a) Dispensing of silver ink solution on pre-patterned substrate, b) Separation of spin-coated layer into V-grooves, c) Solvent evaporation and volumetric shrinkage due to drying, d) Solution densification and nanoparticle merging, e) Simultaneous sintering of silver wires and substrate thermal reflow. [1]*

During solvent evaporation different transport mechanism forces are involved influencing the assembling process and thus the certain particle positions. Especially, capillary flow, convectional flow, coffee-ring effect and surface energies influencing contact angle between ink and the surface will be involved and all determine the final shape of the deposit during the evaporation. [24] Therefore, the complexity of the fluid dynamics needs to be considered during substrate patterning. By employing self-assembly processes on arbitrary pre-patterned substrates, almost any ordered high-resolution structures in the form of zero-dimensional rings, one-dimensional lines, two dimensional arrays or three-dimensional colloidal assemblies can be achieved. [24, 25]

Similar studies were already published involving self-assembly process. However, the mainly presented technique, ink jet printing based on structure formation by placing separated droplets next to each other, possesses ink viscosity requirements. [2] In this diploma thesis, two new strategies for ink deposition are discussed, spin-coating and aerosol jet printing which, are easily customizable techniques without any requirements on specific ink and substrate properties. [24]

1.5   Aerosol Jet Printing

Aerosol Jet Printing (AJP) is a digital contact-free mask less deposition technique which is mainly used for printing electronics such as interconnect devices, antennas, sensors, flexible electronics etc. [4, 26–29]
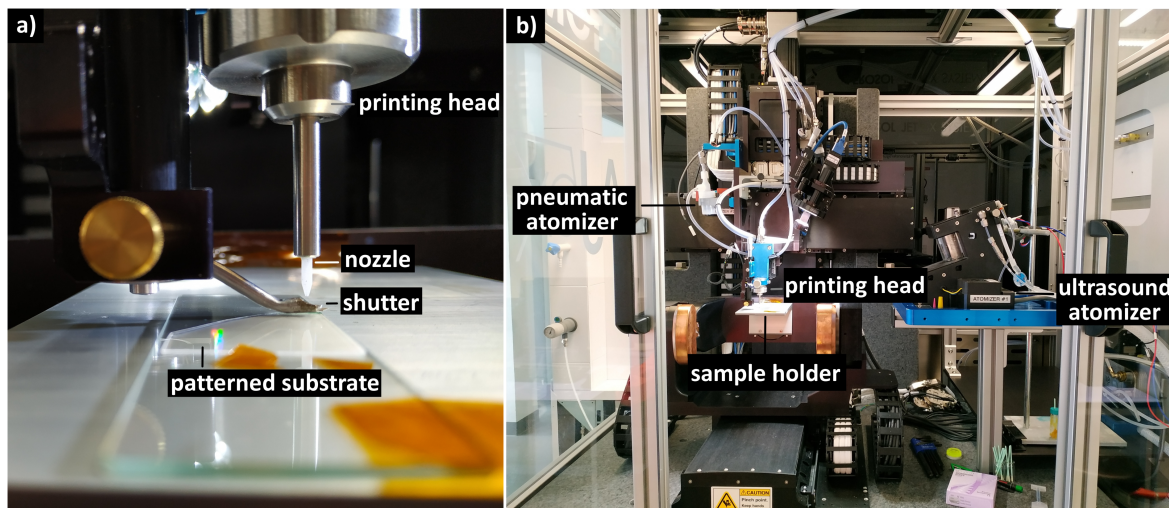

Figure 1.2:   *Image of aerosol jet printing device with a) a detail on the nozzle and substrate arrangement; and b) a general overview of the printing equipment.*

The technique is based on the ink atomization into aerosol (Figure 1.2). Therefore, the only precursor limitation is determined by its ability to be atomized and thus solutions or colloids can be applied without a specific ink viscosity as it is required for other printing techniques of electronics.

Due to ink characteristics, pneumatic or ultrasound atomizer is used for ink atomization. Pneumatic atomization is consisted of smashing a wall with an ink dispersion carried by a high-pressure gas flow. After atomization, the aerosol flows to an aerodynamic separator (also called virtual impactor) which usually follows a pneumatic atomizer. There large sized droplets presented in the aerosol and redundant carrier gas are eliminated for obtaining homogeneous dense aerosol mist. Approximately 30 mL of ink with low vapor pressure (< 0.1 mm Hg), boiling point ($> 180\,°C$) and high viscosity ($0.7 - 1000$ cP (centipoise)) containing particle diameters larger than 50 nm are feasible to be atomized pneumatically. [27] Droplet formation of aerosol mist in ultrasound atomizer is achieved by a transducer which oscillates with a frequency of $1.6 - 2.4$ MHz. Induced ultrasound waves proceed to the vial containing ink, break down the agglomerates and initiate aerosol formation. The advantage of ultrasound atomizer is in its need of only a small amount of ink (approximately 1 mL) which is very suitable for printing of expensive metal inks. Generally, inks with low viscosity ($0.5 - 15$ cP), high vapor pressure (> 0.1 mm Hg), low boiling point ($< 180\,°C$) and containing particle diameters less than 50 nm can be ultrasonically atomized. [3, 27] Each type of atomization is supported by a bubbler which is a container where the carrier gas flow, usually nitrogen, is saturated by passing a bath containing the ink solvent. Saturated carrier

gas flow is then injected into the ink atomizer reservoir. This pre-step helps the proper atomization and inhibits a change of ink chemistry caused due to evaporation. [27]

After atomization, the formed high dense aerosol mist containing approximately 1 to 5 µm sized drops is transferred by an inert gas stream to the printing head. There, an annular sheath gas stream, usually nitrogen or compressed air, is added to surround the aerosol flow and thus improve lateral printing resolution. After the complex of sheath gas and aerosol passes the nozzle, aerosol consisting of small atomized drops is focused and accelerated. Thus, laminar flow determining the line width printing capability is formed. The highest possible resolution which can be obtained with well collimated mist stream results in less than 10 µm line widths. [22,30] The stream remains focused over a distance of 2 to 5 mm from the nozzle to the substrate. [26] However, after the mist reaches the break-down length, a specific distance depending on the gas flow, the laminar flow is changed into the turbulent trajectory and the mist flow is dissipated from the focused stream. The lower stream collimation is, the lower printing quality can be achieved. [30]

Due to the sheath gas flow eliminating the contact between the nozzle and dense aerosol, the equipment clogging and thus interruptions of deposition are inhibited. This is an advantage in comparison with ink jet printing where the clogging of the nozzle is possible even after ink filtration. Multiple nozzle system can be also applied to reach an upscaled technique which makes this technique suitable for mass production. [22] Moreover, the machine can carry multiple ink input devices and hence supports switching between or blending of materials during a printing regime. [26]

Aerosol jet printing is a continuous process and in the case of deposition of separated parts requirement, a shutter is used to protect substrate against deposition by changing its position under the nozzle. Shutter with different shapes depending on a nozzle orifice can be also connected with an exhaustion system to prevent material accumulation. Due to multiple-axis of coordinated print motion, 2D as well as non-planar 3D surfaces can be deposited directly. There is no need of additional substrate which decreases product size, thickness and weight. [22,26]

Aerosol jet printing is often compared with other printing techniques for electronics, mostly with ink jet printing. While AJP enables thinner line deposition with smaller cross-sectional areas, it is not possible to obtained so sharp line edge as in the case of ink jet printing due to chunks of small splats which are always situated on both sides and covering the printed line. [31] On the other side, AJP process allows wider range of ink viscosities, larger standoff distance without losing the capability of high-resolution printing and printing over nonplanar 3D substrates. More detailed comparison between these two techniques is demonstrated in Figure 1.3.

Characteristic	Inkjet printing	Aerosol jet printing (AJP)
Deposition mechanism	Electrostatic	Aerodynamic
Viscosity (cP)	10–20	1–2500
Working distance (mm)	1	1–5
Print speed (mm/s)	Up to 5000	Up to 200
Dynamic accuracy (μm)	N/A	± 6
Line width (μm)	2–200	5–30
Line thickness (nm)	5–500	100–5000
Surface tension (mN/m)	<60	<30
Particle size (nm)	<100	10–700
Metal loading (wt.%)	<20	>60
Droplet size (pl)	1–8	0.001–0.005
Registration (μm)	5–20	5
Feature size (μm)	>30	10–200
Throughput (m^2/s)	0.01–0.5	0.01–0.5
Nozzle diameter (μm)	10–50	100–300

Figure 1.3: *Comparison of ink jet printing and aerosol jet printing characteristics. [27]*

1.6   Spin-coating

Aerosol jet printing is an example of additive technique where the biggest advantage is presented by precise addressability. On the other hand, large area coating technique also without any ink specificity requirement can offer well-defined coating coverage controlled by a few easily customized parameters using significantly less expensive equipment.

Spin-coating is a low cost method conventionally used for the preparation of thin and uniform films. A droplet of coating solution is dispensed on the centre of a flat rotating sample following by its distribution on the entire surface area by centrifugal force. A remaining thin layer on the surface is formed only of a small part of the dispensed solution due to adhesion and viscodynamic forces. In the case of ink dispersion, the solvent from the highly diluted ink is completely evaporated after spin-coating and thus, the surface is partially covered with layer of remained unconnected particles.

Spin-coating is usually used for thin layer deposition mainly of polymers which can afterwards undergo to other post processes e.g. resist application for lithography. [32] But other applications for thin layer preparation of insulators, organic semiconductors, synthetic metals, nanomaterials, transparent conductive oxides etc. are also reported. The thin homogeneous layer deposition allows spin-coating to be a universal technique widely used throughout the semiconductor and nanotechnology industry. [33]

1.7   Sintering Post-processes

For the fabrication of conductive metal wires, the loosely connected nanoparticles need to be transformed into a compact solid mass of material. Therefore, the nanoparticle assembly process is typically followed by sintering where small particles of metal diffuse into grains by different factors. The solvent and organic material that inhibits particle agglomeration are evaporated during heating. Nanoparticles get into contact with each other and neck together in these spots forming a large connected

net. Small particles merge together into larger grains where atom diffusion occurs by coalescence, followed by aggregation, or by Ostwald ripening. [34] The whole complex densifies lowering down the surface energy and transforms into a metallic crystal structure. Generally, a solid conductive wire with a granular appearance is formed (Figure 1.1). [14]

There are different approaches to achieve sintering, e.g. constant heating by hot plate or furnace treatment, flash light sintering (photonic curing) with intense light pulses, low pressure argon plasma sintering, sintering by second to minute microwave pulses, electron beam sintering and chemical sintering using various reducing agents. [14] By chosen technique and controlled sintering conditions, the metal crystallinity with specific grain size and thus the additional line width shrinkage can be achieved. [35–37]

1.7.1   Conventional Thermal Sintering

The conventional thermal sintering is a process based on heating the printed pattern with temperatures below the melting point (T_g) of the bulk metal (typically 250 to 350 °C). Due to high surface-to-volume ratio and enhanced diffusion of surface atoms, nanoparticles have a significant decrease in their melting point down to approximately 100 to 150 °C (depending on the metal form and size). The temperature of sintering is one of the most important factors while choosing a suitable post-process due to influencing the whole structure. Since the substrates for flexible electronics are low cost and thermally fragile, usually paper or polymer, there is always a temperature limitation depending on the thermal decomposition of the substrate. Therefore, the heat must be as low as possible but still high enough for nanoparticle sintering to occur. [14, 36]

However, longer sintering times are necessary during a heat supplement process designed with lower temperature. Due to longer sintering times, atoms moved by diffusion between grains to lower the grain boundary free energies [40] support nanoparticle size growth and thus wire interruption can occur. On the other hand, the total surface area decreases due to atomic diffusion, and even higher resolution wires can be obtained. The possibility to increase wire resolution with the advantage of a good uniformity and the large-area capability of this method make conventional sintering a suitable technique for an industrial production. [16]

1.7.2   Flash Light Annealing (FLA)

Since the sintering of particles is a time-temperature depending process, lower processing temperatures generally mean longer processing times. Flash lamp annealing is an alternative method for achieving sintering postprocess using short light pulses from xenon flash lamp with a low thermal influence of sintered structure. [35]

The process is based on the physical properties of nanoparticles. Due to size limitation, the absorption wavelengths of metal nanoparticles are shifted and therefore highly absorptive in the wavelength range of the emitting source. Very high surface-to-volume ratio admits particle sintering even with lower intensity of the light source. Therefore,

there is no need of an expensive laser equipment. After absorption of radiation and thus particle heating, the thermal energy from particles is transferred within a few milliseconds to attain a thermal equilibrium with the substrate. The shorter duration of light pulse, shorter than it is necessary for achieving thermal equilibration between the particles and the substrate, allows nanoparticle sintering before transferring of high amount energy to the substrate. Since the particles are preferentially heated, it broadcast curing heats only to the deposited pattern. The substrate and surrounding components remain cool which makes this technology ideal for a printed pattern on a low temperature substrate. [36]

Due to the short duration pulse, less than $1\,\mathrm{ms}$, FLA process can be compatible with high-speed printing processes without need of offline curing. However, the disadvantage of FLA is the small area irradiation and therefore step-by-step processing is still required for larger domains. [1, 35, 36]

2 Experimental Part

2.1 Chemicals

2.1.1 Silver Nanoparticle Inks

- Smart'Ink S-CS 01130 (Silver "light" ink (AgL)), Genes'Ink

- Particle content: $(20 \pm 1)\,\text{w/w}\,\%\,\text{NPs}$ (equal to $\sim$1.4 v/v %, see [2])

- Carrier vehicle ("solvent"): alcohol and alcane

- Shelf time: 3 months

- Contact angle: $(5.8 \pm 0.3)°$ (measured on flat surface of PMMA substrate)

- Smart'Ink S-CS 31506 (Silver "dense" ink (AgD)), Genes'Ink

- Particle content: $(55 \pm 5)\,\text{w/w}\,\%\,\text{NPs}$ (equal to $\sim$10 v/v %, see [2]) with the particle diameter $(49 \pm 15)\,\text{nm}$ (Figure 2.1). Elliptical nanoparticles with the longest diameter of 122 nm were captured by SEM.

- Carrier vehicle ("solvent"): alcohol and glycol

- Shelf time: 3 months

- Contact angle: $(14.8 \pm 1.3)°$ (measured on flat surface of PMMA substrate)
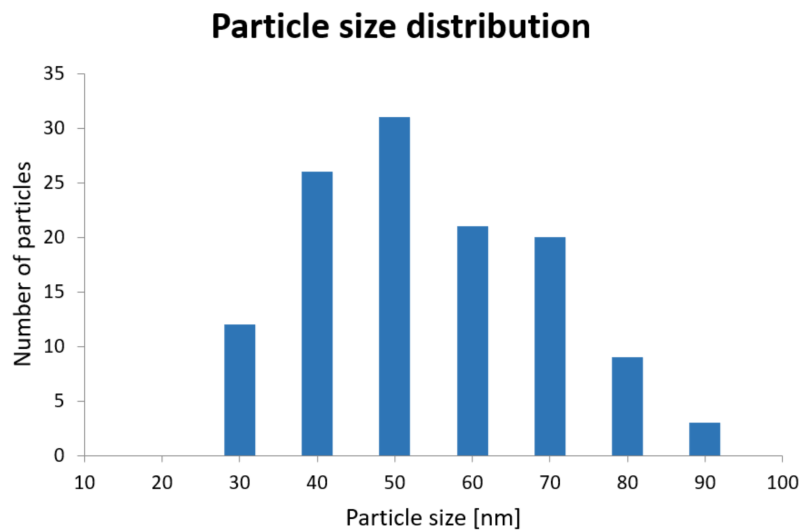

Figure 2.1: *Particle size distribution of AgD silver ink.*

2.1.2 Other Chemicals

2-heptane, trimethyl pentane (TMP), decane, penthanol, ethanol, IPA, 2-buthanol, distilled water

2.2 Preparation of Ink Solution

Silver ink has to be stored in a cold $(0-5)°C$ and dry place to prolong ink shelf time and to prevent possible nanoparticle agglomeration. Special procedure about ink storage needs to be followed accordingly to data sheets. Before each use, the ink is removed from the fridge and left for 10 min at room temperature. Immersion in an ultrasonic bath for 5 min follows to break down possible agglomerates. Ink dilution is made by adding of solvent to achieve required ratio (i.e. 1:49 means one volume unit of silver ink is diluted with 49 units of solvent). The solution is then filtrated through 0.45 µm filter to eliminate larger silver clusters which could clog a nozzle during ink jet printing or simply interrupt the fabricated wires. Homogeneity of solution is achieved by 1 min shaking on a vortex device.

2.3 Substrates

2.3.1 Substrate Patterning

The substrate which will later serve as a stamp for hot embossing was pretreated as followed. First, 100 nm Si_3N_4 layer was applied by low pressure chemical vapor deposition (LPCVD) on a silicon wafer. A negative resist (AZ nLOF 2020, Micro-Chemicals) was spin-coated on the wafers and prebaked at 110 °C for 90 s. Then, the pattern from a mask containing 2 µm wide 4 µm period lines was transferred by contact photolithography (wavelength 365 nm) in a SÜSS MA6 mask aligner. Modified substrate was post-baked at 110 °C for 120 s following by reactive ion etching (RIE) in a mixture of O_2 with flow of 5 sccm, and CHF_3 with flow of 40 sccm with etching rate of 100 nm/min. Residual resist was removed by wet development. Potassium hydroxide (KOH) anisotropic etching at temperature of 80 °C for 18 min was applied following by the Si_3N_4 layer removing by RIE.

Silicon wafer with 3.2 µm wide and 2.3 µm deep V-groove profile containing an angle of 54°44′ between the ⟨100⟩ and the ⟨111⟩ plane; and small 200 nm wide plateau between separated V-grooves was obtained and used for hot embossing. Prepared stamp was transferred by UV-assisted imprint into OrmoStamp applied on glass wafer forming replicas with Λ-ridges molding from original V-grooves. Finally, a PMMA 2S substrate with V-groove profile was achieved by hot embossing of this replica into a 2 µm thick poly(methyl methacrylate) (PMMA) layer ($M_w = 120$ kg/mol, $T_g = 122$ °C) which was provided by micro resist technology GmbH (Germany) and supported by a silicon wafer depending on later application. Imprint was performed at 180 °C and 10 kPa for 10 min until at 60 °C was followed by demolding.

The polymer substrate supported by the 100 mm silicon wafer, PMMA 1S, was

prepared by imprint for 10 min of nickel template supplied by Applied Micro Swiss GmbH into 1.5 µm thick poly(methyl methacrylate) (PMMA) layer.

2.3.2 PMMA 1S Substrate

The characteristics of the "PMMA 1S" substrate, the patterned polymer film supported by a silicon wafer, are 700 nm wide and 1250 nm deep V-groove profile with an angle of 70° and 80° between the right and left side wall and 150 nm wide plateau connecting two V-grooves (Figure 2.2). Stamps for the grooves were replicas from mechanical ruled gratings provided by Richardson Labs Inc.
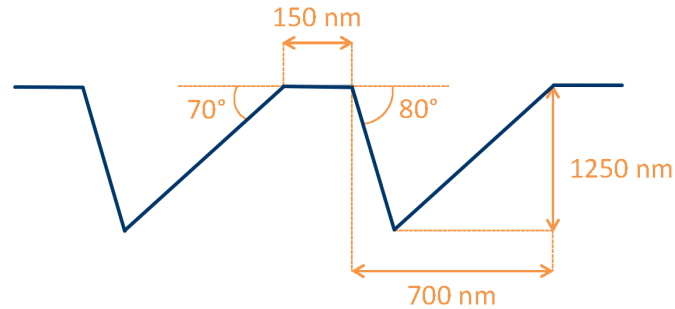
Figure 2.2: *Cross section of "PMMA 1S" substrate used for spin-coating.*

2.3.3 PMMA 2S Substrate

The characteristics of the "PMMA 2S" substrate are 3.2 µm wide and 2.3 µm deep V-groove profile with an angle of 54°44´ between the side wall and 800 nm wide plateau connecting two V-grooves (Figure 2.3). The ink solution was deposited on non-supported polymer foil with aerosol jet printing. In the case of spin-coating, the patterned polymer film was supported by a silicon wafer.
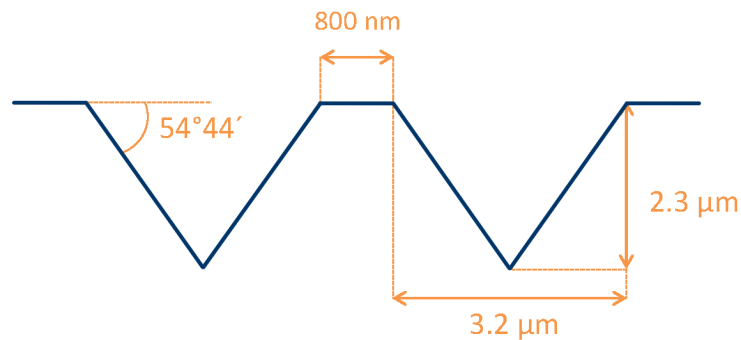
Figure 2.3: *Cross section of "PMMA 2S" substrate used for spin-coating and aerosol jet printing.*

2.4 Characterisation Techniques

- Scanning electron microscope (SEM) – Zeiss Supra 55 VP (Carl Zeiss NTS, Germany), InLens detector

- Optical contact angle measuring and contour analysis system - OCA 25 (Data-Physics Instruments, Germany)

- Ultrasound bath Emmi 20 (Emag Technologies, Germany)

- Vortex Genie 2 (Merck, Germany)

- Aerosol jet printer- Aerosol Jet 5X System (Optomec, USA), program for mask designing Tanner L-Edit IC Layout, provided by Mentor Graphics (Siemens, USA)

- Thermal evaporator - Balzers BAE-250 (Balzers union, Lichtenstein)

- Confocal microscope – Leica DCM8 (Leica microsystems, Wetzlar)

- Optical microscope – Leica INM 20 (Jenoptik, Wetzlar)

2.5 Substrate Cleaving

The cleaving of samples in liquid nitrogen is carried out to avoid the bending of the material during cleaving and thus allows cross area observation by scanning electron microscopy and later calculation. Samples were therefore immersed into liquid nitrogen for 2 min to become more brittle. This cleaving was used for polymer foils and polymer substrates supported by silicon wafer.

2.6 Spin-coating Process

The silicon substrate with patterned polymer layer was fixed on the holder by vacuum located in the middle of a tank. During the first 5 seconds a slower rotation velocity of 1000 rpm was applied before the main spin-coating time, and an approximately 20 µL droplet of silver ink solution was dropped on the centre of the pre-patterned substrate by a plastic pipette. Thin layers of the dispensed solution were spin-coated with an angular velocity of 3000 to 8000 rpm for 60 to 420 seconds with an acceleration of 1000 rpm·s^{-1}.

Only a small amount of ink was used for filling V-groove shaped substrate, redundant ink was centrifugated to the plastic tank below the holder. After separation of ink into lines by the top side of patterned edges, the silver nanoparticles settled down into the bottom of the V-groove. Before the sintering step, samples were left at least for one hour on the room temperature for a complete solvent evaporation.

2.7 Aerosol Jet Printing Process

The bubbler providing nitrogen gas was immersed in approximately 2 mL of silver ink solution supplied in a glass jar. The whole complex was placed into an ultrasound atomizer. Nozzles with orifice diameters of 100 and 300 µm were used with their z axis position of −154.2 (for spraying with AgD:IPA, 1:109) and −152.5 (for spraying

with AgD:IPA, 1:129 and 1:159). These z values correspond to the distance of about 3.8 mm between sample and the end of the nozzle. Sample was fixed by polyimide tape on 1 mm thick laboratory glass.

Lines were sprayed continuously by uniform nozzle movement above the sample in the x and y direction following the programmed mask (Figure 2.4) which was designed in the program Tanner L-Edit. During the deposition, individual samples were separated by closing and opening the shutter under the nozzle. The process velocity was varied in the range between 0.5 and 12 mm·s^{-1}, the carrier gas flow rate between 10 and 26 cm^3 · min^{-1} and sheath gas flow rate between 30 and 70 cm^3 · min^{-1} to observe their influence on sprayed areas. The process was carried out in a safety plastic box under room temperature with the exhaustion of released gas and solvent.
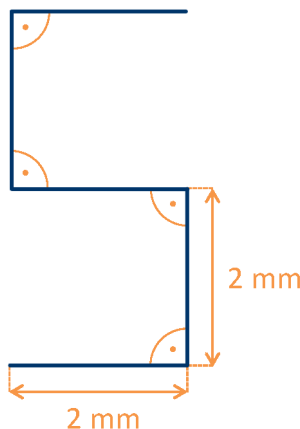

Figure 2.4: *Programmed mask followed by nozzle movement during aerosol jet printing process.*

2.8 Analysis of Areas Sprayed by Aerosol Jet Printing

2.8.1 Analysis of Line Widths of Sprayed Areas

Images captured by scanning electron microscopy containing the whole sprayed area were processed to highlight assembled lines. The width of separated lines was analysed from 15 measurements of 80 μm section of each line in ImageJ program and plotted in graphs. Each third non-interrupted line for line width depending on process velocity was measured. Each fourth non-interrupted line was analysed in the case of sheath gas flow and carrier gas flow influence. Lines presenting a specific behaviour change were additionally added into analysis to record the development.

2.8.2 Analysis of Sprayed Area Width

Many articles focusing on standardization of techniques for characterisation of sprayed area using expensive equipment can be found. [27] Due to high complexity of the thesis, sprayed area widths were computed from images captured by confocal

and optical microscopy by crossing the area with line of measured length in ImageJ program.

The total sprayed area width (d_t) represented by the largest sprayed area width was measured considering the farthest sprayed chunks. Due to nonspecific characterisation of borders caused by overspraying, only rough estimate was achieved by measuring area width containing the farthest sprayed chunks from more condensed chunk areas.

2.9   Thermal Sintering Process

Thermal sintering process was achieved by placing the treated substrate on the hot plate. If no exact procedure was tested, the sintering program was consisting of 3 min heating the plate up to 95 °C where the temperature was kept for 2 min to evaporate the solvent. Then 5 min of heating up and keeping the temperature at 150 °C for 30 min to sinter particle lines into wires followed. The cooling was done by unplugging the hot plate and the leaving sample on until reaching room temperature. To minimalize wire movement and thus interruptions, the slow cooling process lasting around 2 hours was chosen.

In the case of testing different sintering temperatures with the same sintering time, the samples were left on and cooled together with the hot plate at room temperature.

2.10   Analysis of Wire Widths and Line Edge Roughness

Two types of wire width were measured for different purposes by box plot method which also resulted in statistical interpretation of line edge roughness (LER). Due to granular edges, measured values considering the whole cross-section area including the furthest points compared to the middle of the line presents a normal wire width. The results of the largest possible width were presented as a general wire width in the Chapter 3.3.1.

The effective width, used for calculation of wire resistivity, was measured on a line crossing perpendicularly to the middle axis but including the closest points without considering neighbouring grains. Outstanding grains do not contribute during the electrical conductivity and would increase the error of resistivity measurement. These values, called effective widths, were used for calculation of wire resistivity.

Both line widths were measured at every 50 nm on the wire length of 4 µm. Measuring of different widths is demonstrated in Figure 2.5.
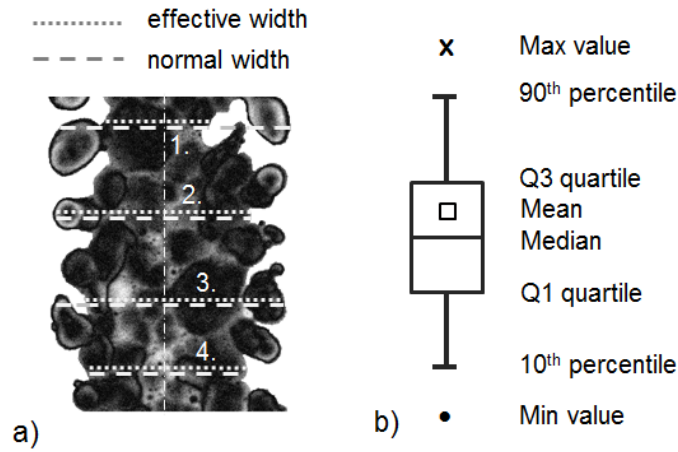
Figure 2.5: *Demonstration of a) measurement of normal and effective wire width and b) LER by box plot method.* [1]

The box plot method (Figure 2.5) was applied on collected data of wire widths containing values of 80 measurements. Median by middle horizontal line and mean with the square are displayed. Box plot also presents 90th percentile (- on the top side of the box), 75th percentile (Q3 quartile), 25th percentile (Q1 quartile), 10th percentile (- bottom side of the box), maximum values ($\times$) and minimum values ($\bullet$) of the data set. The statistical values of LER are then presented by difference between Q1 and Q3 quartiles.

2.11 Measurement of Single Wire Resistivity

To measure the resistivity of an average wire on an approximately 1×1 cm^2 spin-coated sample, two silver pads are sputtered using a thermal evaporator. The cleaned sample (by acetone and later by ethanol) is partly covered by a polyimide tape on all four sides to prevent thermal flow from mask due to high thermal conductivity which could lead to line disruption or sinking of formed structures into the substrate. After, the silicon mask with two $700 \times 700\,\mu\text{m}^2$ windows is placed on the surface and fixed with another tape so only the sample areas framed by the mask windows can be sputtered with a 100 nm thick silver layer. The final sputtered structures had 2 to 4 windows with 200 to 400 nm distance in between. Resistivity measurement was done by placing two probes connected with a microampere source on the sputtered pads with defined distance. Low current of 10 µA was applied and resistivity was measured. Higher current could lead to additional sintering and sinking of fabricated wires due to electrical heating.

After the measurement, the exact amount of non-interrupted wires was calculated from sample analysis made by SEM. Any interrupted or defected wire was excluded from the measurement and the exact number of intact wires was counted. The wire resistivity was calculated from Equation 2.1

$$\rho = \frac{R \cdot n \cdot \tan\alpha \cdot w_{\text{eff}}^2}{4L}, \tag{2.1}$$

where R is a resistance of the wire grid between two pads, n is a number of wires, w_{eff} is an effective width, α is an angle of the wire cross-section triangle at the surface and L is a wire length between two pads. The average cross-section area was calculated from the measured effective wire widths on the surface side of the triangle. The angle from the surface, 36°, was analysed from 25 cross-sections and added to the equation considering isosceles triangles.

3 Results and Discussion

3.1 Spin-coating

Spin-coating is a low-cost technique where the solution is dispensed and spread on the entire flat surface by centrifugal forces forming a thin layer of the remained dispensed solution due to adhesion and viscodynamic forces. The main idea presented here is based on spin-coating application as a low-cost technique for high resolution wire fabrication. The description of the idea is included in Chapter 1.4. Diluted ink containing silver nanoparticles was chosen as spin-coated solution on the pre-patterned substrate containing lines which have a cross-section of V-grooves.

As the first step for spin-coating process design, a solvent which would lead to fine particle sedimentation without any particle remaining on the dewetted surface during evaporation is needed to be found. Only alcohol with glycol for silver "dense" ink (AgD) and alkane for silver "light" ink (AgL) were listed in the supplier's product sheets as the solvent of the ink. Due to unknown original solvents of the commercial inks, some chosen alcohols and alkanes for ink dilution with different ratios were tested. The solvents were chosen with the emphasis on their chain length, chemical interaction with the substrate and contact angle during evaporation. Solutions with accurate dilution ratios of AgD ink with 2-buthanol, ethanol, isopropyl alcohol (IPA) and 1-pentanol for their shorter chain length were chosen while 2,2,4-trimethyl pentane (TMP), 2-heptane and decane with longer chain length were used for preparing solutions with AgL ink.

All samples were spin-coated on "PMMA 1S" substrate and thermally sintered for 30 min at 150 °C temperature with a preheating step at 95 °C for two minutes and were analysed by SEM. SEM images were investigated on their line edge roughness (LER), homogeneous width, interruptions or other defects in the form of additional agglomerates. Particle remaining after spin-coating on the plateaus was also considered even when the properties of V-grooves inhibit particle contact between assembled lines and particle remaining on the plateaus. It is shown in Figure 3.1 where PMMA substrate was reflowed by thermal sintering and flattened. The plateau area is then displayed as the lighter area between lines covered by particles depending on their settlement on the plateaus.

Due to used conditions for preparation of samples in Figure 3.1, the wires almost did not separate probably because of low ink dilution. Solution of AgD:ethanol did not support particle connectivity forming wide non-intact lines, probably due to increasing the repulsive forces between particles. [24] Moreover, many particles remained on the plateaus and therefore ethanol was avoided from further experiments.
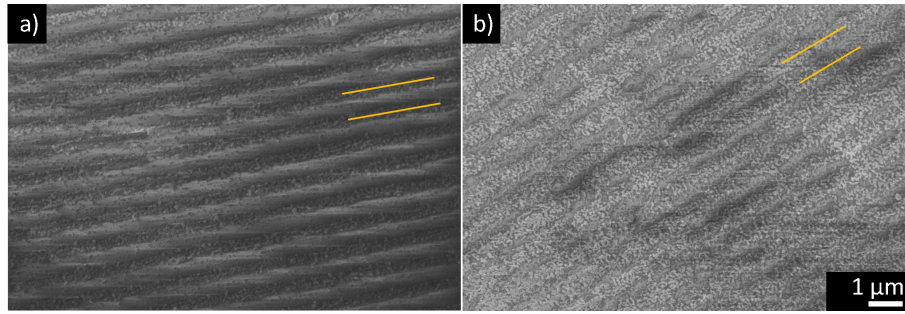
Figure 3.1: *SEM micrographs of solution a) AgD:IPA, b) AgD:ethanol with dilution ratio 1:49. Samples were spin-coated for 180 s with 5000 rpm velocity on a "PMMA 1S"substrate. The two yellow lines illustrate the direction of the spin-coated lines. (All items included in one Figure possess the same magnification. In the case of different magnifications, additional scale bar is provided.)*

Higher ink dilution was chosen and spin-coated to avoid particle residue between wires. The resulted samples are captured in Figure 3.2. AgD:1-pentanol solution was no longer tested for very strong grain growth during sintering (explained in Chapter 3.3.1). Probably due to the effect of short chain length, the lines prepared with spin-coated AgD:IPA and AgD:2-buthanol solutions showed homogeneous thickness with no additional agglomerates. Contact angle measurement of IPA showed very good wetting properties with a contact angle around 0°. Moreover, its application on PMMA surfaces did not show any polymer chemical dissolution or disruption. Therefore, the solution AgD:IPA was chosen for later experiments to improve conditions for decreasing the number of particles on the plateau and line edge roughness (LER).
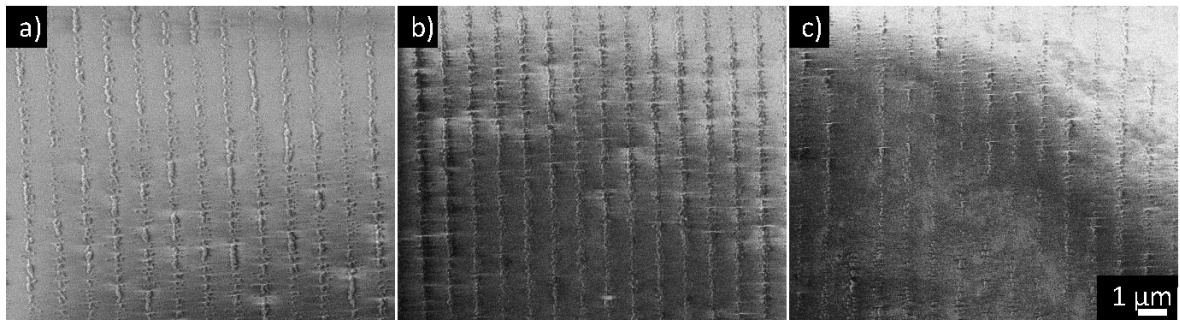

Figure 3.2: *SEM micrographs of a) AgD:IPA, b) AgD:2-buthanol, c) AgD:1-pentanol with dilution ratio 1:69. Samples were spincoated for 120 s with 5000 rpm velocity on a "PMMA 1S" substrate.*

In comparison of all three solvents mentioned for AgL ink, the solution of AgL:TMP showed the biggest potential to connect particles into lines with low grain sizes after sintering. Solution with 2-heptane did not spread on the whole substrate and the particles agglomerated into big clusters during drying. The substrate after spin-coating of AgD:decane solution seemed to be partly dissolved with nanoparticle sinking into the polymer (Figure 3.3).
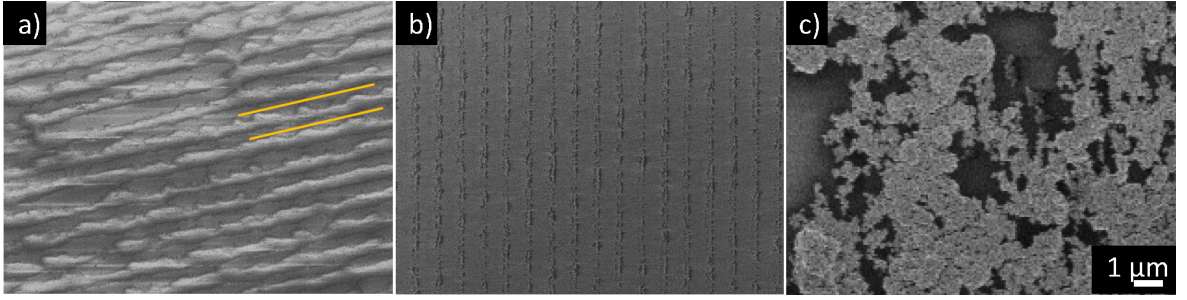
Figure 3.3: *SEM micrographs of spin-coated a) AgL:TMP, b) AgL:decane and c) AgL:2-heptane with dilution ratio 1:19. Samples were spin-coated for 420 s with 5000 rpm velocity on a "PMMA 1S" substrate. The two yellow lines illustrate the direction of the spin-coated lines.*

At the same time as looking for suitable ink solvents, spinning conditions needed to be tuned for achieving straight intact lines with low LER, and low particle content on the plateau. The combination of AgL:TMP was chosen and a variation of speeds and spin-coating times were experimentally tested with this solution to optimize line characteristics (Figure 3.4).

Also, the moment of placing a solution drop on the substrate was investigated. No evident difference between the samples with a drop applied before and during the first seconds of spin-coating was observed. Therefore 5 seconds of slower rotation velocity of 1000 rpm was used before the main spin-coating time, and a drop of solution was applied during this lower speed. With this method, the coffee stain effect with higher border edge was inhibited and the spin-coating time was maintained.

Dilution ratio	t [s]	ω [rpm]	a [rpm·s^{-1}]	Observed line properties
1:19	200	7000	1000	Spin-coated conditions were skipped due to vacuum error caused by long spin-coated time.
1:19	180	8000	1000	Lines with almost homogeneous width and few interruptions due to high rotation speed
1:19	120	5000	1000	Lines with almost homogeneous width and minimum interruptions
1:19	120	3000	1000	Very wide lines due to large amount of settled material caused by low rotation speed
1:29	180	8000	1000	Lines with almost homogeneous width and few interruptions due to high ink dilution
1:39	120	8000	1000	Lines with almost homogeneous width and few interruptions due to high ink dilution
1:49	180	8000	1000	
1:49	180	5000	1000	Too high dilution inhibited line formation
1:49	120	5000	1000	
1:49	60	5000	1000	

Figure 3.4: *Spin-coating conditions applied on solution AgL:TMP for tuning of line properties where t is spin-coating time, ω is velocity and a is acceleration.*

Due to long spin-coating times (≥ 200 s), the plastic seal on the spin-coating machine was elongated and vacuum release error occurred. Spin-coating time duration was therefore consequently lowered with the dilution ratio and rotating velocity adaptation.

A new "PMMA 2S" substrate with smaller width of plateaus and V-grooves was designed to achieve better wire resolution and smoother sidewalls for particle sedimentation enhancement and residue plateau inhibition. The substrate was used for all following experiments containing spin-coating process.
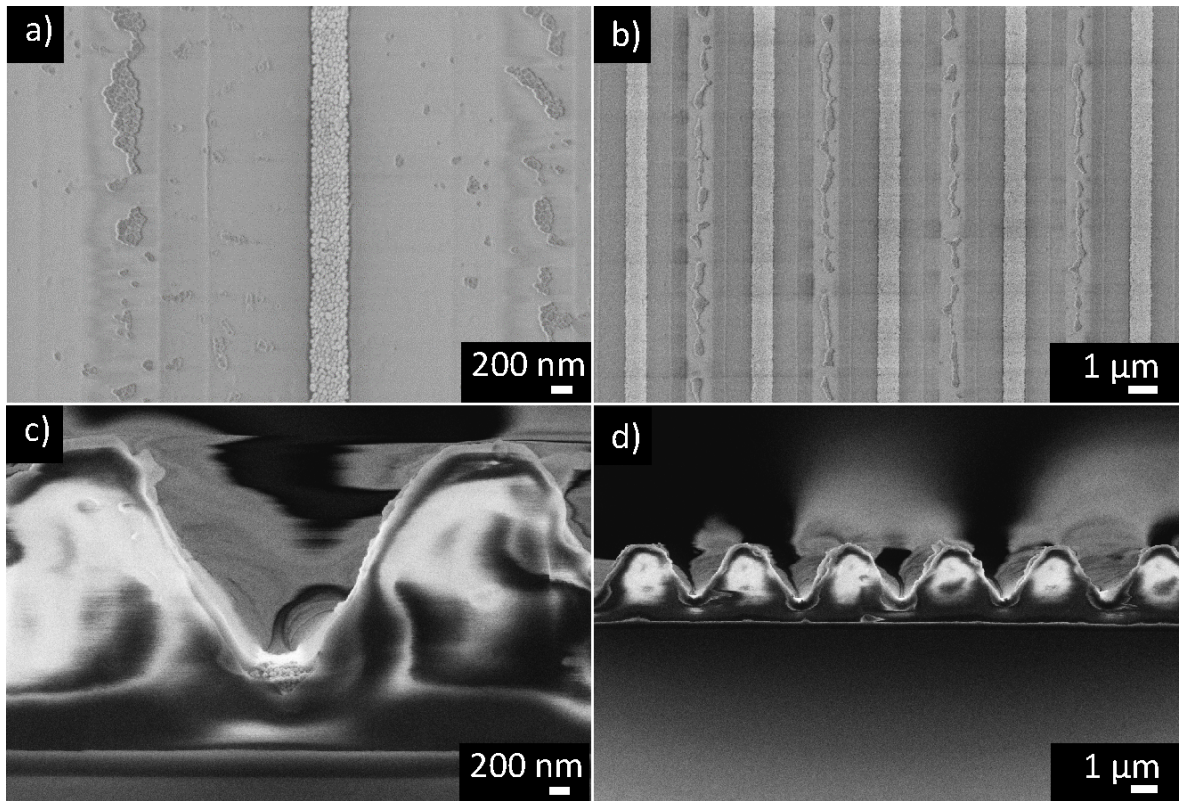
Figure 3.5: *SEM micrographs displaying a) a detail of spin-coated line from top view and c) its cross-section on polymer substrate, b) a general overview of spin-coated lines from the top view and d) their cross-sections on polymer substrate. The sample was prepared by AgD:IPA solution with dilution ratio 1:59 spin-coated for 120 s with the 5000 rpm velocity on the "PMMA 2S" substrate.*

After optimising the spin-coating conditions and all the process steps, very fine ~ 370 nm homogeneous lines with similar widths and very reduced roughness were obtained and analysed by SEM before an additional sintering post process. The lines with nicely visible surface topology (V-grooves and plateaus) and their cross-sections made by precise cleaving are illustrated in Figure 3.5.

Even though very homogeneous, non-interrupted lines without defects and with low particle content between separated V-grooves were obtained, AgL:TMP solution was skipped due to its high LER which would not be acceptable for required wire conductivity in the case of microelectronic applications.

Different strategies for shrinking the wire width were experimentally tested. One way is based on increasing the ink dilution and thus decreasing of particle content and was applied on the sample which is shown in Figure 3.6. A reduced number of particles is settled on the bottom of each V-groove. This method allows the fabrication of fine structures with line width even near the 100 nm range with a few settled particles next to each other.
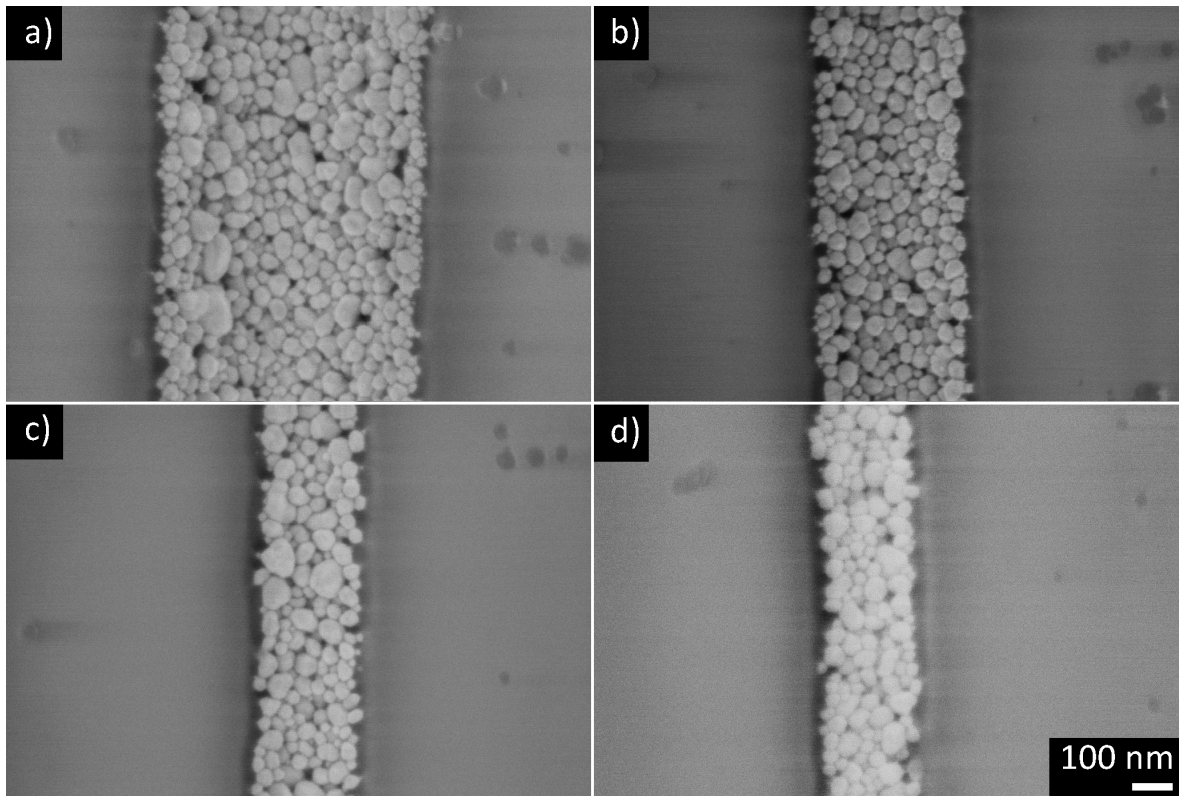
Figure 3.6: *SEM micrographs of non-sintered line width changes of spin-coated Ag:IPA with a dilution ratio of a) 1:59, b) 1:109, c) 1:199, d) 1:259.*

To reduce line widths, AgD:IPA solutions with ratios 1:59, 1:109, 1:199 and 1:259 were spin-coated for the same time with the same spin-coating conditions (120 s, 5000 rpm). The obtained widths were in the range from 200 to 750 nm depending on the dilution ratio, specifically (731 ± 19), (358 ± 23), (249 ± 22) and (217 ± 18) nm for 1:59, 1:109, 1:199 and 1:259 dilution ratio. This experiment clearly confirmed the possibility to use the low resolution spin-coating method for obtaining high resolution lines and then sintering into conductive wires.

Even under stable laboratory conditions, the sample results were strongly dependent on surrounding aspects. To demonstrate the climate influence, samples prepared with the same conditions i.e. the solution with dilution ratio AgD:IPA 1:59 were spin-coated for 120 s with the 5000 rpm velocity (Figure 3.7). Both samples were prepared within 1 month. The first one (a) was prepared during cold and rainy weather and the second one (b) with the sunny and dry weather conditions. Further experiments proved the theory about line width dependence based on different dilution ratio. However, environmental conditions need to be considered when choosing the dilution ratios to obtain a required line width.
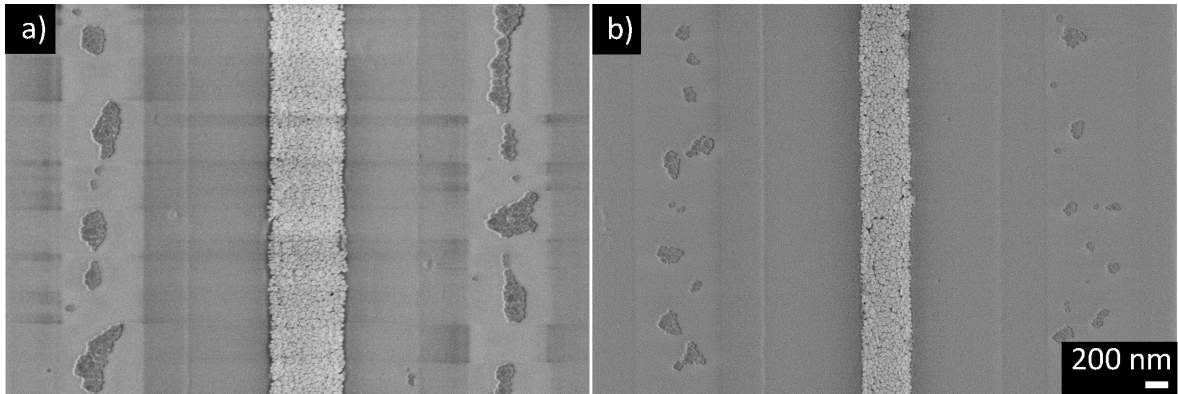
Figure 3.7: *SEM micrographs of two samples spin-coated with the same solution AgD:IPA with dilution ratio 1:59, spin-coated for 120 s with the 5000 rpm velocity on a) April 4 and b) May 22.*

3.2 Aerosol Jet Printing

Aerosol jet printing (AJP) is an additive printing technique working on the principle of continuous deposition of ink droplets with a focused jet. Like inkjet, it is intended for use in mass production of electronics, however, with the advantage that the deposition of the small, accelerated ink droplets in a carrier gas enable an almost dry deposition with negligible spreading upon impact on the substrate, thus enabling down to 10 µm resolution of sprayed wires. Lines are formed from a spray of mist rather than from single large droplets, and in both cases spread after impact onto the substrate and merge into a continuous line. To increase the resolution even further, with the aim of sub-µm resolutions by confinement, the same idea considering pre-pattern substrate combined with wet deposition was used. Due to the "dry characteristic" of the jet, droplets sizes smaller than the intended line width do not allow the confinement strategy of spin-coating. This relies on the fact that particles carried in solution are sprayed into a V-groove, and upon evaporation of the solvent concentrate at its vertex, thus enabling a narrowing of the line width. A too dry deposition would inhibit this narrowing due to premature evaporation (Figure 3.8), a too wet deposition would cause capillary flow along grooves. The aim of this chapter is to find the best configuration of conditions depending on the specific applications, and to use the potential of this technique for high-resolution printing.
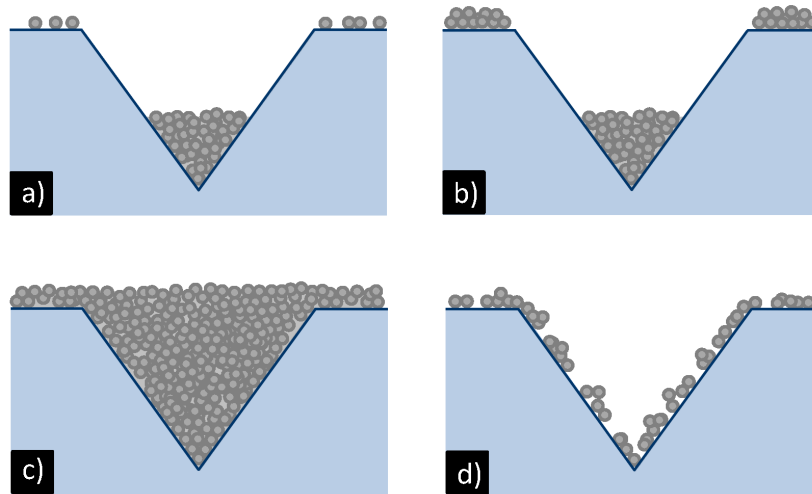
Figure 3.8: *Schematics of different types of filling by sprayed ink on the substrate with V-groove cross section, a) confinement filling and a few isolated particles on plateaus, b) confinement filing and particles connected into intact lines on plateaus, c) overfilling and d) dry deposition.*

Four main situations occurring due to spraying on pre-pattern surfaces are described in Figure 3.8, mainly different in terms of the amount of deposited ink and its dynamics of evaporation. Due to the wet deposition achieved by applying suitable gas flows (carrier and sheath gas flows) with referring process velocity (velocity of nozzle movement), the ink is homogeneously transferred and confined in separated V-grooves forming line structures at the bottom of the vertex. Due to particle movement by sliding down during the solvent evaporation, the upper part of the sidewalls is free from particles and therefore formed line is not connected with plateaus. Depending on particle density sprayed on plateaus, this case can be divided into two situations which can later influence the product application. The first situation is described as an ink confinement within the V-grooves while only few isolated particles are sprayed on plateaus. It can be considered as an ideal for electronics applications where only conductive wires at the bottom of the V-groove are required. For example, wire structure with defined placing of separated wires i.e. optical polarizers. The second situation is described as the ink confinement within V-grooves with additional intact lines formed due to high amount of deposited ink on the plateaus. It is desired for large area sensors where lines on plateaus increase the resolution of sensing and thus the sensing performance can be multiplied.

When the amount of deposited particles is higher than the capacity of V-grooves, overfilling occurs. Deposited ink is flowing over all V-grooves and homogeneously sediments until all solvent is evaporated. All filled V-grooves are covered by layer of additional ink and therefore the whole complex of structures is connected.

The last situation, dry deposition, is caused by very quick evaporation of solvent. Thus, particles can not slide down, accumulate and spread within capillaries due to lack of solvent. The deposited ink therefore stays on the place and do not move after first deposition.

Depending on the constellation of spraying direction and the direction of V-grooves

(Figure 3.9), the spreading driven by capillary forces can be increased by continuously spraying ink at one spot onto capillaries and thus supplying material like from a reservoir. One of the examples can be described by perpendicular spraying trajectory to the V-grooves where the spreading is caused only by capillary filling. The ink is spreading from the middle of sprayed area to the sides forming lines thinner in the middle and wider at the side. The stop point of the spreading is determined by the drying process. [2] Nevertheless, the spraying in perpendicular direction will not be considered in this thesis for high complexity of the topic.
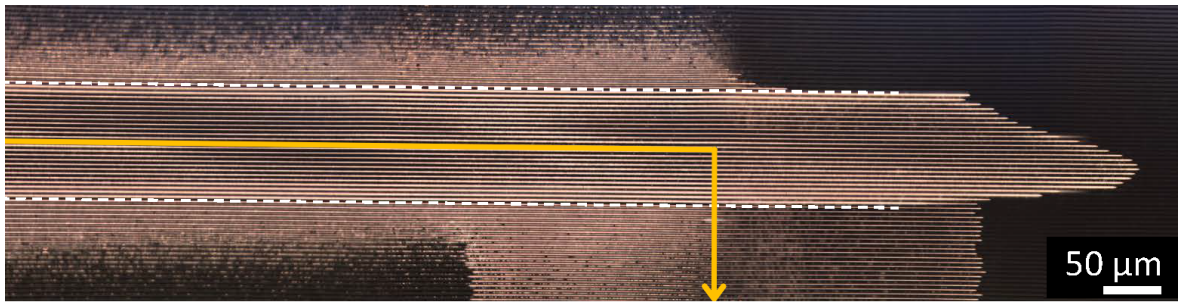

Figure 3.9: *Confocal microscope image of additional spreading of silver ink in V-grooves after parallel (middle part) and perpendicular (down part) spraying while the nozzle follows the process trajectory (presented by yellow line). The plateau sprayed area (indicated by white dashed lines) is surrounded by oversprayed mist. Upon change of direction of the deposition, the spreading along capillaries becomes visible, in the extension of the line along grooves resulting in an extended line (to the right) and a broadening of the line. Demonstrated solution AgD:IPA with dilution ratio 1:109 was sprayed with process velocity of 4 mm·s^{-1}, carrier gas flow rate of 20 cm^3 · min^{-1} and sheath gas flow rate of 50 cm^3 · min^{-1}.*

Due to continuous movement of the nozzle parallel to the V-groove orientation, the spreading can be enhanced by generated forces of further deposited ink. The spreading continues supported by additional ink in its direction until reaching the drying point and thus longer lines than the sprayed area are obtained (Figure 3.9). Furthermore, the surface of assembled lines is additionally refined in the direction of V-grooves to lower down the surface free energy which supports the homogeneity of line widths. The density of ink deposition and also the ability to preserve the wetness of ink can be controlled by the parameters summarized in Figure 3.10.

Process parameter	Size	Variation → Effect
Nozzle diameter	100 µm, 300 µm	↑nozzle diameter ↑ confinement
Carrier gas	gas flow rate 16 – 24 cm³·min⁻¹	↑ carrier gas flow rate ↑velocity of impacting ink droplets
Sheath gas	gas flow rate of 40 – 60 cm³·min⁻¹	↑sheath gas flow rate ↑focus of main area possible premature drying
velocity of lateral nozzle movement	0.5 – 10 mm·s⁻¹	↑process velocity ↓amount of deposited material ↓confinement
Ink dilution ratio	1:109, 1:129	↑solvent ↑confinement
Substrate properties	-	↑surface roughness ↓confinement

Figure 3.10: *Process parameters influencing the density of ink deposition and the ability to preserve the wetness of ink.*

To increase the amount of ink able to flow and inhibit the evaporation of solvent, a nozzle with a large diameter was chosen. While wet deposition on PMMA 2S substrate (used for all aerosol jet printing experiments) and thus the ink spreading within capillaries was observed by using the nozzle diameter of 300 µm; it was only possible to carry out dry deposition with the nozzle diameter of 100 µm. Both cases were realized with set conditions; carrier gas flow rate of $20 \, \mathrm{cm}^3 \cdot \mathrm{min}^{-1}$ and sheath gas flow rate of $50 \, \mathrm{cm}^3 \cdot \mathrm{min}^{-1}$. Variation of process velocities started from the slowest available motion of $0.5 \, \mathrm{mm \cdot s}^{-1}$ which should support releasing higher content and thus prolonging the necessary time for ink to spread before drying.

Small spherical aggregates occurred covering the surrounding and the top of already sprayed area. These small chunks consist of atomized ink which interacted with the sheath gas in the nozzle. [31] These particles were excluded from the main stream, and after passing the nozzle they were released under a higher angle than the rest of aerosol. Therefore, they often copy the spraying trajectory which leads to overspray. However, chunks can spread and confine within V-grooves forming oversprayed lines during the wet deposition. Therefore, these chunks are also included into analysis of sprayed area widths. Specifically, the *total sprayed area* width (d_t) is represented by the largest sprayed area width considering also the chunks. Due to nonspecific characterisation of borders caused by overspraying, only rough estimate was achieved by measuring the width containing only the farthest sprayed chunks from optically more dense area.

Since the nature of V-grooves supports the separation of confined ink in the vertex and the residue remaining on plateaus, only separated lines are assembled until the amount of released material passes the limit and overfilling occurs (Figures 3.8, 3.11). Therefore, the overspraying should not significantly influence the electrical conductivity of the fabricated wires since formed lines will not be in touch. Thus, the *main area* (d_m), area consisted of all formed intact and isolated lines is considered as one of the most important parameters determining possible product application.

Isolated lines are mainly the case because nanoparticles from the sidewalls are washed down to the vertex and the upper part of the slopes are therefore free from particles. Furthermore, when the density of particles is low, they are sparse enough that they will not touch on the plateaus, too. Thus, the *plateau area* (d_p), area containing

plateaus sporadically covered by low amount of particles and therefore not forming lines on the plateaus, is easily detached.

The last measured area, the *area containing homogeneous line width* (d_{h}), is established as a part of the main area where the line width varies maximally in the range of 300 nm. All areas are demonstrated in Figure 3.11.
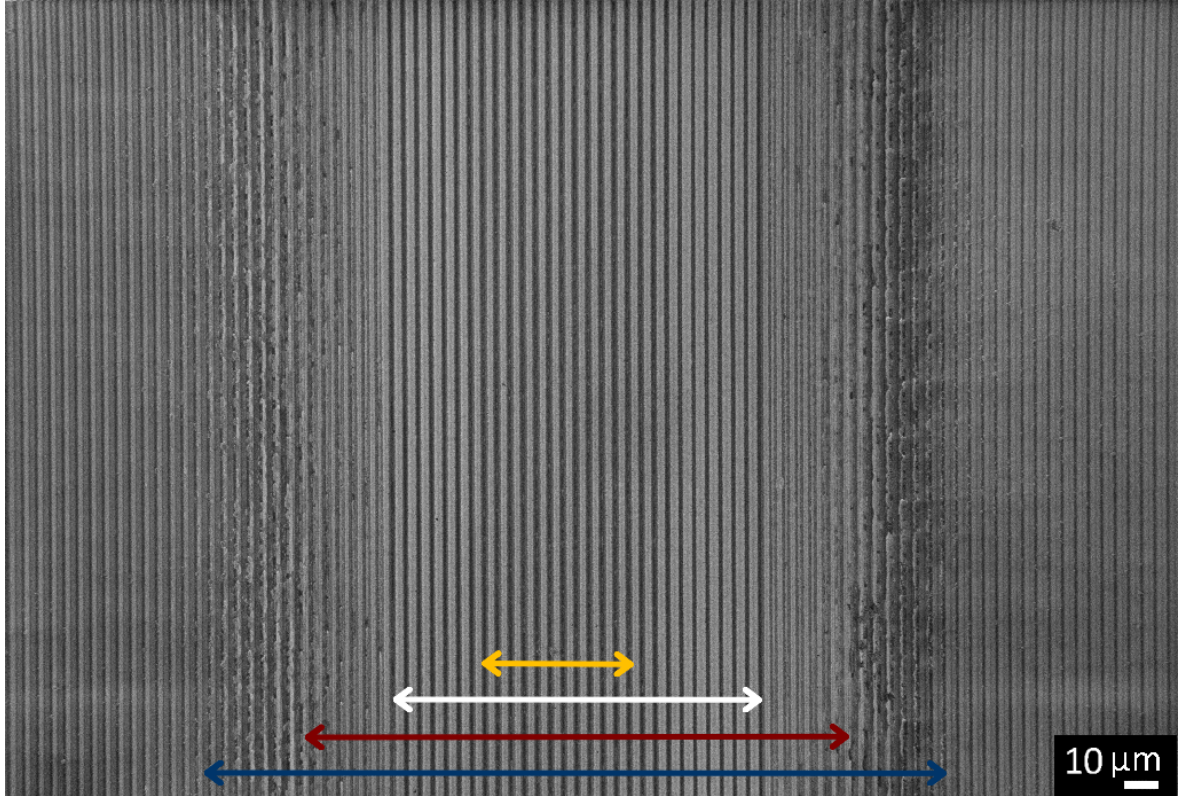

Figure 3.11: *SEM micrograph of deposited area by solution AgD:IPA with dilution ratio 1:109 which was sprayed with process velocity of 2 mm·s^{-1}, carrier gas flow rate of 20 cm^3 · min^{-1} and sheath gas flow rate of 50 cm^3 · min^{-1}. The deposited total area (d_t) is indicated by blue arrow, the main area (d_m) by red arrow, the plateau area (d_p) by white arrow and the homogeneous area (d_h) by yellow arrow.*

3.2.1 Changing velocity of nozzle movement

Wet deposition can be enhanced by decreasing the velocity of the lateral nozzle movement. Slower process velocity of spraying allows a higher amount of aerosol deposition on the selected sprayed area which should support prolongation of time necessary for ink spreading before the ink starts to dry. When the capillary is completely filled, the ink distributes furthermore into neighbouring V-grooves (Figure 3.12). Inhomogeneity of line widths and overfilling occurs while the ink is covering already dried ink. Due to the dried ink, the surface roughness increases and therefore, the further ink spreading is inhibited.

The inequality of line widths i.e. the deviation from symmetric deposition, located on the opposite sides with the same distance from the middle axis of the sprayed area, was induced by asymmetry of nozzle orifice or other nozzle defects. It occurred in all experiments and it was mainly visible during a comparison of two sides of area sprayed

parallelly to the V-groove direction. This effect can be easily eliminated by replacing the nozzle and thus should not influence usability of the technique. In all cases, the lines are non-sintered, i.e. measured after drying, before an electrical conducting wire formation. Good lines are qualified by two parameters: their continuity without any interruption over the deposition length along the grooves (intact lines) and their separation from neighbouring grooves. Once sintered, this would result in conducting wires without any shortcuts.
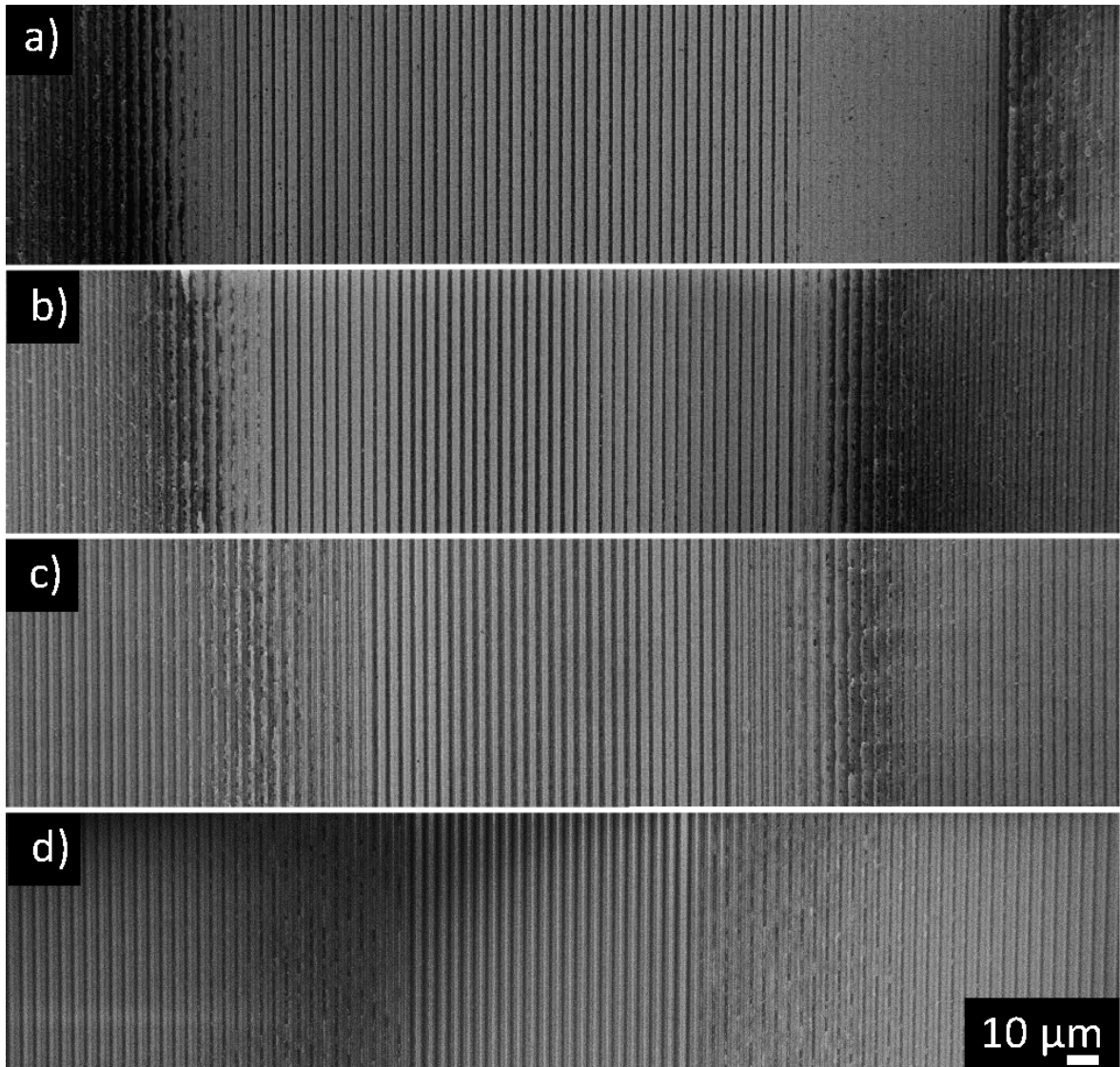

Figure 3.12: *SEM micrographs of deposited areas by solution AgD:IPA with dilution ratio 1:109 which was sprayed with process velocity of a) 0.5, b) 1, c) 2 and d) 10 mm·s^{-1}, carrier gas flow rate of 20 cm^3 · min^{-1} and sheath gas flow rate of 50 cm^3 · min^{-1}.*

v [mm·s^{-1}]	d_t [µm]	d_m [µm]	d_h [µm]	d_p [µm]
1	199	173	55	167
2	198	152	44	121
10	206	132	60	90

Figure 3.13: *Width of the total sprayed area (d_t), the main area (d_m), the homogeneous area (d_h) and the plateau area (d_p) depending on the process velocity (v). Demonstrated solution AgD:IPA with dilution ratio 1:109 was sprayed with carrier gas flow rate of $20\,cm^3 \cdot min^{-1}$ and sheath gas flow rate of $50\,cm^3 \cdot min^{-1}$.*
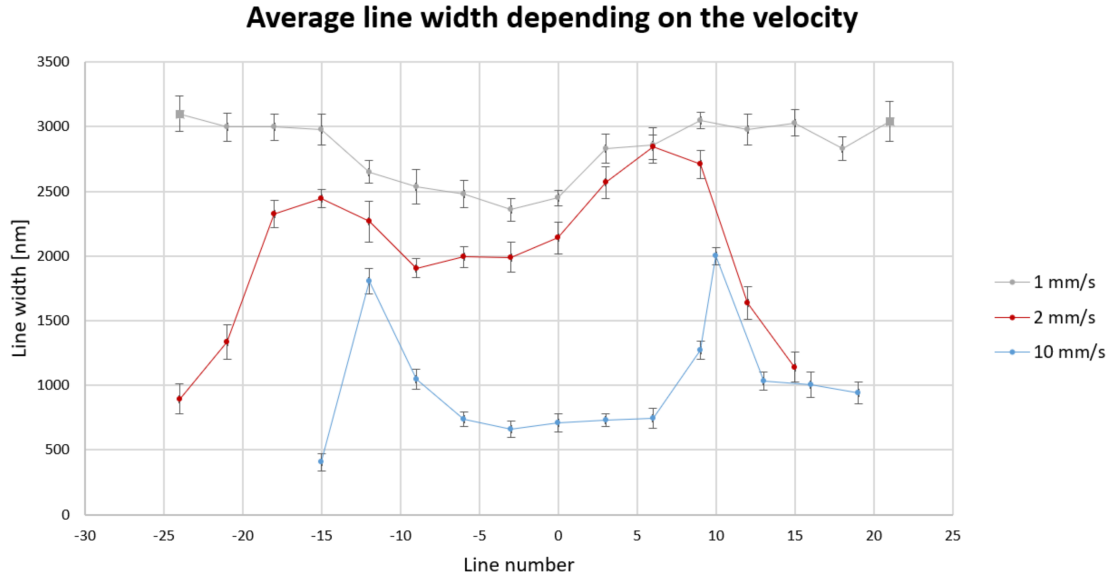

Figure 3.14: *Average line width depending on the process velocity determined from SEM micrographs measured from the cross section of sprayed area. Demonstrated solution AgD:IPA with dilution ratio 1:109 was sprayed with process velocity of 1, 2 and $10\,mm·s^{-1}$, carrier gas flow rate of $20\,cm^3 \cdot min^{-1}$ and sheath gas flow rate of $50\,cm^3 \cdot min^{-1}$. The isolated lines are represented by round signs, the squares demonstrate overfilled area with shortcuts between lines and plateaus.*

Lower nozzle speed leads to overfilling (Figure 3.12), higher speed leads to lower deposition of single, unconnected droplets and thus rapid drying. In the case of higher process velocity, almost all material surrounding the main area was deposited already in an almost dried state. Therefore, chunks were not connected into additional surrounding and thus overspraying became more significant. So, the total $\sim 200\,\mu m$ sprayed area (d_t) width did not significantly change (Figure 3.13) but deviations in the number of proper lines (d_m) fabricated with variation of velocities occurred due to different amount of released material. With process velocity increasing, the amount and thus wetness of deposited ink decreased which caused lower number of proper lines and inhibited the particle movement from plateaus into the V-grooves presenting by lower d_p. On the other hand, less deposited material led to not completely fulfilled V-groove channels and therefore thinner line formation with more homogeneous widths (Fig-

ure 3.13). Hence high-resolution wires with homogeneous widths can be tuned and fabricated depending on preferences for later applications.

3.2.2   Changing sheath gas flow rate

The effect of process velocity variation and thus a line appearance is influenced by many factors and cannot be studied separately, mainly gases applied during process; gas carrier aerosol mist and sheath gas influence the sprayed structure the most. Deposited ink can be furthermore displaced after confinement in V-grooves by its gas driven force or by another incoming aerosol. Probably due to possible turbulent flow in separate trenches, doses of solution can be replaced reaching neighbouring V-grooves until they become dried or the source of intense pressure is removed. It is presented on the areas sprayed with velocities of 0.5 and $10\,\mathrm{mm\cdot s^{-1}}$ (Figure 3.12) which possess high difference between surrounding line widths. It can be explained by different amount of deposited particles due to slower process velocity. Higher density of ink droplets limits the gas influence upon drying, enables the build-up of droplets to a closed film, and therefore the probability of premature drying of ink droplets.

Another parameter, more visible in the case of higher process velocity of $10\,\mathrm{mm\cdot s^{-1}}$, is a sheath gas flow responsible for beam focusing and therefore overspraying. The process velocity of $2\,\mathrm{mm\cdot s^{-1}}$ and carrier gas flow rate of $20\,\mathrm{cm^3\cdot min^{-1}}$ were preserved during the spraying process to clarify the influence of the sheath gas on the V-groove structure separately. Higher dilution ratio, 1:129 AgD:IPA, was chosen to support the wet deposition and thus reduce the overspraying (Figure 3.16). The connection between chunks was improved by less viscous aerosol, so overspraying became less visible. Due to higher dilution and thus less released material, the overfilling of V-groove was also avoided in the case of slower process velocities, mainly $0{,}5\,\mathrm{mm\cdot s^{-1}}$. The influence of dilution ratio on the confined structure can be presented in Figures 3.12, 3.15, 3.16 by ink dilution ratios 1:109 and 1:129 sprayed with the process velocity of $2\,\mathrm{mm\cdot s^{-1}}$, carrier gas flow rate of $20\,\mathrm{cm^3\cdot min^{-1}}$ and sheath gas flow rate of $50\,\mathrm{cm^3\cdot min^{-1}}$. The shape of lines presenting different solutions can be explained by different ability of ink atomization due to high dilution ratios.
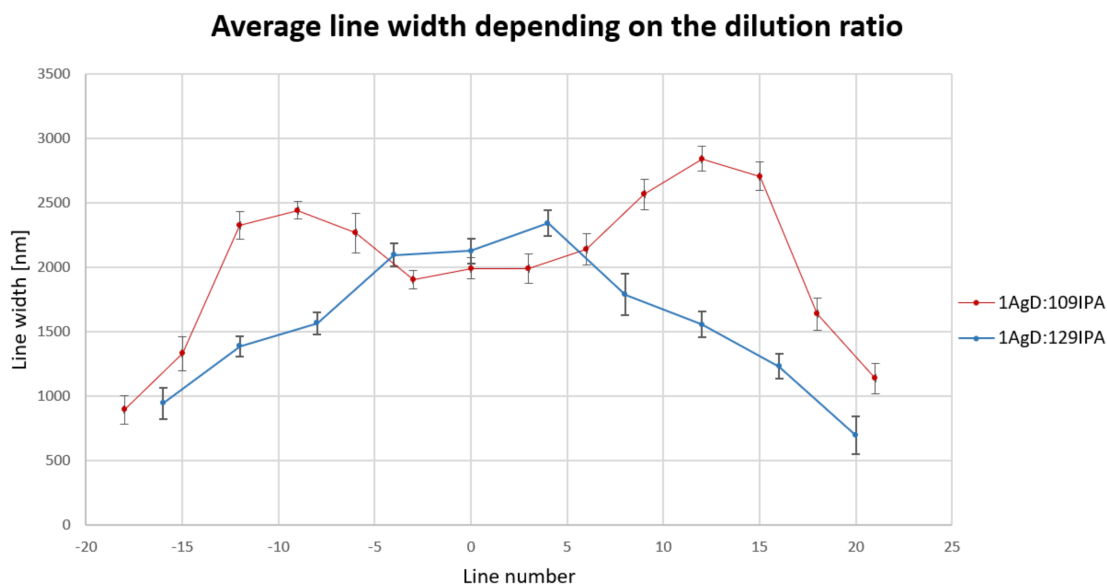
Figure 3.15: *Average line width depending on the dilution ratio determined from SEM micrographs measured from the cross section of sprayed area. Demonstrated solutions AgD:IPA with dilution ratios 1:109 and 1:129 were sprayed with process velocity of $2\,mm{\cdot}s^{-1}$, carrier gas flow rate of $20\,cm^3{\cdot}min^{-1}$ and sheath gas flow rate of $50\,cm^3{\cdot}min^{-1}$.*

Figure 3.16: *SEM micrographs of deposited areas by solution AgD:IPA with dilution ratio 1:129 which was sprayed with process velocity of $2\,mm{\cdot}s^{-1}$, carrier gas flow rate of $20\,cm^3 \cdot min^{-1}$ and sheath gas flow rate of a) 40, b) 50 and c) $60\,cm^3 \cdot min^{-1}$.*

40

By decreasing the overspraying effect, the defocusing of the beam by decreasing sheath gas becomes an advantage. While the plateau area (d_p) stayed almost identical, more lines with higher homogeneity (d_h) and lower width were obtained by beam defocusing over approximately $300\,\mu\text{m}$ total sprayed area (d_t) (Figures 3.17, 3.18). Theoretically, the largest possible area containing homogeneous width of lines reached by sheath gas flow minimalization and atomization of even higher dilution ratios of inks, is limited only by the aerosol jet printing device.

SG [$\text{cm}^3\cdot\text{min}^{-1}$]	d_t [µm]	d_m [µm]	d_h [µm]	d_p [µm]
40	297	173	60	38
50	237	146	44	40
60	212	138	32	40

Figure 3.17: *Width of the total sprayed area (d_t), the main area (d_m), the homogeneous area (d_h) and the plateau area (d_p) depending on the sheath gas flow rate (SG). Demonstrated solution AgD:IPA with dilution ratio 1:129 was sprayed with process velocity of $2\,mm\cdot s^{-1}$ and carrier gas flow rate of $20\,cm^3 \cdot min^{-1}$.*

Figure 3.18: *Average line width depending on the sheath gas flow calculated from the cross section of sprayed area. Demonstrated solution AgD:IPA with dilution ratio 1:129 was sprayed with process velocity of $2\,mm\cdot s^{-1}$, carrier gas flow rate of $20\,cm^3 \cdot min^{-1}$ and sheath gas flow rate of a) 40, b) 50 and c) $60\,cm^3 \cdot min^{-1}$.*

3.2.3 Changing carrier gas flow rate

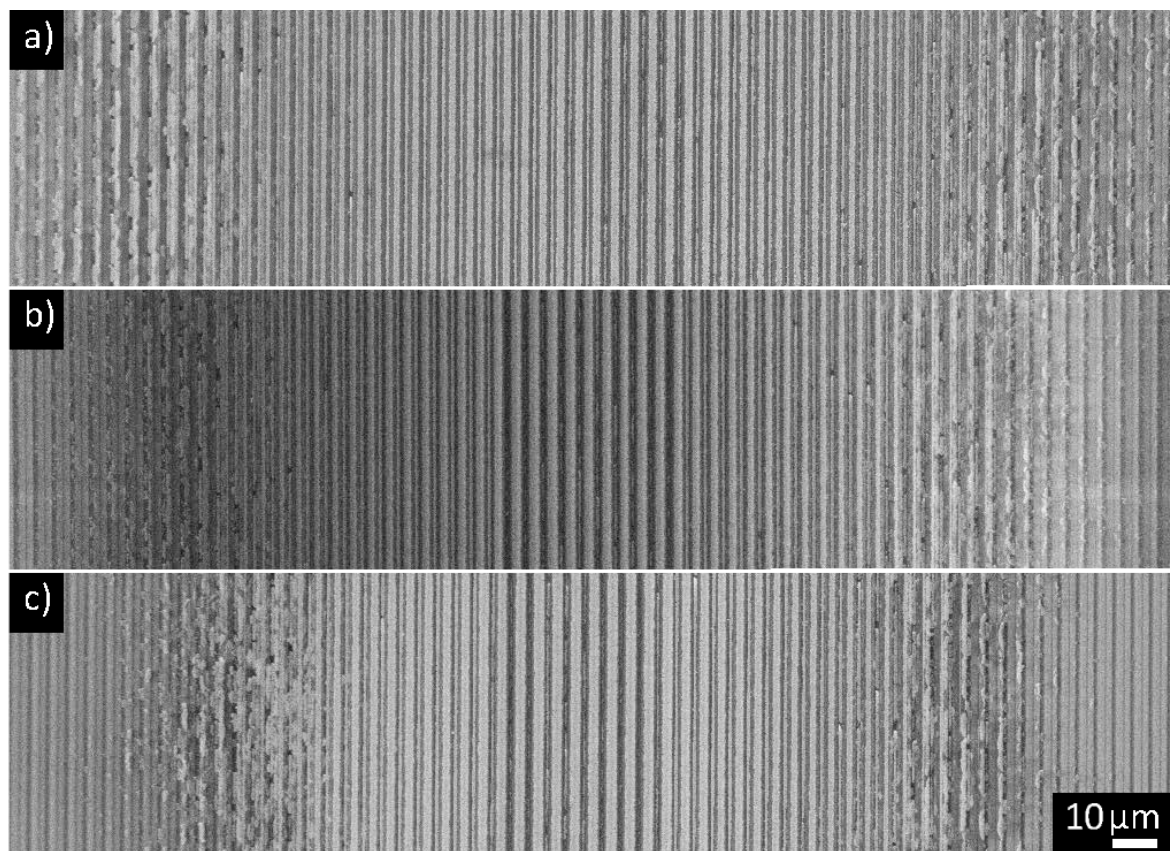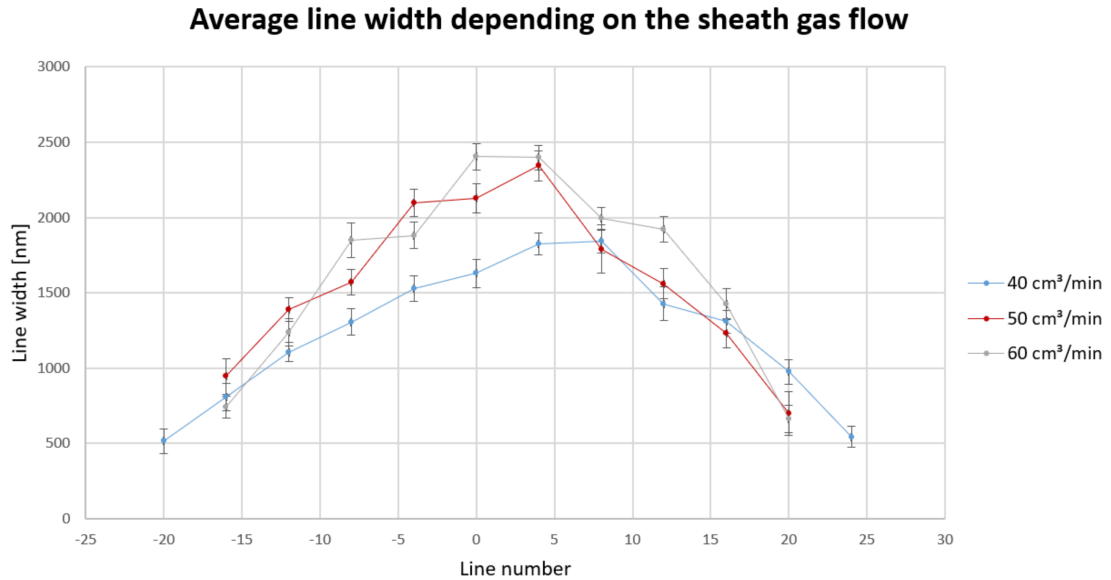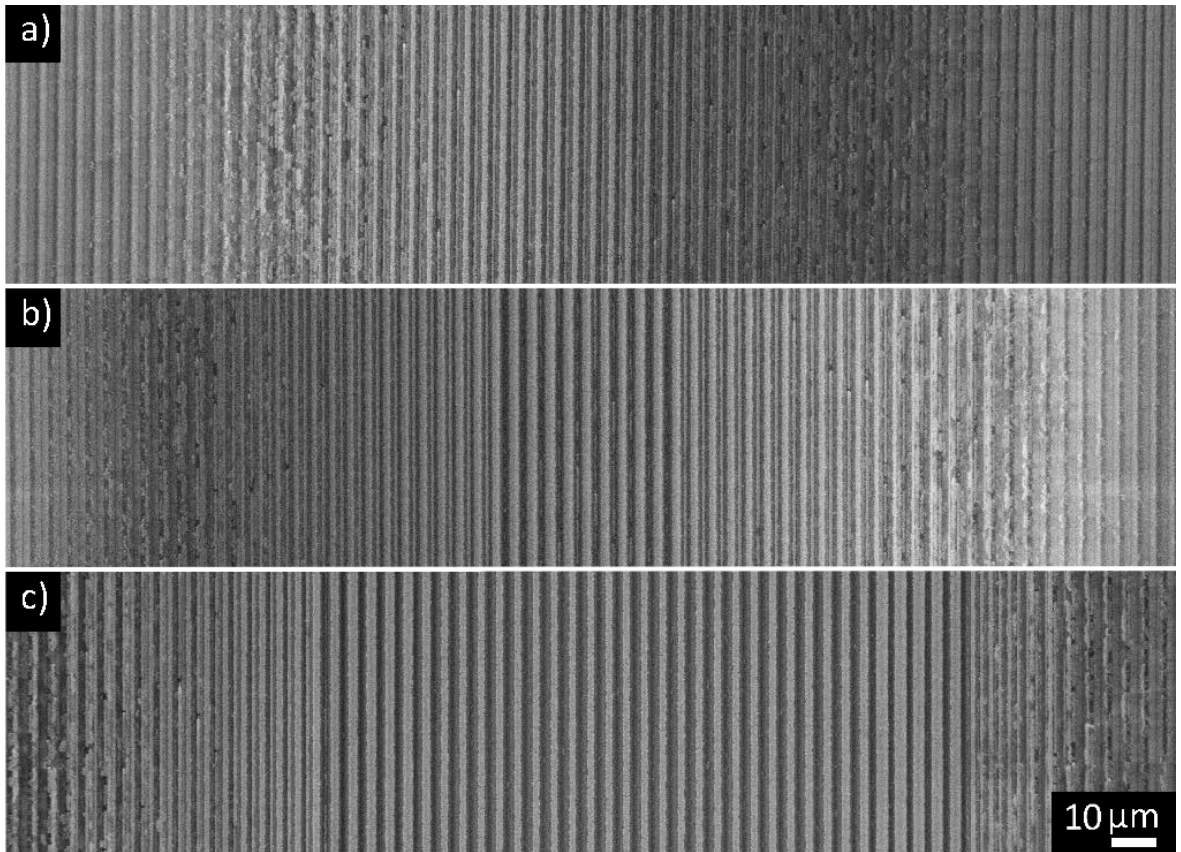Figure 3.19: *SEM micrographs of deposited areas by solution AgD:IPA with dilution ratio 1:129 which was sprayed with process velocity of $2\,mm\cdot s^{-1}$, carrier gas flow rate of a) 16, b) 20 and c) $24\,cm^3 \cdot min^{-1}$ and sheath gas flow rate of $50\,cm^3 \cdot min^{-1}$.*

CG [cm^3·min^{-1}]	d_t [µm]	d_m [µm]	d_h [µm]	d_p [µm]
16	192	98	60	x
20	230	140	40	40
24	280	220	100	133

Figure 3.20: *Width of the total sprayed area (d_t), the main area (d_m), the homogeneous area (d_h) and the plateau area (d_p) depending on the carrier gas flow rate (CG). Demonstrated solution AgD:IPA with dilution ratio 1:129 was sprayed with process velocity of $2\,mm\cdot s^{-1}$ and sheath gas flow rate of $50\,cm^3 \cdot min^{-1}$.*

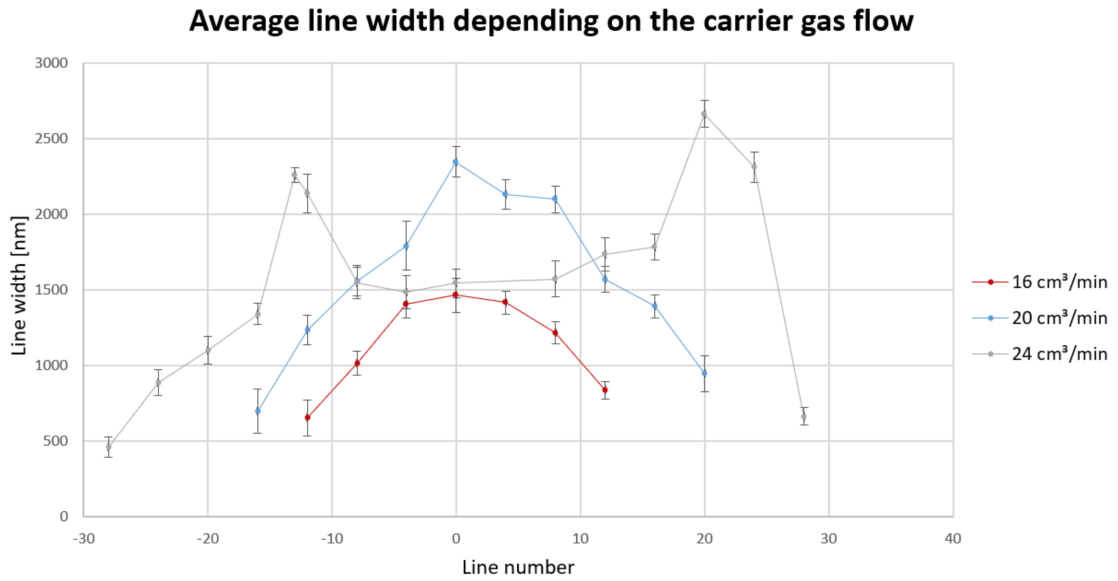Figure 3.21: *Average line width depending on the carrier gas flow calculated from the cross section of sprayed area. Demonstrated solution AgD:IPA with dilution ratio 1:129 was sprayed with process velocity of $2\,mm\cdot s^{-1}$, carrier gas flow rates of 16, 20 and $24\,cm^{3}\cdot min^{-1}$ and sheath gas flow rate of $50\,cm^{3}\cdot min^{-1}$. The unconnected lines are represented by round signs, the squares demonstrate oversprayed area with shortcuts between lines.*

The last parameter considered into the main spraying factors, carrier gas flow, was also investigated with preserved process velocity of $2\,\text{mm}\cdot\text{s}^{-1}$ and sheath gas flow rate of $50\,\text{cm}^{3}\cdot\text{min}^{-1}$. Lines formed with the variation of carrier gas were strongly dependent on the amount of released material. By increasing the amount of released material, more deposited ink was confined into lines and therefore, larger main area with more homogeneous line width was achieved (Figures 3.19, 3.20, 3.21). Nevertheless, by increasing the carrier gas flow rate, the more visible interface between homogeneous area and surrounding overspraying occurred. Borders can be eliminated only with the respect of line width inhomogeneity. Therefore, carrier gas flow has a similar influence but with a higher impact as process velocity and has to be designed with emphasis on a strong influence.

Regarding to later applications, the difference in width of border lines can cause difficulties for large scale structures where spraying one area next to each other can be applied. Lower carrier gas flow is suitable for this type of mass production using step by step process always covering part of already sprayed area. Due to proper design of parameters, any desired area can be sprayed by lines with homogeneous width. These conditions are very convenient for sensor production where additional lines sprayed on plateaus (d_{p}) increase the sensing resolution. On the other hand, very homogeneous line width, necessary for electrical components such as separated wires or size circuits where border lines can be excluded from the device, can be achieved by carrier gas flow increasing.

3.3 Sintering Lines into Conductive Wires and Thermal Reflow of Polymer Substrate

Different wire characteristics are necessary according to the intended application, such as constant wire thickness and width without interruption over the entire length, and insulation between neighbouring wires. In some applications, such as wire grid polarizers, discontinuity can be allowed. But in other cases, wire interruption and shortcuts between wires need to be highly controlled. Generally, the aim of this chapter is to find a postprocess that enables particle sintering into a homogeneous wire with low line edge roughness (LER), reproducibility over long length and without any wire defects. Formed lines, depending on the original width, can be easily interrupted due to particle merging and diffusion which happen during this process. Therefore, two different sintering methods were applied and compared with an emphasis on wire conductivity and number of interruptions which are, depending on application, allowed/not allowed.

The sintering process also affects the thermoplastic substrate. When the structured polymer substrate is heated up to the sintering temperature, substrate flattening can happen as a secondary effect. After the polymer is thermally softened, its surface is flattened due to minimalization of surface energy. This process mainly depends on material T_g and can be easily tuned to gain requirements for further application. [38] The biggest advantage of the polymer substrate flattening is for more structured system fabrication where additional material layers should be applied on a polymer basement. The imprinted structured surface can prohibit or complicate other manufacturing steps. Therefore, thermal reflow can be designed to achieve flattening of the whole structure or the heating can be performed only locally and avoid further deformation or sinking of fabricated structure on specific spots.

In the case of filled V-grooves of PMMA, the substrate was softened by heat during the sintering step when the temperature of 95 °C was applied for 2 min. After the temperature was increased up to 150 °C, the material from the high ridges started to sink, and the shape of the structure became more rounded until all structures were eliminated in the regions where no particles were settled. In the spots where particles covered the bottom of V-grooves, silver wires were formed. Sintered silver kept the bottom of the V-groove shape while the rest of surface was flattened. The slight decrease of angle between surface and sides of V-grooves from original $\sim 54°$ to $\sim 36°$ was calculated from 25 cross-sections. The cross-section area of wires from spin-coated AgD:IPA with ratio 1:59 on polymer substrate is demonstrated in Figure 3.22. Material diffused towards the rough side grains formed higher LER roughness. Therefore, the triangle shape of wire cross-section was slightly shrinked (maximally for 50 nm) in its surface and became wider in the case where LER of wires was higher.
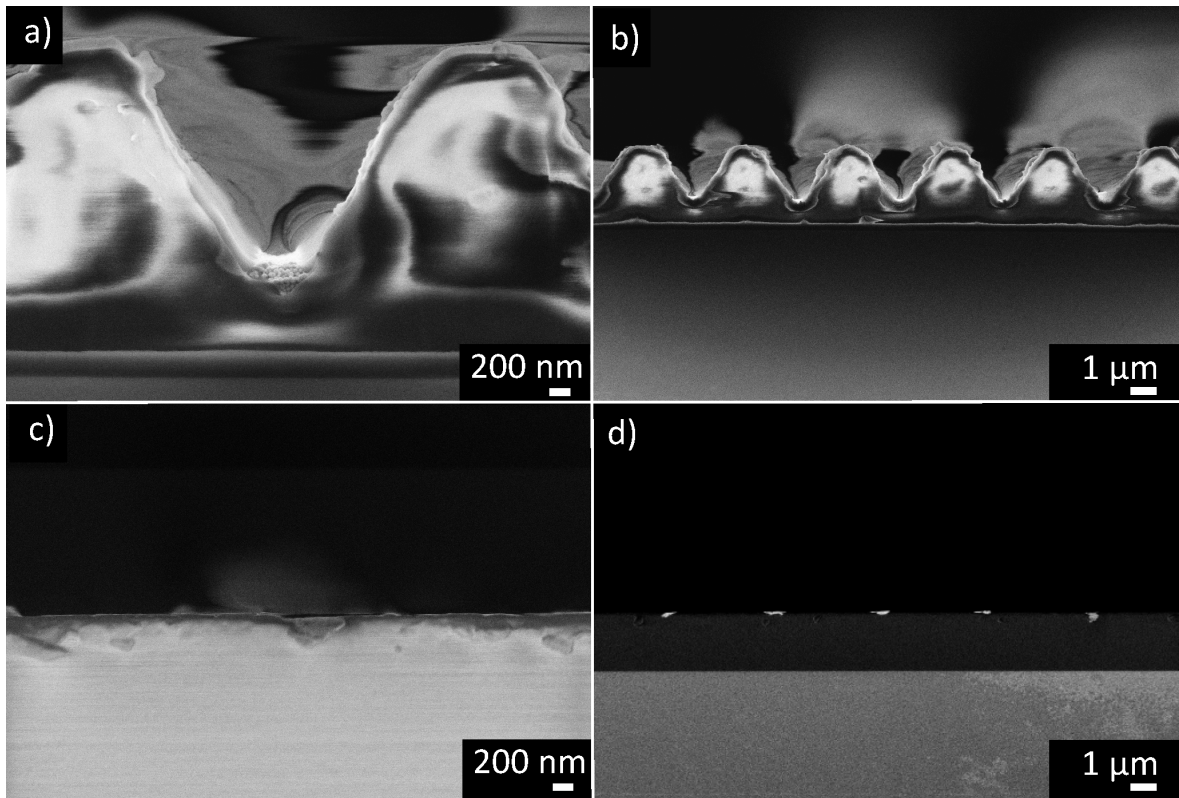
Figure 3.22: *SEM cross-section micrographs for comparison of a), b) non-sintered PMMA structured substrate and c), d) flattened PMMA substrate due to thermal sintering postprocess with a detail of a) non-sintered line and c) sintered wire on the left side and general overview of b) non-sintered lines and d) sintered wires on the right side. Used spin-coated sample with AgD:IPA with dilution ratio 1:59 was sintered for 2 min with 95 °C following by 30 min with the temperature 150 °C.*

3.3.1 Conventional Thermal Sintering

Thermal sintering is a process in which the thin organic layer surrounding particles is removed by heat treatment. For this purpose, a hot plate was used to heat up samples. Temperatures in the range from 140 to 150 °C were applied for their suitability to sinter silver particles. It is very important to keep the temperature under the melting point and as low as possible. Higher temperatures are not allowed for industrial production and cause particle sinking due to polymer melting.

However, ink solution treated with lower temperature has to be sintered for longer time which supports nanoparticle size growth due to diffusion. It can negatively influence wire LER and cause wire interruption. On the other hand, the total surface area decreases due to the particle diffusion, and even higher resolution wires can be obtained. The shrinking process is demonstrated in Figure 3.23 where the dimension of spin-coated wire by AgD:IPA with dilution ratio 1:79 decreased approximately by 38 %, from the original width of 240 nm up to 150 nm. The diffusion into larger grains is also nicely illustrated. Atoms moved by diffusion between grains to lower the grain boundary free energies. [40] Therefore, no other particle content was left to connect two bordering large grains and wire interruptions occurred.
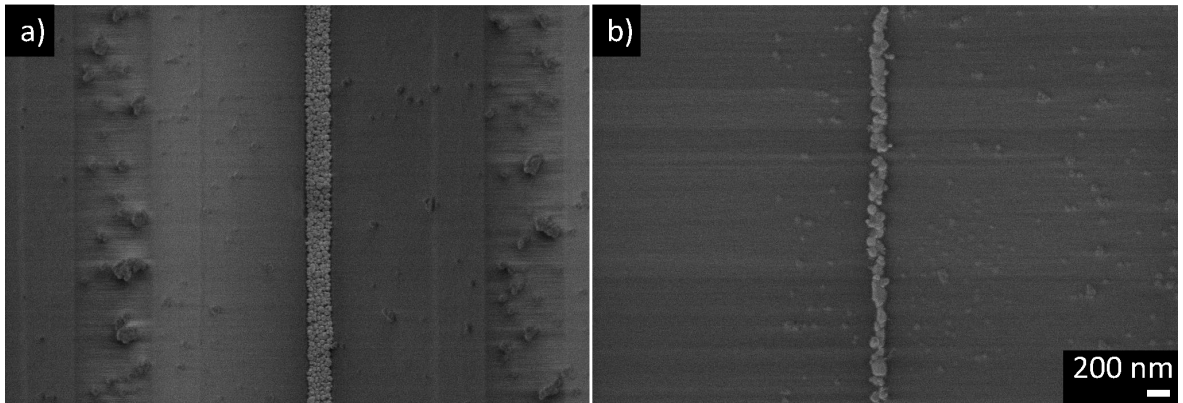
Figure 3.23: *SEM micrographs of a) non-sintered and b) sintered wire spin-coated with AgD:IPA diluted with ratio 1:79.*

With smaller line width, which can be in the case of spin-coating by higher ink dilution, smaller silver content is sustained in V-grooves and therefore more reduced wire width is formed. Theoretically, the thinnest possible obtained wire would be formed from single particles settled and merged in a row with a width of the largest grain. The decrease of wire width with dilution ratio is presented with AgD:IPA solution in Figure 3.24 and Figure 3.25.
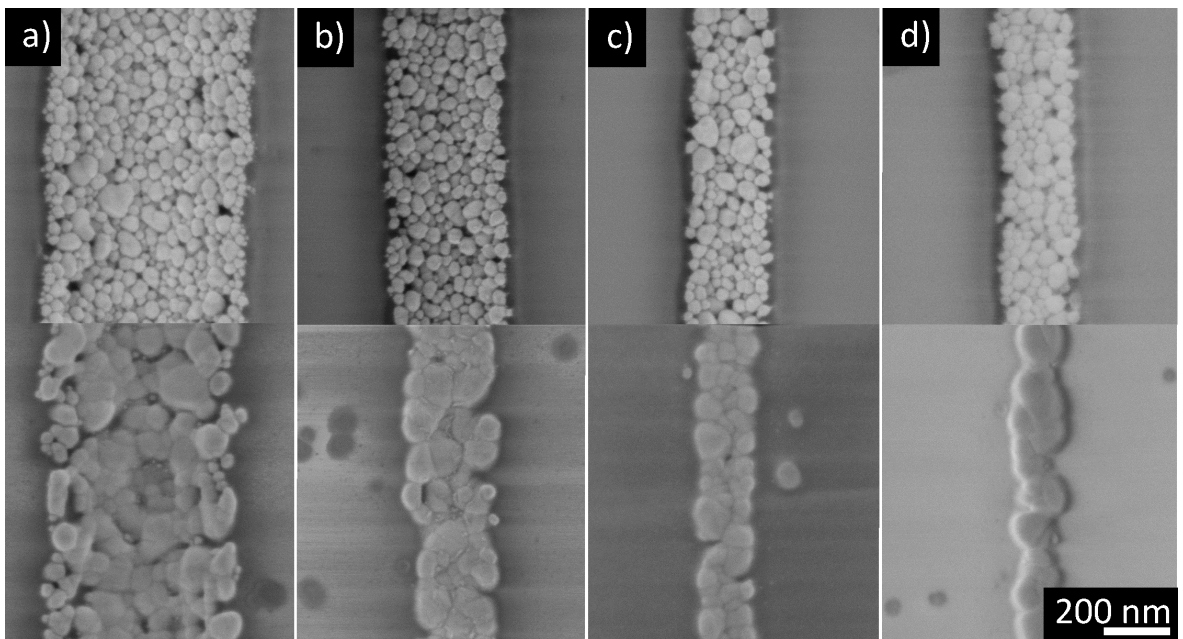
Figure 3.24: *SEM micrographs of spin-coated samples with AgD:IPA diluted with ratio a) 1:59, b) 1:109, c) 1:199, d) 1:259 ratio. Non-sintered samples are on the top and on the bottom, samples sintered for 2 min with 95 °C and for 30 min with the temperature 150 °C are demonstrated.*

dilution ratio	Average Line Width		percentage of shrinkage [%]
	before sintering [nm]	after sintering [nm]	
1:59	731	456	38
1:109	358	228	36
1:199	249	176	29
1:259	217	129	41

Figure 3.25: *Comparison between non-sintered and sintered wire widths with the percentage of shrinkage due to sintering.*

Due to decreasing particle content in the solution and thus in separate V-grooves, high resolution wires with width less than 200 nm can be achieved. The resolution is limited only by particle diffusion and the initial particle size distribution. The silver AgD ink has a particle size distribution of (49 ± 15) nm where the largest measured grains were measured to be 80 nm which should grant the thinnest possible wire width. But because of the high grain grow and diffusion, at least one hundred nm wide wires were reasonable. Thinner wires can suffer by large amount of defects, mainly interruptions. Even with the dilution 1:259, the approx. 150 nm wide wires possessed at least one interruption on each 8.3 µm of the wire (counted from a 225 µm long section). On the other hand, the wires spin-coated with the ratio 1:259 were formed by only one grain and compared to others obtained very low LER. Defects such as interruptions shall not be a problem for grid polarizers where very thin wires with very low LER are highly required. For some electrical components however, interruptions would not be tolerated. Therefore, the adequate conditions to decrease probability of wire defects have to be chosen dependently on later wire application.

Different strategies were tested to reduce the number of wire interruptions and to understand the ink behaviour more during sintering. First, sintering temperature was decreased to 140 °C to avoid a particle diffusion. To compare these conditions with sintering by 150 °C, preheating step of 2 min with 95 °C and the sintering time 30 min was kept. Silver recrystallization should start already from 60 °C. [39] At higher temperatures, the grain growth accelerates and thus the probability of defects increases. However, higher temperature needs to be applied to remove organic additives which are included in the ink solution to inhibit particle agglomeration. Particles were also coagulated into large grains but nevertheless, some smaller particles still covered by organic material were maintained separately (Figure 3.26). Since not all particles were merged with the formed complex, wires were categorized as non-sintered.
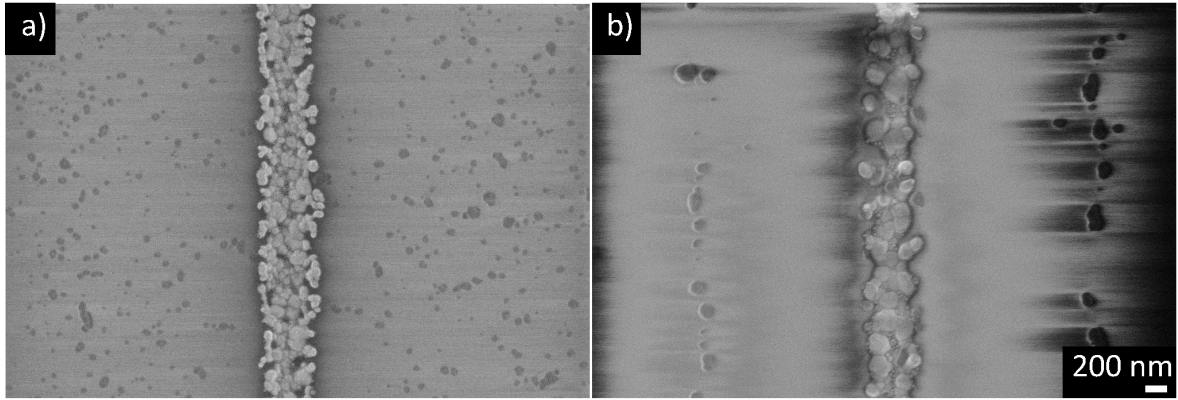
Figure 3.26: *SEM micrographs of spin-coated samples with AgD:IPA with dilution ratio 1:59 sintered for 2 min at temperature 95 °C and then heated up to a) 150 °C, b) 140 °C when the sintering time is conserved at 30 min.*

Therefore, the lowest possible temperature, 150 °C, for organic elimination was preserved and different sintering times were chosen to see the sintering process. The sufficiency of sintering will be more analysed in Chapter 3.4 with an emphasis to a wire conductivity. Particle necking occurred already after 1 minute when the silver started to diffuse and connect to neighbouring grains, and by 20 min of sintering the area was almost equalized. The grain growth is shown in Figure 3.27 and Figure 3.28 where from the initial approximately 50 nm small particles a grain sizes of 86, 164, 178, 183, 192 and 290 nm were achieved at 1, 5, 10, 20 and 30 minutes of sintering, respectively.

Additionally, voids between particles begun to shrink due to necking during sintering and thus the volume and wire width was reduced. The dependency of wire widths on the sintering time is presented in Figure 3.29, together with LER. The longer sintering time was, the more visible was the shrinkage of the line widths along with higher roughness. The material from wire edges was being transported to the middle area where bigger grains were formed by diffusion. Therefore, a lack of silver was at the edge which would otherwise unite neighbouring grains. Less material resource was kept in time due to continuous shrinkage of width by diffusion into other grains. Thus, the LER was increasing forward in time. The calculation of line width can be made in 2 ways for different applications. For LER calculation, the normal width, containing the measurement of the furthest crossing points compared to the middle of the wire, was considered. Initial roughness of about 25 nm significantly increased after around 20 minutes. At that time, the diffusion into the middle area grains mainly happened and continued until reaching LER about 115 nm after 30 minutes.
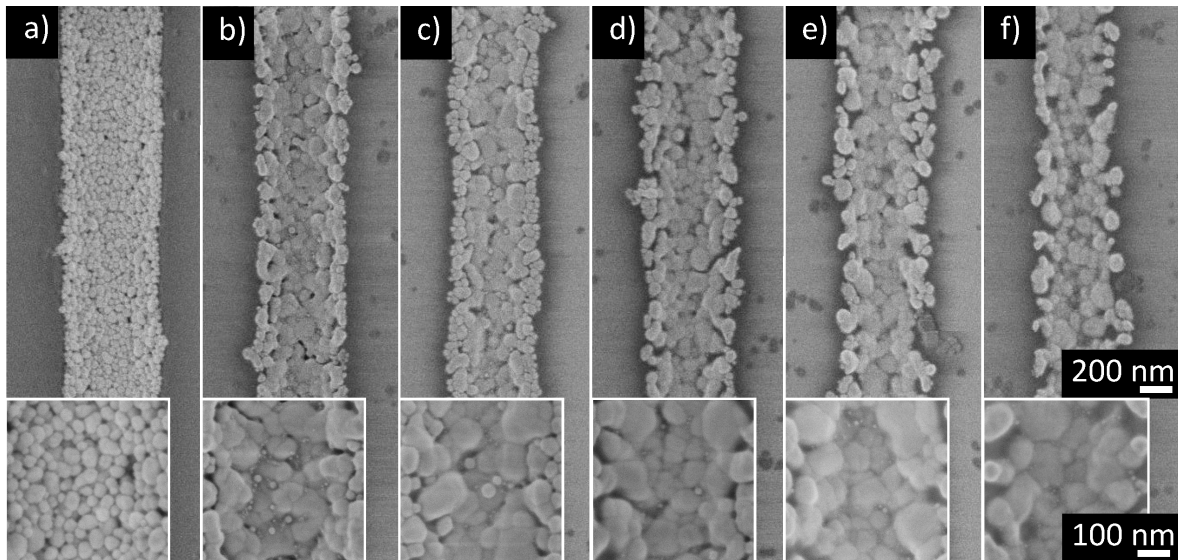
Figure 3.27: *SEM micrographs of grain growth comparison while spin-coated samples with AgD:IPA with dilution ratio 1:59 were a) not sintered and sintered for b) 1 min, c) 5 min, d) 10 min, e) 20 min, f) 30 min with temperature of 150 °C.*
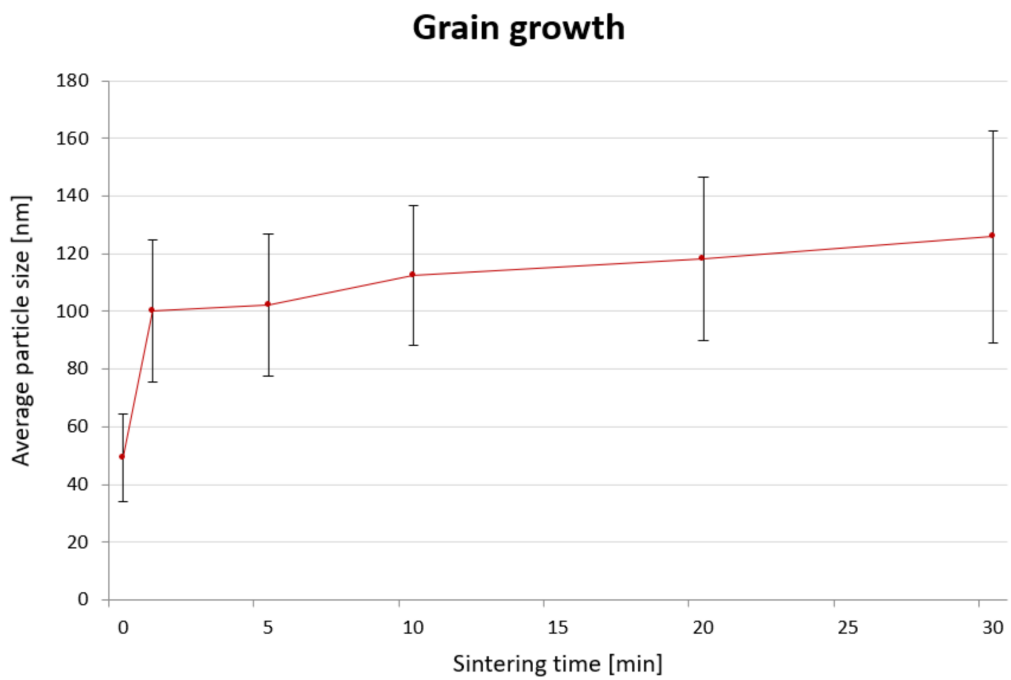
Figure 3.28: *Average particle size before and after 1 min, 5 min, 10 min, 20 min, 30 min of sintering with temperature of 150 °C.*
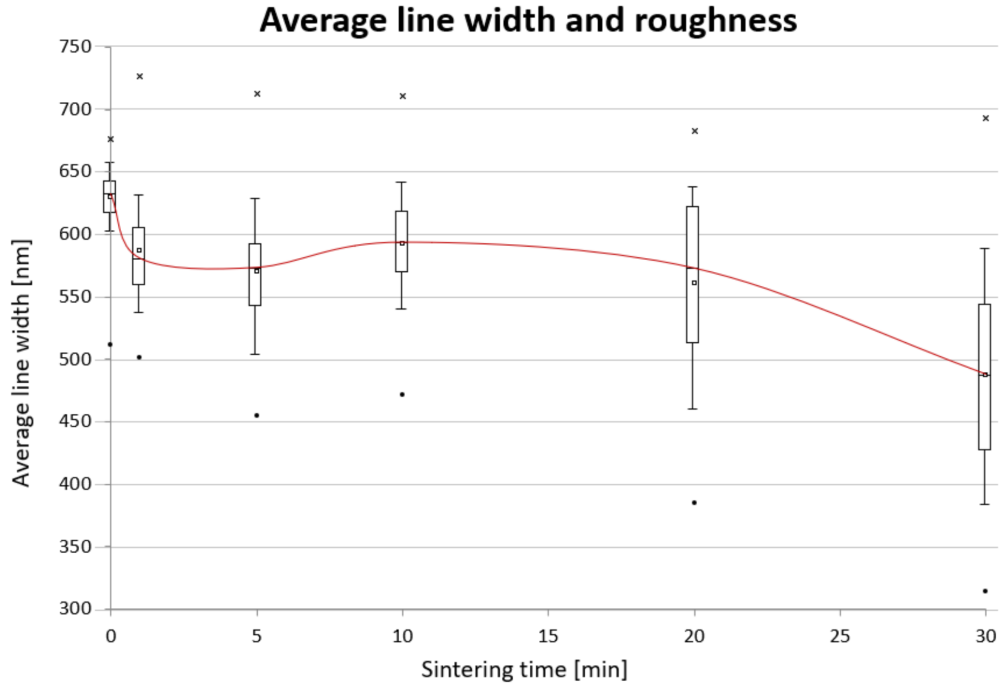
Figure 3.29: *Average line width and roughness before and after 1 min, 5 min, 10 min, 20 min, 30 min of sintering with temperature of 150 °C.*

3.3.2 Flash Lamp Annealing (FLA)

To avoid wire interruptions, minimal grain growth due to particle diffusion was needed. Therefore, flash lamp annealing (FLA) where a low thermal exposure is achieved by short duration high intensity pulse was applied. Surface flattening could be realized depending on sintering conditions too.

The influence of sintering time is shown in Figure 3.30. The ultra-short annealing time inhibited most of the bulk diffusion due to the rapid cooling of the sample after exposure (< 10 s depending on applied energy density determined by selected parameters). As the voltage was preserved at 800 V, the sintering energy density was increased by pulse duration (Figure 3.31). With higher annealing energy density, particle contact area increased due to material diffusion but with apparently not so evident grain growth compared to conventional thermal sintering.
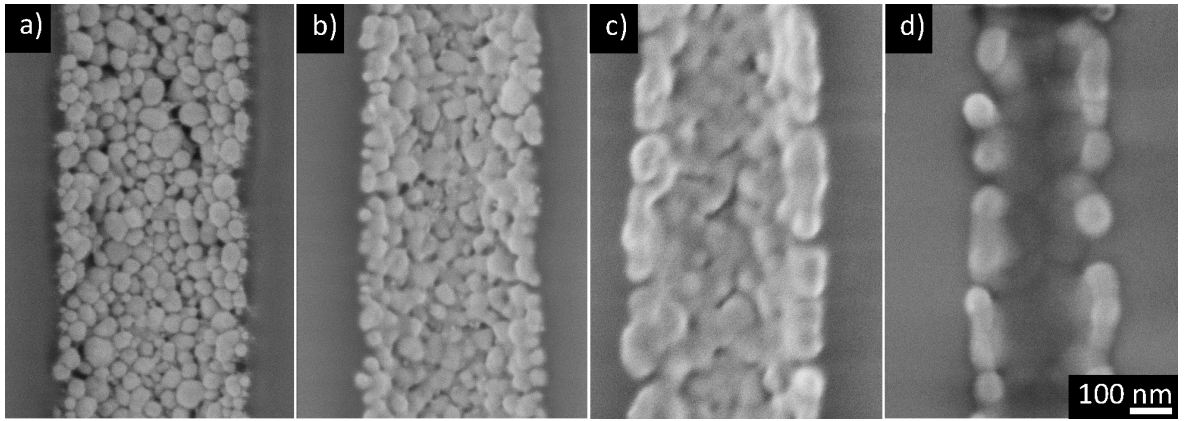
Figure 3.30: *SEM micrographs of spin-coated lines with AgD:IPA diluted with ratio 1:59 sintered by one pulse with duration a) 100 μs, b) 300 μs, c) 500 μs and d) 1000 μs with voltage 800 V.*

number of pulses	t [μs]	V [V]	E [J·cm^{-2}]
1	100	800	1.46
1	300	800	5.10
1	500	800	8.47
1	1000	800	15.60

Figure 3.31: *Dependency of energy density on annealing time while the voltage is preserved.*

Established duration time should preserve from the grain growth and thus more obvious energy density influence can be demonstrated while different voltage was applied. The dependency of sintering energy density on different voltage with retained annealing time at 500 μs is shown in Figure 3.32. Applied parameters are presented in Figure 3.33.

The absorbed energy density $4.7\,\mathrm{J \cdot cm^{-2}}$ was not sufficient to merge particles together (Figure 3.34). The necking of particles started to be observed with higher energy light pulses. It is demonstrated on the line width (Figure 3.35) where the width strongly dropped after a light pulse with the voltage 700 V containing energy density $5.8\,\mathrm{J \cdot cm^{-2}}$. The organic surfactant prohibiting particle coalescence evaporated due to the applied energy and thus particles slightly rearranged due to diffusion. It is the similar line shrinkage phenomenon which occurred also during the conventional thermal sintering. After particle reorganization, material was not diffused into large grains and no other significant line shrinkage was observed. Therefore, the edge line roughness is not significantly increased during flash lamp annealing which is the main advantage of this technique. The LER change between samples sintered by pulses with 750 V and 900 V was only 6 nm comparing Q3 and Q1 quartile to the median (Figure 3.35).

With higher energy intensity, the surface of PMMA also flattened which can be suitable for later applications. Depending on the velocity of substrate movement, the line edges slightly folded toward the middle axis. The line was then placed a little bit deeper into the substrate which caused a transformation from the V-shape cross-section into U-shape. It demonstrated that the application of too high energy density

can cause sinking of wires into the substrate due to polymer melting and generate uncontrollable grain growth (with grain size > 200 nm).
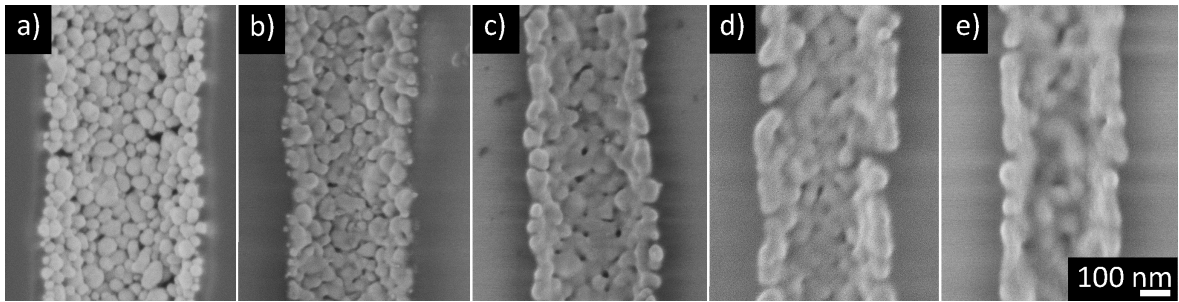
Figure 3.32: *SEM micrographs of spin-coated lines with AgD:IPA diluted with ratio 1:59 sintered by one pulse with duration 500 μs and voltage a) 650 V, b) 700 V, c) 750 V, d) 800 V, e) 850 V and f) 900 V.*

number of pulses	t [μs]	V [V]	E [J· cm^{-2}]
1	500	650	4.63
1	500	700	5.80
1	500	750	7.06
1	500	800	8.47
1	500	850	10.10
1	500	900	11.80

Figure 3.33: *Dependency of energy density on annealing time while the voltage is preserved.*
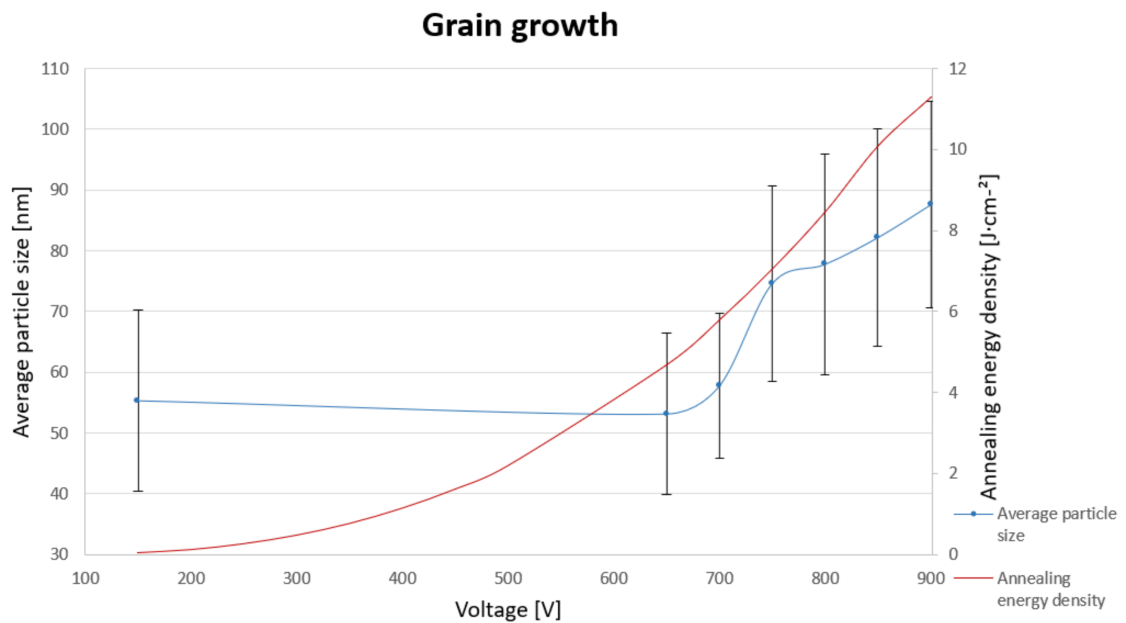
Figure 3.34: *Average particle size (spin-coated AgD:IPA with dilution ratio 1:59) depending on the voltage with the corresponding annealing energy density.*

52
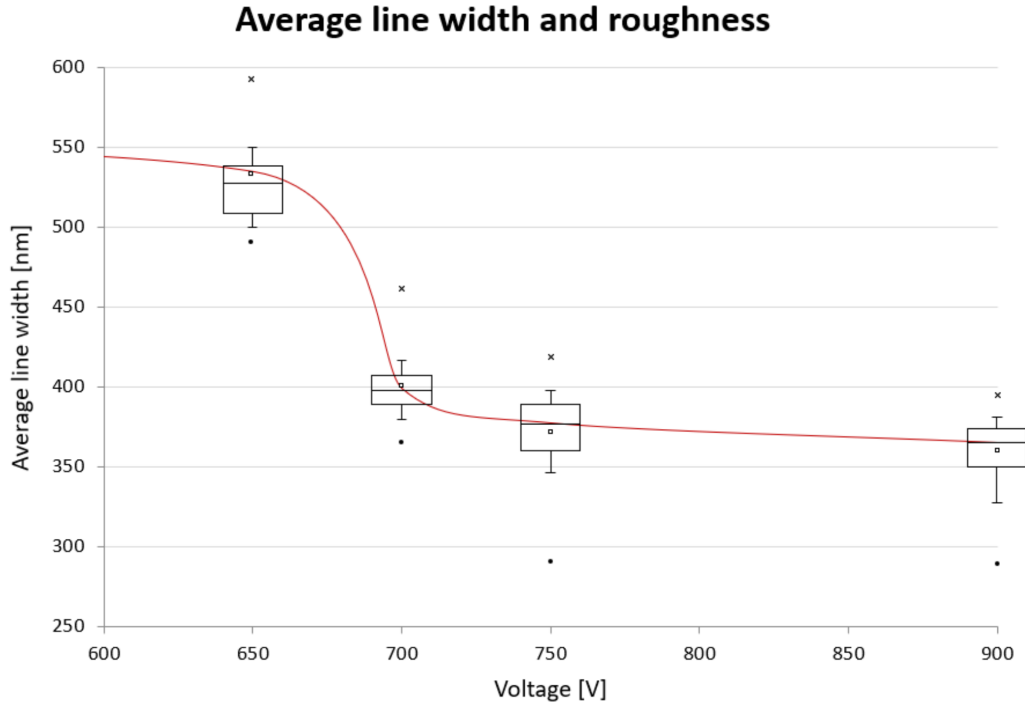
Figure 3.35: *Dependency of average line width and roughness (spin-coated AgD:IPA with dilution ratio 1:59) on the voltage while the annealing time is preserved at 500 μs.*

FLA technique possess many parameters with which the final wire structure can be influenced e.g. annealing time, voltage. As it was demonstrated, the energy density required for efficient sintering can be applied by increasing voltage while sintering time is preserved. Thus, the final wire appearance and defects can be more controlled than in the case of thermal heat sintering. One not discussed parameter, number of applied pulses, was not investigated for large complexity of the topic and therefore it is suggested for further research.

3.4 Measurement of Electrical Resistivity

Electrical resistivity measurements were determined on spin-coated samples with solution AgD:IPA with dilution ratio 1:59. Spin-coated lines with higher dilution ratios possessed less assembled particles and therefore had bigger tendency to be interrupted after sintering due to grain growth. While spin-coated samples with 1:59 dilution ratio were intact wires almost without any interruptions, samples spin-coated by solution with dilution ratio 1:259 consisted of wires interrupted around each 8 μm of their length. Measuring of these short non-interrupted parts would lead to high error value of measurement. Equation 2.1 from the theoretical part was used for calculation of resistivity considering distances between pads, number of measured wires and cross-section areas. The effective width considering the closest border points measured by perpendicular line to the middle axis of wire, was used to avoid errors caused by high LER due to granular shape of wires. Therefore, wire widths of 532, 487, 468, 429, 389, 402 and 380 nm were collected in the specific sintering times 1, 5, 10, 20, 30 minutes and after

applying 750 and 900 V and used for cross-section area calculation. Thus, the electrical resistivity of an average single wire was obtained. The description of all measurement processes is described in Experimental Part.
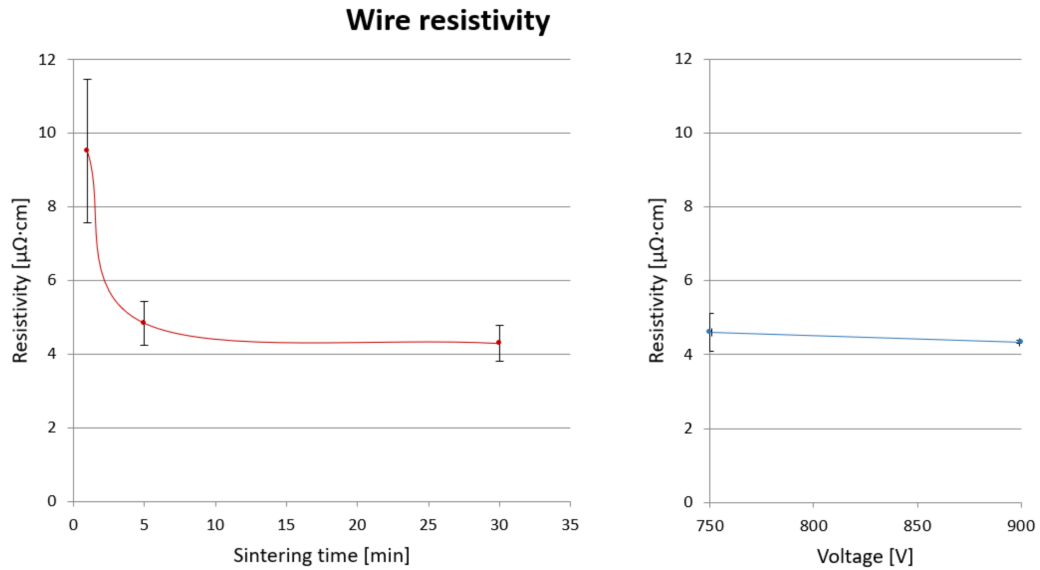
Figure 3.36: *Measured resistivity of wires after conventional thermal sintering (demonstrated by red line) on the left side and flash light annealing on the right side. Demonstrated sample was spin-coated with solution AgD:IPA with dilution ratio 1:59 for 180 s with 5000 rpm velocity.*

Measured data correlated with values included in Genes'Ink data sheets (resistivity of $4.25 \cdot 10^{-6}$ Ω·cm or lower after 3 minutes of sintering at $150\,°C$) which confirmed the successful sintering and therefore, the suitability of both sintering techniques (conventional sintering and flash light annealing).

Very high resistivity in the range of 10^{-4} Ω·cm was measured for unsitered ink which demonstrates the presence of organic layer separating each particle and therefore inhibiting their connections (Figure 3.36). The surfactant removing process can be seen already at 1 minute of sintering process when the measured resistivity was already $9.52 \cdot 10^{-6}$ Ω·cm. Particles were already necking with decreasing volume of voids. Then the resistivity significantly dropped to $4.84 \cdot 10^{-6}$ Ω·cm presenting 5 minutes of sintering. After 10 min of sintering, the voids almost disappeared and therefore only slight enhancement of wire resistivity was observed in comparison of resistivity $4.29 \cdot 10^{-6}$ Ω·cm measured after 30 min of sintering.

The similar resistivity of 4.59 and $4.34 \cdot 10^{-6}$ Ω·cm sintered with 750 V and 900 V for wires treated by flash light annealing was measured (Figure 3.36). In this case, wires sintered with 750 V showed similar appearance and resistivity as after 5 minutes of thermal sintering and can be used for comparison of both techniques. More analysed wire properties collected after specific times or light pulses used during processes are summarized in Figure 3.37.

Sintering process		d_a [nm]	d_m [nm]	LER (Q3-Q1) [nm]	ρ [Ω·cm]
No sintering		49.1	86.0	43580.0	~ 10^{-4}
Conventional thermal sintering	1 min	100.0	164.6	45.7	$9.52 \cdot 10^{-6}$
	5 min	102.2	178.3	49.5	$4.84 \cdot 10^{-6}$
	10 min	112.5	182.6	48.8	
	20 min	118.4	191.6	108.6	
	30 min	126.0	290.2	115.4	$4.29 \cdot 10^{-6}$
Flash light annealing	750 V	74.6	102.3	30.7	$4.59 \cdot 10^{-6}$
	900 V	87.6	119.6	24.9	$4.34 \cdot 10^{-6}$

Figure 3.37: *Summary of measured wire properties before and after sintering including average (d_a) and maximal (d_m) particle diameter, line edge roughness (LER) and electrical resistivity (ρ).*

As it was already mentioned in the previous chapters, the longer sintering time is, the larger grain growth occurs and the probability of wire interruptions increases. Therefore, short annealing times are recommended for sub-micrometer wire treatment. Flash light annealing, with sintering sufficiency comparable with conventional thermal sintering, can lower this probability by preserving low wire LER. Due to application of very short light pulses, electrical wire conductivity can be reached with high efficiency.

Depending on the later application of fabricated structure, wire interruptions do not need to cause obstacle for device usability e.g. interdigitated electrode arrays used as sensors or optical gratings but can significantly decrease its efficiency. Nevertheless, in other applications where wires are implemented into circuits, the interruptions can cause collapse of the whole structure. Therefore, the chosen techniques with sintering parameters is very important.

Conclusion

The aim of the diploma thesis was to develop a fabrication process which would replace the expensive techniques used nowadays for micro-electronic manufacture. For this purpose, two methods, spin-coating and aerosol jet printing, based on applying nanoparticle-based silver inks on pre-patterned polymer substrates were designed.

The high resolution of fabricated structures was achieved by proper design of pre-patterned polymer substrates with a specific sub-micrometer topography, both locally and by specific vertical shapes. V-groove shapes separated by plateaus allowed the wet deposited ink to confine within the capillaries in a defined way and thus enabled a resolution much smaller than the resolution of the applied additive processes and even the V-groove profiles. Since the substrate pattern allows the control over the location and shape of the fabricated structure, diverse solid or flexible electronic architectures containing capillaries for ink storage of different depths and widths can be achieved by the suggested methods.

As it was demonstrated, spin-coating allows very homogeneous line fabrication over a large area due to centrifugal force. Therefore, it is a very suitable technique for large structure production where the same wire widths for all included structures are necessary e.g. large electrode arrays or optical gratings. For example, lines formed by applying of solution AgD:IPA with a dilution ratio 1:59 spin-coated for 120 s with the process velocity of 5000 rpm possessed line width ~ 730 nm due to the substrate with grating of period almost 313 V-grooves/mm with the height 2,3 µm and width 3,2 µm of each V-groove. Thinner lines can be easily achieved by increasing the dilution ratio of the solution which shows very easy customization of the technique. The only limitation is in the utilization of a substrate containing also other patterned electronic components. Spin-coating covers the entire substrate by a thin layer of ink and hence other prepatterned structures on the substrate are influenced too. This provides a disadvantage if there is a requirement for filling of only specific structures.

In case there is a presence of other structures on the substrate intended for coverage, aerosol jet printing overcomes the limitation of spin-coating due to its addressability. Aerosol jet printing has the advantage of ink deposition control, thus enabling narrower lines use of a range of inks with different solvent contents, local deposition on topography and even 3D surfaces, fully addressable according to computer aided designs. This technique also offers homogeneous line fabrication by spraying a wider beam which can cover many wires, whole circuits or other structures depending on their size by one sprayed line. Up-scaling of the technique can be reached by multiple sprayed areas placed next to each other which can also compete to spin-coating. Another advantage of aerosol jet printing consists of the possibility to use more types of ink. Different inks can be switched or mixed together and applied during spraying which can add the device new properties e.g. improved conductivity. It is very convenient for ink designing for specific applications.

The same solution of silver ink but with much higher dilution ratios was applied by

wet deposition to observe the effect of aerosol jet printing on the pattern substrate. To briefly summarize some of the most important investigated parameters influencing the process (Figure 3.38), two main representative applications are considered regarding to later applications.

variation of process parameter → effect				
	d_t [µm]	d_m [µm]	d_h [µm]	d_p [µm]
↑ velocity of lateral nozzle movement	↑	↓	↑	↓
↑ Sheath gas	↓	↓	↓	↓
↑ Carrier gas	↑	↑	↑	↑

Figure 3.38: *Summarization of the main investigated parameters influencing the total sprayed area (d_t), the main area (d_m), the homogeneous area (d_h) and the plateau area (d_p) of the sprayed area.*

The large scale structures such as sensors where the additional formed lines on plateaus even increase the sensing area can be prepared with step by step spraying process when the part of already sprayed area is again covered. The difference between the widths of lines at the border of d_h and in the middle of the d_m is very important for this step process. It can be eliminated by decreasing the carrier gas flow and the lateral nozzle movement velocity. Process velocity also supports higher filling of V-grooves and thus increasing the sensing area. Additionally, more homogeneous obtained line width with lower overspraying effect can be achieved by decreasing the sheath gas flow.

On the other hand, very homogeneous line width is necessary for electrical components such as separated wires or size circuits where the difference of border line widths is not important and these lines can be excluded from the device. For these components, the higher carrier gas flow is recommended together with combination of high nozzle movement velocity. The low sheath gas flow with higher ink dilution ratio furthermore increase the line width homogeneity by beam defocusing.

Proper design of parameters allows the spraying of any desired area which results in lines with quite homogeneous width. The later application varies mainly on the line width homogeneity and the permission of the width difference between lines on the border of d_h and in the middle of the d_m. Theoretically, the area containing homogeneous width of lines reached by decreasing the sheath gas flow and atomization of high dilution ink is limited only by the aerosol jet printing device.

The fabrication process is followed by a sintering postprocess to further tune resolution, achieve conductivity of formed structures and additionally flatten the polymer substrate which increases the usability for electronics application. Two techniques, conventional thermal sintering and flash light annealing were compared, and the achieved wire conductivity was discussed. Fabricated structures had significant line shrinkage of about 30 to 40 % by conventional thermal sintering treatment. On the other hand, strong grain growth was inhibited by ultra-short pulses applied during flash light annealing and thus wire interruptions were eliminated which increased the product application.

The suggested processes showed many advantages in the way of very fast fabrication without any requirements of specific printing ink or substrate. Therefore various

"green chemistry" inks can be applied with respect to the environment on any type of prepatterned substrate. It also allows deposition on polymer foils which represent the main substrate suitable for flexible electronics which allows new mechanical properties and therefore novel product applications. Manufactured sub-micrometer electrically conductive structures can be easily designed by adjustment of the solvent content and deposition parameters depending on the chosen method and thus fulfill application requirements. With the emphasis on the efficiency, up-scalability and versatility, the described low-cost process can be considered as a next generation method for industrial flexible micro-electronic production.

List of Abbreviations

Ag	silver
AJP	aerosol jet printing
Al	aluminium
Au	gold
C	carbon
Cu	copper
FLA	flash light annealing
Hg	mercury
CHF_3	trifluoromethane
IPA	isopropylalcohol
LER	line edge roughness
M_w	molecular weight
N_2	nitrogen
Ni	nickel
O_2	oxygen
PAR	polyarylate
PC	polycarbonate
PDMS	poly(dimethylsiloxane)
PEDOT	poly(3,4-ethylenedioxythiophene)
PI	polyimide
PMMA	poly(methyl methacrylate)
PEN	polyethylene naphthalate
PES	poly(ether sulfone)
PET	polyethylene terephthalate
PSS	poly(styrene sulfonate)
PU	polyurethane
RIE	reactive-ion etching
SEBS	styrene–ethylene–butadiene–styrene
Si_3N_4	silicon nitride
TMP	2,2,4-trimethyl pentane
d_h	homogeneous area
d_p	plateau area
d_m	main area
d_t	total sprayed area
L	wire length
n	number of wires
R	resistance
T_g	glass-transition temperature
w_{eff}	wire effective width
ρ	resistivity
σ	conductivity

Bibliography

[1] Horváth, Barbara, Barbora Křivová, Sami Bolat, and Helmut Schift. 2019. Fabrication of Large Area Sub-200 nm Conducting Electrode Arrays by Self-Confinement of Spincoated Metal Nanoparticle Inks. *Advanced Materials Technologies* 1800652: 1–11. `https://doi.org/10.1002/admt.201800652`.

[2] Horvath, Barbara, Barbora Křivová, and Helmut Schift. 2019. Nanoimprint Meets Microfluidics: Development of Metal Wires from Nanoparticle Ink Filled Capillaries. *Micro and Nano Engineering* 3 (November 2018): 22–30. `https://doi.org/10.1016/j.mne.2019.02.004`.

[3] Stulik, J., and A Hamacek. Carbon Nanotubes Ammonia Sensor Printed by Aerosol Jet System. *University of West Bohemia* 0–3. `https://passive-components.eu/wp-content/uploads/2017/10/4.5.-UWB-Jiri-Stulik.pdf`

[4] Wang, Chia, Guan Yi Hong, Kuan Ming Li, and Hong Tsu Young. 2017. A Miniaturized Nickel Oxide Thermistor via Aerosol Jet Technology. *Sensors* 17 (11). `https://doi.org/10.3390/s17112602`.

[5] Mattana, Giorgio, and Danick Briand. 2016. Recent Advances in Printed Sensors on Foil. *Materials Today* 19 (2): 88–99. `https://doi.org/10.1016/j.mattod.2015.08.001`.

[6] Rieu, Mathilde, Malick Camara, Guy Tournier, Jean Paul Viricelle, Christophe Pijolat, Nico F. de Rooij, and Danick Briand. 2016. Fully Inkjet Printed SnO_2 Gas Sensor on Plastic Substrate. *Sensors and Actuators*, B: Chemical 236: 1091–97. `https://doi.org/10.1016/j.snb.2016.06.042`.

[7] Secor, Ethan B., Sooman Lim, Heng Zhang, C. Daniel Frisbie, Lorraine F. Francis, and Mark C. Hersam. 2014. Gravure Printing of Graphene for Large-Area Flexible Electronics. *Advanced Materials* 26 (26): 4533–38. `https://doi.org/10.1002/adma.201401052`.

[8] Gao, Wei, Hiroki Ota, Daisuke Kiriya, Kuniharu Takei, and Ali Javey. 2019. Flexible Electronics toward Wearable Sensing. Research-article. *Accounts of Chemical Research* 52: 523–33. `https://doi.org/10.1021/acs.accounts.8b00500`.

[9] Kayser, Laure V., and Darren J. Lipomi. 2019. Stretchable Conductive Polymers and Composites Based on PEDOT and PEDOT:PSS. *Advanced Materials* 31 (10): 1–13. `https://doi.org/10.1002/adma.201806133`.

[10] Eckstein, Ralph, and U. Lemmer. 2016. Aerosol Jet Printed Electronic Devices and Systems, 192. `http://digbib.ubka.uni-karlsruhe.de/volltexte/1000065424`.

[11] Fukuda, Kenjiro, Yudai Yoshimura, Tomoko Okamoto, Yasunori Takeda, and Daisuke Kumaki. 2015. Reverse-Offset Printing Optimized for Scalable Organic Thin-Film Transistors with Submicrometer Channel Lengths, 1–6. `https://doi.org/10.1002/aelm.201500145`.

[12] Leppäniemi, Jaakko, Olli Heikki Huttunen, Himadri Majumdar, and Ari Alastalo. 2015. Flexography-Printed Ni_2O_3 Semiconductor Layers for High-Mobility Thin-Film Transistors on Flexible Plastic Substrate. *Advanced Materials* 27 (44): 7168–75. `https://doi.org/10.1002/adma.201502569`.

[13] Li, Hongpeng, and Jiajie Liang. 2019. Recent Development of Printed Micro - Supercapacitors: Printable Materials, Printing Technologies, and Perspectives. Advanced Materials 1805864: 1805864. `https://doi.org/10.1002/adma.201805864`.

[14] Kamyshny, Alexander, and Shlomo Magdassi. 2018. Conductive Nanomaterials for 2D and 3D Printed Flexible Electronics.*Chemical Society Reviews*, 1712–40. `https://doi.org/10.1039/c8cs00738a`.

[15] Venkata Krishna Rao, R., K. Venkata Abhinav, P. S. Karthik, and Surya Prakash Singh. 2015. Conductive Silver Inks and Their Applications in Printed and Flexible Electronics. *RSC Advances* 5 (95): 77760–90. `https://doi.org/10.1039/c5ra12013f`.

[16] Efimov, A. A., P. V. Arsenov, N. V. Protas, K. N. Minkov, M. N. Urazov, and V. V. Ivanov. 2018. Dry Aerosol Jet Printing of Conductive Silver Lines on a Heated Silicon Substrate. *IOP Conference Series: Materials Science and Engineering* 307 (1). `https://doi.org/10.1088/1757-899X/307/1/012082`.

[17] Primeau, Brian C., Goldie L. Goldstein, and John E. Greivenkamp. 2012. Exploring the Performance of Indoor Localization Systems Based on VLC- RSSI, Including the Effect of NLOS Components Using Two Light-Emitting Diode Lighting Systems. *Optical Engineering* 51 (6): 064301. `https://doi.org/10.1117/1.OE`.

[18] Schift, H, and J. Ahopelto. 2008. Library of Processes - Nanopatterning, Production and Applications Based on Nanoimprint Lithography. `https://doi.org/10.1016/j.avsg.2007.07.015`.

[19] Zhang, Yan, Lina Zhang, Kang Cui, Shenguang Ge, Xin Cheng, Mei Yan, Jinghua Yu, and Hong Liu. 2018. Flexible Electronics Based on Micro/Nanostructured Paper. *Advanced Materials* 30 (51): 1–39. `https://doi.org/10.1002/adma.201801588`.

[20] Chen, Yong, and Anne Pépin. 2001. Review Nanofabrication: Conventional and Nonconventional Methods Miniaturization. *Electrophoresis* 22: 187 – 207.

[21] Ligon, Samuel Clark, Robert Liska, Jürgen Stampfl, Matthias Gurr, and Rolf Mülhaupt. 2017. Polymers for 3D Printing and Customized Additive Manufacturing. *Chemical Reviews* 117 (15): 10212–90. `https://doi.org/10.1021/acs.chemrev.7b00074`.

[22] Ligon, Samuel Clark, Robert Liska, Jürgen Stampfl, Matthias Gurr, and Rolf Mülhaupt. 2017. Polymers for 3D Printing and Customized Additive Manufacturing. *Chemical Reviews* 117 (15): 10212–90. `https://doi.org/10.1021/acs.chemrev.7b00074`.

[23] Hyun, Woo Jin, Ethan B. Secor, Mark C. Hersam, C. Daniel Frisbie, and Lorraine F. Francis. 2015. High-Resolution Patterning of Graphene by Screen Printing with a Silicon Stencil for Highly Flexible Printed Electronics. *Advanced Materials* 27 (1): 109–15. `https://doi.org/10.1002/adma.201404133`.

[24] Sowade, Enrico, Thomas Blaudeck, and Reinhard R. Baumann. 2015. Inkjet Printing of Colloidal Nanospheres: Engineering the Evaporation-Driven Self-Assembly Process to Form Defined Layer Morphologies. *Nanoscale Research Letters* 10 (1): 0–8. `https://doi.org/10.1186/s11671-015-1065-2`.

[25] Lone, Saifullah, Jia Ming Zhang, Ivan U. Vakarelski, Er Qiang Li, and Sigurdur T. Thoroddsen. 2017. Evaporative Lithography in Open Microfluidic Channel Networks. *Langmuir* 33 (11): 2861–71. `https://doi.org/10.1021/acs.langmuir.6b03304`.

[26] Aerosol Jet System Configurations. Optomec, Inc. `https://www.optomec.com/printed-electronics/aerosol-jet-printers/`.

[27] Salary, Roozbeh (Ross), Jack P. Lombardi, M. Samie Tootooni, Ryan Donovan, Prahalad K. Rao, Peter Borgesen, and Mark D. Poliks. 2016. Computational Fluid Dynamics Modeling and Online Monitoring of Aerosol Jet Printing Process. *Journal of Manufacturing Science and Engineering* 139 (2): 021015. `https://doi.org/10.1115/1.4034591`.

[28] Cantù, Edoardo, Sarah Tonello, Giulia Abate, Daniela Uberti, Emilio Sardini, and Mauro Serpelloni. 2018. Aerosol Jet Printed 3D Electrochemical Sensors for Protein Detection. *Sensors* 18: 1–14. `https://doi.org/10.3390/s18113719`.

[29] Salary, Roozbeh (Ross), Jack P. Lombardi, M. Samie Tootooni, Ryan Donovan, Prahalad K. Rao, Peter Borgesen, and Mark D. Poliks. 2016. Computational Fluid Dynamics Modeling and Online Monitoring of Aerosol Jet Printing Process. *Journal of Manufacturing Science and Engineering* 139 (2): 021015. `https://doi.org/10.1115/1.4034591`.

[30] Feng, James Q. 2019. Mist Flow Visualization for Round Jets in Aerosol Jet ® Printing. *Aerosol Science and Technology* 53 (1): 45–52. `https://doi.org/10.1080/02786826.2018.1532566`.

[31] Seifert, Tobias, Enrico Sowade, Frank Roscher, Maik Wiemer, Thomas Gessner, and Reinhard R. Baumann. 2015. Additive Manufacturing Technologies Compared: Morphology of Deposits of Silver Ink Using Inkjet and Aerosol Jet Printing. *Industrial and Engineering Chemistry Research* 54 (2): 769–79. `https://doi.org/10.1021/ie503636c`.

[32] Pianigiani, Michele, Robert Kirchner, Enrico Sovernigo, Alessandro Pozzato, Massimo Tormen, and Helmut Schift. 2016. Effect of Nanoimprint on the Elastic Modulus of PMMA: Comparison between Standard and Ultrafast Thermal NIL. *Microelectronic Engineering* 155: 85–91. `https://doi.org/10.1016/j.mee.2016.03.019`.

[33] Spin Coating: A Guide to Theory and Techniques. Ossila enabling materials science. `https://www.ossila.com/pages/spin-coating`.

[34] Salkar, R. A., P. Jeevanandam, S. T. Aruna, Yuri Koltypin a A. Gedanken. The sonochemical preparation of amorphous silver nanoparticles. *Journal of Materials Chemistry* [online]. 9(6), 1333–1335 [cit. 2016-04-09]. DOI: 10.1039/a900568d. ISSN 09599428. Dostupné z: `http://xlink.rsc.org/?DOI=a900568d`

[35] Terai, Fujio, Shigeki Matunaka, Akihiko Tauchi, Chikako Ichimura, Takao Nagatomo, and Tetsuya Homma. 2006. Xenon Flash Lamp Annealing of Poly-Si Thin Films. *Journal of The Electrochemical Society* 153 (7): H147. `https://doi.org/10.1149/1.2200291`.

[36] Schroder, K. A., S. C. Mccool, and W. F. Furlan. 2006. Broadcast Photonic Curing of Metallic Nanoparticle Films Basic Process Research and Development System. *The Nanotechnology Conference and Trade Show* 3 (512): 198–201.

[37] Hummelgård, Magnus, Renyun Zhang, Hans Erik Nilsson, and Håkan Olin. 2011. Electrical Sintering of Silver Nanoparticle Ink Studied by In-Situ TEM Probing. *PLoS ONE* 6 (2). `https://doi.org/10.1371/journal.pone.0017209`.

[38] Schleunitz, Arne, Vitaliy A Guzenko, Martin Messerschmidt, Hakan Atasoy, Robert Kirchner, and Helmut Schift. 2014. Novel 3D Micro- and Nanofabrication Method Using Thermally Activated Selective Topography Equilibration (TASTE) of Polymers. *Nano Convergence* 1 (1): 1–8. `https://doi.org/10.1186/s40580-014-0007-5`.

[39] Dryzek, J., M.Wróbel, E. Dryzek. 2016, Recrystallization in severely deformed Ag, Au, and Fe studied by positron-annihilation and XRD methods. *Physica status solidi* 253 (10): 2031–2042. `https://doi.org/10.1002/pssb.201600280`.

[40] Horváth, Barbara. 2013, Influence of copper diffusion on the shape of whiskers grown on bright tin layers. *Microelectronics Reliability* 53: 1009–1020. `https://doi.org/10.1016/j.microrel.2013.03.008`.

Appendix

Fabrication of Large Area Sub-200 nm Conducting Electrode Arrays by Self-Confinement of Spincoated Metal Nanoparticle Inks

Barbara Horváth, Barbora Křivová, Sami Bolat, and Helmut Schift*

Here, the fabrication of sub-200 nm metal wires from commercial silver inks with 50 nm particle size, 100 times narrower than with typical low-resolution ink-jet and screen printing in flexible electronics, is demonstrated. Using a combination of spincoating on prepatterned polymer substrates and flash lamp annealing, nanoparticles merge to wires featuring good electrical conductivity. With this method less than 150 nm thin wires can be generated from 2 µm wide or smaller V-grooves due to adapted dilution of particle content, self-confinement in V-grooves, shrinkage of line width during solvent evaporation, and sintering. After nanoimprinting, grooves made from PMMA are smoothened out by thermal reflow without affecting the wires. The resistivity of 300 µm long, 400 nm wires is similar to more conventional ink-jet printed wires with 10–50 µm widths.

1. Introduction

There is a rapidly growing interest for low-cost fabrication methods to create large area, flexible electrodes. Metal nanowires can be used as transparent conductive electrodes in various fields, such as sensors, heaters, solar cells, light emitting diodes or touch panels. Additionally, they can be used for optical purposes, such as wire grid polarizers.[1] There are different patterning methods to place silver nanowires on surfaces, such as photolithography, electron lithography, or nanoimprint lithography (NIL).[2,3] These methods, however, involve the use of pattern transfer methods (physical vapor evaporation, etching or lift-off) to convert a resist pattern into metallic wires; or use direct printing (i.e., reverse NIL methods)[4–6] which requires stamps with nanometer size grooves and to coat a suitable thin polar liquid layer on the substrate which serves as a transfer mechanism; therefore they are still costly for high volume manufacturing of transparent electrodes in low-cost applications. Other options, such as randomly distributed metal nanofibers[7] or nanowire networks[8,9] allow no control of the location and pattern of the wires as they are always randomly distributed on the substrate. On a micrometer scale of creating silver wires, inkjet[10] and gravure printing[11,12] are low-cost additive methods used for printed electronics, yet with resolutions often in the range much larger than 10 µm.[13] They are not suitable for applications where sub-micrometer or even sub-100 nm resolutions (e.g., for subwavelength optics) are needed. In order to shrink dimensions without using traditional lithography, the patterning of nanoparticles by self-assembly on pre-patterned substrates is a solution. It has been tested for the generation of dense arrays of 50–80 nm silica particles in V-grooves.[14] Capillary assisted particle assembly (CAPA) is used for the parallel assembly of sub-micrometer particles into hexagonal arrangements by convective or capillary effects.[15,16] However, nanoparticle inks have polydisperse distribution of particle sizes (here between 20 and 80 nm) and therefore typically do not self-assemble but rather form a loose agglomeration, which is merged into a 3D cluster by post-processing (e.g., sintering).

The objective of the present paper is to provide a novel method for reducing the width of structures generated by ink deposition on pre-patterned substrates. We aim to achieve resolutions which are not only much smaller than the resolution of the applied additive process, but also smaller than the width of the pre-patterned structures. Pre-patterning the substrates with specific sub-micrometer topography can be done by straightforward replication techniques such as thermal or UV-assisted NIL which can then be covered either locally (e.g., by inkjet printing) or on an entire substrate (by spincoating). This enables the generation of fine structures in the micrometer range down to subwavelength range at low cost and high throughput, and thus satisfies the demand for a technology being less expensive than currently known lithographic processes. In the process proposed here, we use this approach to fill V-groove shaped substrates with silver nanoparticle-based inks, typically with average 50 nm particles dispersed in a suitable solvent.[17] The nature of the V-groove substrates with inclined sidewalls and Λ-ridges between adjacent grooves separates individual lines

Dr. B. Horváth, B. Křivová, Dr. H. Schift
Paul Scherrer Institute (PSI)
Laboratory for Micro- and Nanotechnology
5232 Villigen PSI, Switzerland
E-mail: helmut.schift@psi.ch
B. Křivová
Department of Experimental Physics
Palacký University Olomouc
77147 Olomouc, Czech Republic
S. Bolat
Swiss Federal Laboratories for Materials Science and Technology (EMPA)
Überlandstrasse 129, 8600 Dübendorf, Switzerland

The ORCID identification number(s) for the author(s) of this article can be found under https://doi.org/10.1002/admt.201800652.

**ADVANCED
SCIENCE NEWS**
www.advancedsciencenews.com

**ADVANCED
MATERIALS
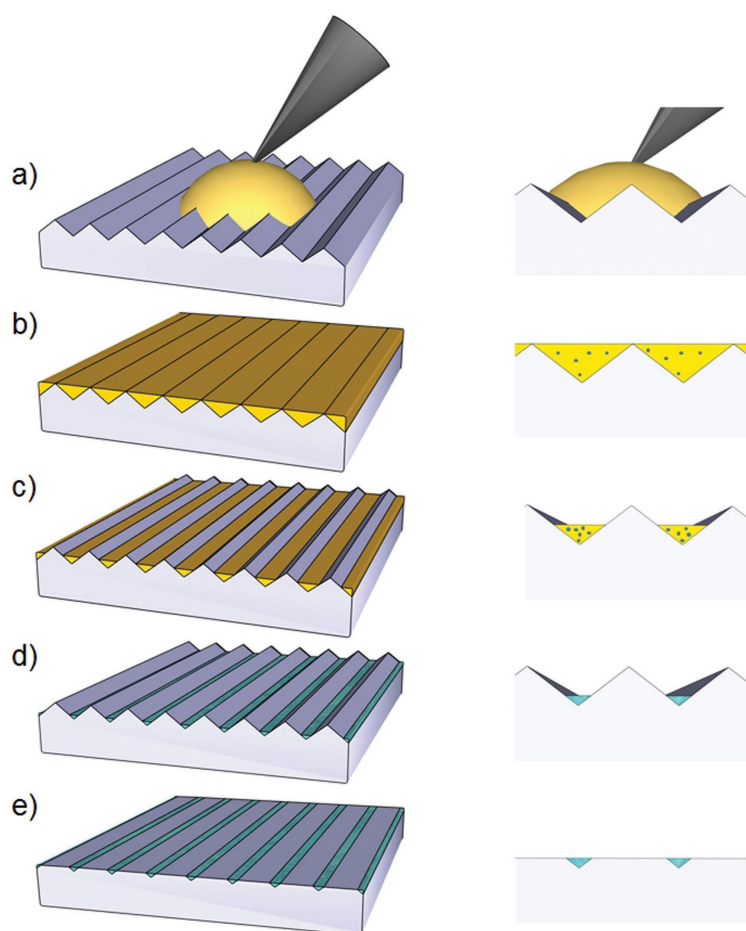TECHNOLOGIES**
www.advmattechnol.de

Figure 1. Schematics of process to generate a self-forming metal line pattern—left side: general view, right side: magnification of the cross section. a) Dispensing of silver ink solution on V-grooves, b) spincoating and the beginning of solvent evaporation, c) volumetric shrinkage due to drying, d) densification and nanoparticle merging, e) simultaneous sintering of silver wires and thermal reflow of the substrate.

surface between the lines.[19,20] Flash lamp annealing (FLA) is presented as an option for both ink sintering and thermal reflow, which enables to reduce both the temperature and exposure time.[21,22] With the optimization of inks and solvents, a wire width below 150 nm is feasible, which would qualify this method for low-cost fabrication of wire grid polarizers for visible wavelengths and would address the needs of high-resolution flexible electronics, or consumer goods such as foils for light redirecting, displays, solar panels, and packaging.

2. Results and Discussion

2.1. Self-Assembling of Silver Nanoparticles in Lines with Defined Width

Electrically conductive nanowires were produced by using substrates pre-patterned with V-grooves. The surface topology enables the wire width reduction compared to the width of the V-grooves due to confinement of the nanoparticles upon evaporation of the ink solvent. This method allows the generation of fine structures even near the sub-100 nm range depending on the particle load of the initial solution. As seen in **Figure 1**a, the filling of grooves is carried out by spincoating diluted ink solution on an entirely patterned PMMA surface, which then covers all the grooves. The rotation during spincoating removes excess material from above the grooves and the edges act as separation of the individual ink lines (Figure 1b). The concentration of nanoparticles is anticipated to be the same in the entire liquid film, which deposits within the rims of the V-grooves. The V-shaped grooves have smooth sidewalls with a constant angle meeting at a line-like bottom, and the contact angles of the solution inside the ridges allow a filling of the groove with concave meniscus and entirely dewet the ridges free of ink. During solvent evaporation (Figure 1c) the nanoparticles accumulate in the lowest central part of the V-groove, and in best case without any nanoparticles contaminating the dewetted surface. Diluting the inks further reduces the number of particles in each V-groove before the solvent is evaporated. Upon complete evaporation of the solvent, the nanoparticles entirely collect at the bottom of the grooves (Figure 1d). If we assume a completely filled V-groove with 4 µm width (in an ideal V-groove grating with 4 µm period and without a plateau in between), a ratio of 1:100 volume content of solid to solvent would result in 400 nm wide triangle cross-sectioned lines after drying and sintering (if we assume a complete sintering eliminating all voids). Yet, in reality the grooves are not completely and evenly filled. Therefore, thinner sub-200 nm lines can only be achieved by using much higher dilution

and during the evaporation of the solvent the solid material accumulates from the dispersion at the bottom of the groove. The nanoparticles merge into a densely packed agglomerated line after drying; a sintering step removes the organic additives and eventually forms a metal wire with conductivity similar to bulk metal. Since we aim to fabricate line widths close to the initial nanoparticle size, a suitable process has to be chosen where diffusion induced particle growth is reduced. Furthermore, temperatures have to be kept below 200 °C in order to comply with the polymer substrates used for low-cost printed electronics. Such polymer substrates are poly(ethylene)terephthalate (PET) and polyethylene naphthalate (PEN),[18] which would melt in too high temperatures and the structures on them would be distorted. By using poly(methyl methacrylate) (PMMA) with lower T_g as a substrate (or as a planarization layer on other material substrates), we can apply a heating step to eliminate the sharp Λ-ridges and grooves, and achieve a flat

**ADVANCED
SCIENCE NEWS**
www.advancedsciencenews.com

**ADVANCED
MATERIALS
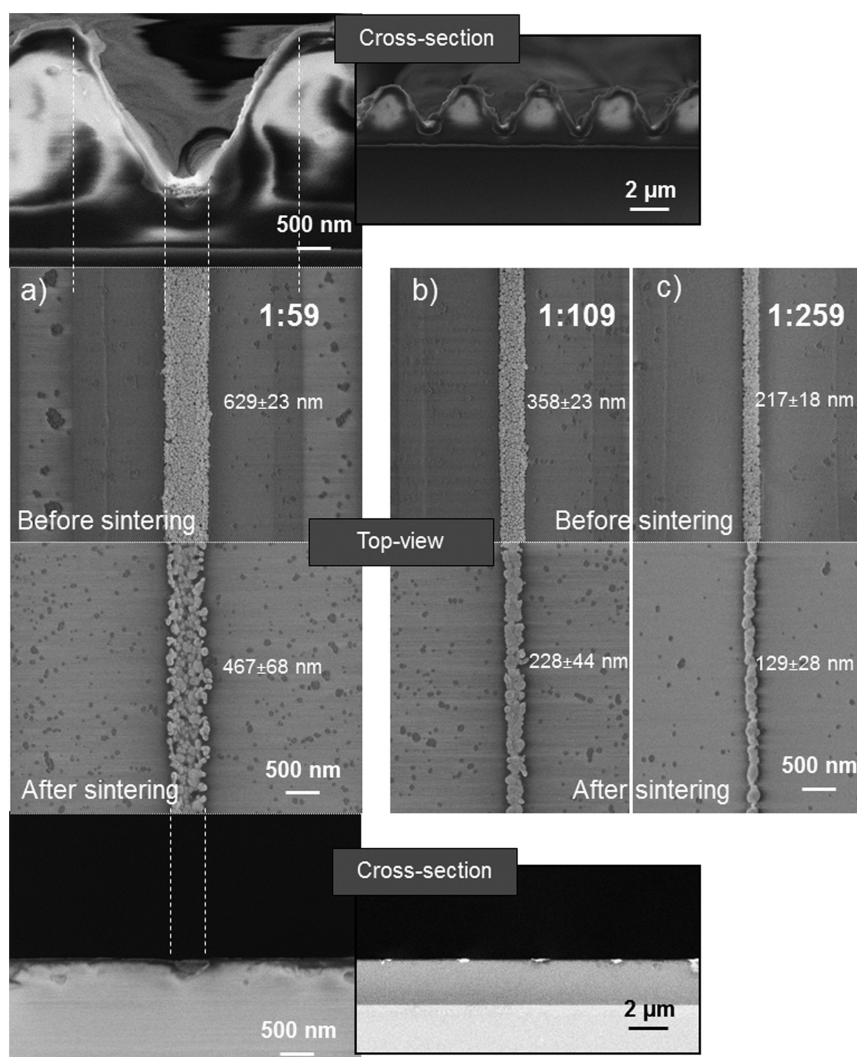TECHNOLOGIES**
www.advmattechnol.de

Figure 2. SEM microscopy images displaying the wire widths depending on the volume fraction of metal particles in solvent. Transformation of assembled particles before and after sintering: a) the top view and the corresponding cross sections with different magnifications of the wires made with Genes'Ink silver inks in a ratio of 1:59, where a change of topography is seen due to thermal reflow. Top view of wires diluted with IPA in ratios of b) 1:109 and c) 1:259. The wires are all triangle shaped (only visible in close-ups of perfectly cleaved polymer layers and wires with low LER) due to the sharp vertex of the V-groove, the simultaneous reflow and sintering alters it into a slightly smaller inclination.

or smaller V-grooves. With the 1:59 thinning (one volume unit of silver ink thinned with 59 unit isopropyl alcohol (IPA)) we achieve ≈500 nm lines in 3.2 µm wide grooves, 230 nm with 1:109 and 120 nm with 1:259 thinning (**Figure 2**a–c). In the case of samples where an 800 nm plateau is present, few nanoparticles may remain on the surface as residue. During the volume reduction and concentration, it is important that the evaporating ink does not deposit nanoparticles on the dewetted surfaces while the contact line is moving. In order to make the best quality line with the least nanoparticle residue outside of the lines, the selection of the right solvent matching the substrate is highly important. Silver inks using ethanol and ethylene glycol as base can be successfully further diluted with

IPA. The contact angle of the undiluted ink is 14.8° and of IPA is close to 0° on PMMA; therefore we can state that a dilution of 1:59 already has very good wetting properties with contact angles close to 0°. Additionally, IPA is a gentle solvent that does not dissolve polymers such as PMMA and PC or attacks them chemically. The spincoating process is then followed by heat treatment, which eventually merges the nanoparticles and sinters them together to solid wires (Figure 1e). The ideal case would be to use inks with sub-10 nm particle sizes and to use sintering methods that enable the merging of particles into a homogeneous film with low line edge roughness (LER) and reproducibility over long lengths along with well-connected particles. Here, since a dispersion of various nanoparticle sizes

ADVANCED
SCIENCE NEWS
www.advancedsciencenews.com

ADVANCED
MATERIALS
TECHNOLOGIES
www.advmattechnol.de

with an average of 50 nm was used, a 50 nm line width is expected as the absolute minimum but more realistically in the range above 100 nm.

2.2. Sintering Self-Assembled Silver Nanoparticles into Wires and Thermal Reflow of Substrate

Sintering is a process in which nanoparticles merge together by applying heat below their melting point. Adjacent particles partially coalesce owing to diffusion and consequently the total surface area decreases. For large >10 µm wide wires, grains in each groove of ≈200 nm do not play a big role on the roughness. However, in case of nanowires, it contributes to a non-negligible LER, which is limiting the minimum feature sizes. Photonic sintering (or photonic curing, synonymous to FLA) is a low thermal exposure sintering method developed to sinter nanoparticle thin films for printed electronics, e.g., on polymeric substrates. The process involves using a xenon flash lamp to deliver a high intensity, short duration (<10 ms) pulse of light to the deposited nanoparticles. In order to acquire high electrical conductivity in the sintered silver nanoparticles, several FLA parameters such as light energy and pulsed light patterns were investigated previously.[23,24]

In the research presented here, a relatively low sintering temperature of 150 °C was used for the silver ink. This temperature is ideal for the sintering of silver nanoparticles according to the ink datasheets, although longer duration can have a negative effect on the LER. Additionally as an alternative, FLA was used to inhibit nanoparticle size growth due to diffusion, since extended exposure to conventional heat treatment would allow both the merging of particles and grain growth. FLA enhances sintering while keeping the grain growth limited. This enables to keep the grain sizes as near as possible to the initial particle size. We therefore use the expression grain for the merged nanoparticles.

Since the final metal structure is on the bottom of the grooves which would make the addition of further layers difficult in case of a more complex process line, it is advantageous to remove the V-groove topography and flatten the surface after the wires have been fabricated. Thermal reflow is a suitable process for this, which smoothens out the polymer surface due to energy minimization. The underlying PMMA substrate softens during the curing of the ink at 150 °C and transforms its surface shape causing the ridges to sink and the V-grooves to become rounded. Thanks to this effect, the V-grooves can be eliminated in regions where there is no coverage with nanoparticles, and a thin silver wire forms in a small groove surrounded by a flattened-out surface. Such process can be individually tuned by modifying the T_g of the polymeric material, enabling to soften the material locally to avoid further deformation and sinking of the lines into the substrate.[25]

We have to distinguish the reduction of line widths due to self-confinement into the V-grooves or due to the sintering nanoparticles into grains. Dilution ratios, solvents and particle loads play a role for self-confinement by taking into account contact angles and coagulation; for sintering densification, grain growth and material diffusion have to be taken into account. The aim is to get electrically conductive wires with a minimum line width, low LER, low number of defects, and

high conductivity. For electrical wiring applications it is important to obtain wires that are not broken, neither are shortcuts between neighboring wires allowed. In other applications such as for wire grid polarizers, interrupted wires may be allowed. In all cases, the control of line width and LER is necessary, and defects such as shortcuts between adjacent wires or interruption of single wires have to be minimized or eliminated.

2.2.1. Thermal Sintering (150 °C) of Wires

The higher the solvent/nanoparticles ratio of the solution is in each groove, the more the forming wires will reduce in width. Theoretically the smallest line width would be a row of single connected particles, with the width of the largest particle size. Densely packed nanoparticles need sufficient contact, and the thin organic layer on the surface of the nanoparticles (to avoid coalescence in solution) needs to be removed by the heat treatment. For wires composed of few or even single particles, an elongation or minimal particle growth is needed. Although due to volume conservation, the latter can only be at the expense of other particles, which have to diffuse into other particles. Figure 2 shows how line width decreases with increasing the dilution of the solution with IPA. With the thermal reflow, however, the resolutions achieved are mostly limited by the grain growth of the silver particles. The initial average size of the nanoparticles before sintering was 49 ± 15 nm. This was calculated by measuring the longest diameter of 122 elliptical nanoparticles of the commercial ink used in this research. The smallest measured nanoparticle was 20 nm, and the largest was 86 nm. The size distribution of the nanoparticles can be seen in **Figure 3**b. During sintering at 150 °C for 30 min, nanoparticles diffuse into each other and thus grain growth occurs. In case of the 1:59 dilution, the average grain size is 121 ± 33 nm, with a maximum size of 290 nm. Size distribution measured on a set of 116 grains also shows a large variety of sizes occurring in the range of 100–200 nm diameters. With such intense grain growth it is not possible to go below a wire width of 150 nm because of the large grain sizes and additionally the diffusion of silver atoms into certain grains creates a deficit of silver atoms in other areas and thus breaks occur in the line (Figure 2c). On the other hand, the LER of 1:259 is much lower compared to 1:59 because its line width consists of only one grain, while 1:59 consists of multiple grains. The cross sections of 1:59 wires show that the PMMA substrate has a V-groove structure before sintering with the nanoparticles sunk to the bottom, and these structures are completely flattened out after sintering. The sintered grains still keep a V-shape after sintering, however it is slightly flattened: the average angle from the surface is reduced from 54.7° (the <111> angle of the Si stamp to the surface) to 36°±4° (based on a measurement of 25 cross sections). The shape of the cross section was a near perfect triangle in cases where the cross section was made in an area with lower LER of the wire. In parts where higher LER was observed, the triangle was wider and had a slight (up to 50 nm) shrinkage in its surface area due to the material transport toward the rough side grains by diffusion.

Adequate sintering is necessary to obtain good electrical conductivity in the wires.[26] Initially before reaching lower curing
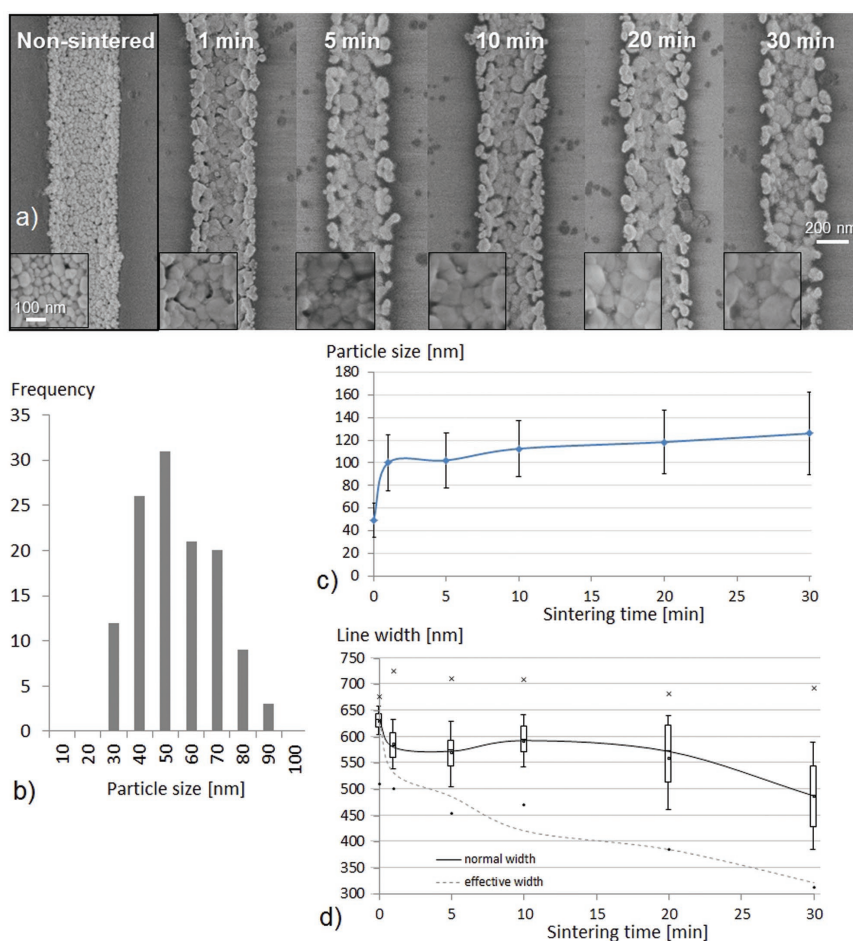
**ADVANCED
SCIENCE NEWS**
www.advancedsciencenews.com

**ADVANCED
MATERIALS
TECHNOLOGIES**
www.advmattechnol.de

Figure 3. a) SEM microscopy images of grain size changes of Ag:IPA dilution of 1:59 in case of before sintering and after 150 °C sintering for 1, 5, 10, 20, and 30 min. Inset: the grain structure at the middle of the wire; b) size distribution of the nanoparticles before sintering; c) average particle size depending on sintering durations at 150 °C; d) line width and roughness of Ag:IPA dilution of 1:59 depending on sintering time. Box plot method for line width evaluation is described in the Experimental Section.

temperatures, an organic material is surrounding the silver nanoparticles. This few nanometers thin organic layer serves a purpose to stabilize the nanoparticles and to avoid coalescence in the solution. However, after nanoparticle deposition on the substrate, this organic layer prevents electrons moving from one nanoparticle to another, and therefore the unsintered ink has lower conductivity properties[27] in the range of 10^{-4} Ω cm according to our measurements. Decomposing this organic layer by heating allows the silver nanoparticles to touch. At a lower curing temperature than the 150 °C proposed by the ink supplier that is determined by the organic additives, the ink should already start showing good conductive properties. Good conductivity therefore can only be achieved at higher temperatures: the tiny contact areas between two nanoparticles transform into a larger area by necking. The loosely assembled particles densify into closer packs and transform into a metallic crystal structure with a low number of grain boundaries. The initial driving force to this is either Ostwald ripening, where the

large surface-to-volume ratio of the particles allows the surface energy to reduce, thus larger particles develop by the merging of smaller ones[27] or by coalescence followed by aggregation.[28] Bulk diffusion becomes the major driving force for further grain growth. Silver has relatively low recrystallization temperature, Dryzek et al. found that recrystallization starts already from 60 °C,[29] and grain growth due to bulk diffusion is accelerated at higher (100–150 °C) temperatures. Grain boundary movement occurs when atoms go through the grain boundary to another grain to lower the grain boundary free energies.[30]

The longer the annealing time, the larger the grains grow in the wire. Figure 3a shows spincoated wires with Ag:IPA dilution of 1:59 before and after sintering at 150 °C for 1, 5, 10, 20, and 30 min. It can be seen in the insets of Figure 3a, that necking of particles occurs even after 1 min, and is almost completed after 20 min, as the amount of voids between 3 grains is minimal. Figure 3c shows the rate of grain growth according to sintering time with the corresponding grain size distribution.

**ADVANCED
SCIENCE NEWS**
www.advancedsciencenews.com

**ADVANCED
MATERIALS
TECHNOLOGIES**
www.advmattechnol.de

While initially the average nanoparticle size is around 50 nm in an unsintered line, the average grain size grows to around 125 nm in a well-sintered wire (for 30 min). The largest grain sizes measured during sintering for 0, 1, 5, 10, 20, and 30 min were 86, 164, 178, 183, 192, and 290 nm, respectively.

The average grain size in a wire correlates with the LER. Since there can be differences in the line width after spincoating depending on the ambient conditions (e.g., humidity) due to their slight effect on the angle of the meniscus, a single sample was spincoated and then broken into six pieces, and afterward these pieces were heated for different time durations. The box plots in Figure 3d show line width and roughness over sintering time, which shows that longer sintering time leads to shrinkage of the line widths along with higher roughness. Many voids are observed between the grains in early sintering stages, but as the necking of grains advances, these voids shrink and the volume of the wires reduces. From around 20 min, diffusion is the major reason for grain growth on the expense of other grains. The grains in the edge of the wire have less resource of silver atoms due to the lack of neighboring grains, hence the wire width still continues to reduce and the LER to increase more forward in time. Line roughness becomes more significant over time, initially the roughness of the lines is within a range of 25.4 nm considering the difference between the Q3 and Q1 quartile to the median; however the LER directly jumps to 45.7 nm after 1 min of sintering and reaches 115.3 nm after 30 min (the explanation of the Q1–Q3

quartile calculations can be found in the Experimental Section in details). For different purposes we calculate line width in two ways: for roughness calculations the normal line width is considered; for electrical applications (i.e., to calculate the average cross section area) the effective width is considered. The two calculation methods are also described in Experimental Section. The effective line widths of the 1, 5, 10, 20, and 30 min sintered lines are 532, 487, 468, 429, and 389 nm, respectively.

2.2.2. Flash Lamp Annealing of Wires

An alternative method to achieve shorter sintering time is using FLA to sinter the spincoated lines. **Figure 4**a shows the dependence of voltage on the sintering quality when the flash annealing time is kept constant at 500 µs. It can be seen that until 650 V (energy density 4.7 J cm^{-2}), the absorbed irradiation is not sufficient for sintering, the nanoparticles stay intact and no particle growth is observed. Sintering starts after a breakthrough voltage of 700 V and energy density of 5.8 J cm^{-2}, where necking of nanoparticles is already observed (Figure 4b). As the energy increases, so does the contact area between two nanoparticles due to diffusion, although grain growth is not explicit in case of FLA compared to conventional thermal sintering in 150 °C. The ultrashort annealing time of 500 µs prohibits most of the bulk diffusion to occur and it minimizes after the rapid cooling of the sample. Line width shrinkage is in
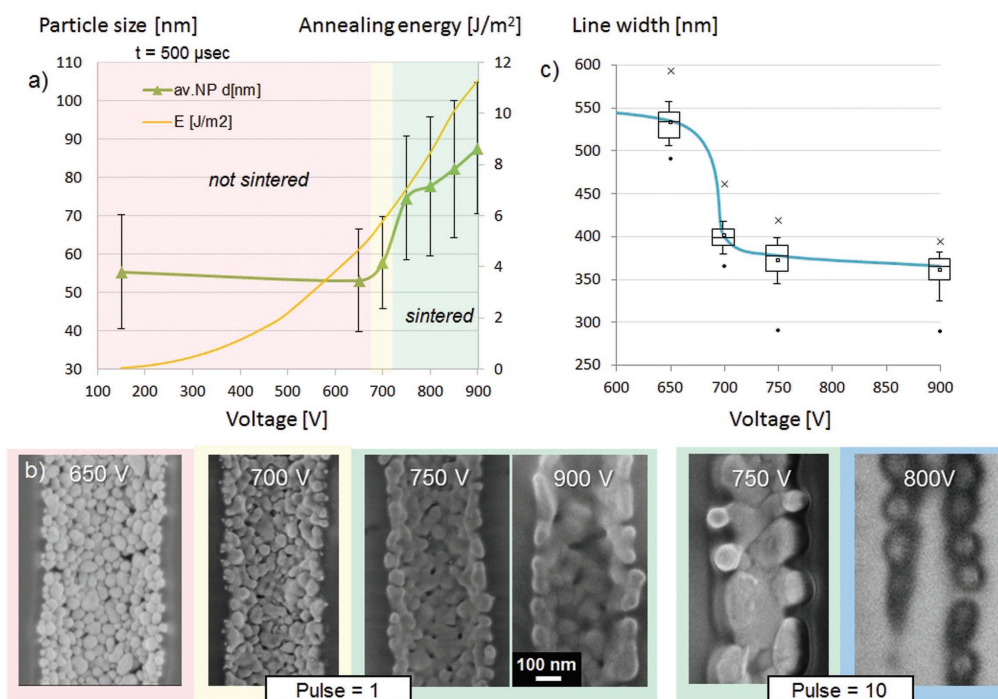

Figure 4. a) Average particle size depending on the flash annealing voltage, with the corresponding annealing energy; b) SEM microscopy images of sintered lines depending on the annealing voltage and number of light pulses; c) line widths depending on the annealing voltage, while $t = 500$ µs (Ag:IPA dilution of 1:59).
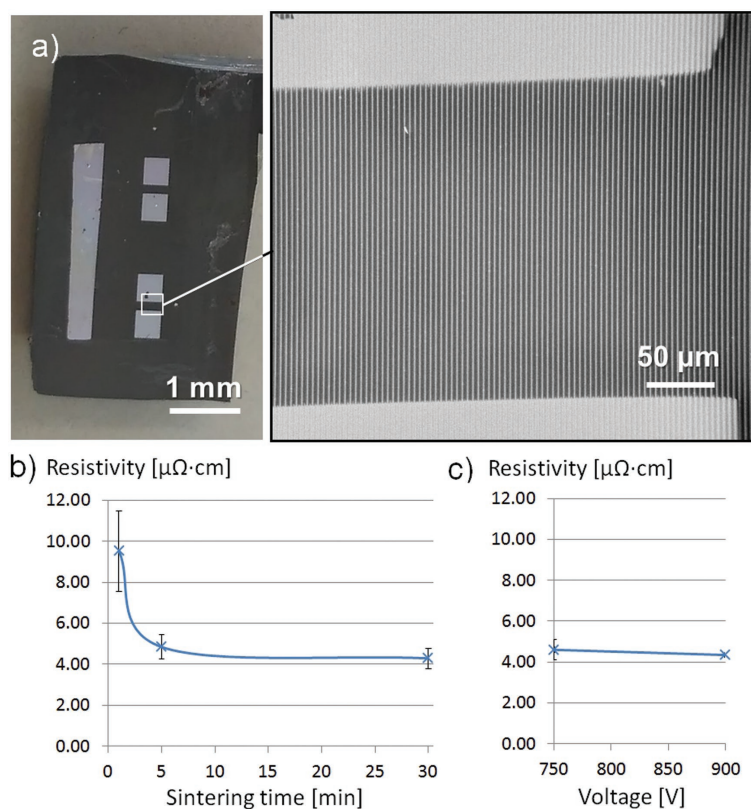
**ADVANCED
SCIENCE NEWS**
www.advancedsciencenews.com

**ADVANCED
MATERIALS
TECHNOLOGIES**
www.advmattechnol.de

2.3. Measurement of Electrical Resistivity of the Sintered Silver Wires

The electrical conductivity measurements of the metal wires demonstrate a successful sintering. Since the process relies on nanoparticle assembly and particle merging during sintering, various defects may occur with widths near the limit of particle size which have adverse effects on specific applications. Thinner wires (e.g., the 1:259 dilution with 129 nm width) experience breaks frequently due to the loss of silver atoms during grain diffusion. The average wire length achieved was around 20 µm. Therefore, we have selected slightly thicker lines around 400–500 nm for the electrical characterization of the wires developed by different sintering methods, created by 1:59 IPA dilution. With these wider lines we can more reliably measure the electrical resistivity of the sintered silver. Additionally, breaking of the lines was seldom observed. The average cross section area of these wires was determined by the effective width of each sintering type and condition, which values can be found in Figure 3d. **Figure 5**a shows an example of a sample with multiple parallel wires on its surface. 100 nm thick silver pads were evaporated on the wires with 200–400 µm distances between two pads. As explained in the Experimental section more in details, the resistivity of the wires were measured by placing probes on the two pads.

The electric measurements give a clear indication that full conductivity can be achieved both with conventional sintering at 150 °C and FLA. Figure 5b shows the resistivity values of 1:59 silver wires after sintered for different time lengths. The effective width is taken into account during the cross section calculation, therefore the effect of higher LER has is in smaller cross section areas. Most changes in the resistivity values are due to the different stages of nanoparticle sintering: namely the removal of organic layer on the nanoparticle, necking between nanoparticles and grain growth. Resistivity was calculated with Equation (1)

$$\rho = \frac{R \times n \times w_{\text{eff}}^2 \times \tan \alpha}{4\,L} \tag{1}$$

where R is the resistance of the wire grid between the two pads, n is the number of wires (and their multiplication results in the average resistance of a single wire); w_{eff} is the effective width, α is the angle of the cross-section triangle at the surface (together these values give the cross-section area); and L is the wire length between the two pads.

Initially, the unsintered ink has low conductivity properties in the range of 10^{-4} Ω cm according to our measurements. 1 min annealing already provides reasonable sintering with

Figure 5. a) Setup of the resistance measurement, with evaporated silver pads on the wires with 200–400 µm distances. The photo shows the chips where line arrays are located between large contact pads. The inset shows an SEM image of an array of 225 µm long wires. The resistivity of wires made with Ag:IPA dilution of 1:59 after different sintering conditions such as b) thermal sintering and c) FLA.

the similar range for FLA samples compared to sintering for 30 min in 150 °C (Figure 4c). There is an initial drop in the width when the organic coating surrounding the nanoparticles evaporates and the nanoparticles slightly rearrange during necking. On the other hand, the advantage of this technique is that the roughness does not grow significantly after sintering. The roughnesses of the lines are 31 and 25 nm for 750 and 900 V, respectively, considering the difference between the Q3 and Q1 quartile to the median. It is visible by scanning electron microscope (SEM) that the middle of the line is located slightly deeper than before. In higher energies the PMMA substrate also starts to flatten and this movement of the substrate slightly folds the edge of the line toward the middle axis of the line, hence a V-shaped cross section with a slightly U shaped top is formed. The nanoparticles, however, do not merge into spherical large grains within the lines in which large grains would assume the lowest surface to bulk ratio, hence further line shrinkage is not anymore significant. When too much energy is subjected to the wires (shown as pulse = 10 with lower 750 and 800 V), grain growth is heavily accelerated leading to >200 nm grains, the PMMA substrate melts and the silver wires sink under the surface.

**ADVANCED
SCIENCE NEWS** ⎯⎯⎯⎯⎯⎯⎯⎯⎯⎯⎯⎯⎯⎯⎯
www.advancedsciencenews.com

**ADVANCED
MATERIALS**
TECHNOLOGIES
www.advmattechnol.de

Table 1. Comparison of wire properties (average and maximum nanoparticle size, LER, resistivity) made with Ag:IPA dilution of 1:59 for different sintering types and process parameters.

Sintering process		Nanoparticle size		Line edge roughness	Resistivity
		Average [nm]	Maximum [nm]	(Q3–Q1) [nm]	[Ω cm]
No sintering		49.1	86.0	25.4	high (10^{-4} range)
	1 min	100.0	164.6	45.7	9.52×10^{-6}
Thermal (150 °C)	5 min	102.2	178.3	49.5	4.84×10^{-6}
	10 min	112.5	182.6	48.8	
	20 min	118.4	191.6	108.6	
	30 min	126.0	290.2	115.4	4.29×10^{-6}
FLA (500 µs)	750 V	74.6	102.3	30.7	4.59×10^{-6}
	900 V	87.6	119.6	24.9	4.34×10^{-6}

a slightly higher resistivity of 9.52×10^{-6} Ω cm. While at this sintering time high grain growth and decreasing line width can already be observed, the effective line width is still slightly higher due to its lower LER compared to later sintering times, which results in larger cross section area. The organic material on the surface of the grains has already disappeared, but the grains within the wire are connected to each other only with a lower area neck. 5 and 30 min sintering times provide good resistivity with values of 4.84 and 4.29×10^{-6} Ω cm, respectively. These values are in correlation with Genes'Ink data sheet claiming a sheet resistance of <1.7 mΩ sq^{-1}/25 µm (meaning resistivity of 4.25×10^{-6} Ω cm or lower) after 3 min of sintering at 150 °C. Some voids are still observed between the grains after 5 min of sintering, however, it is minimized after 30 min, hence the further improvement of resistivity over long time. The resistivity of the FLA sintered wires is in a similar range with values of 4.59 and 4.34×10^{-6} Ω cm in case of 750 V and 900 V, respectively, as seen in Figure 5c. In these cases, similarly to the thermal sintering from 5 min, the necking is close to complete at 750 V. The slight improvement of resistivity seen at 900 V can be attributed to the even less amount of voids and also the increased grain size.

Table 1 shows the comparison of each sintering type and condition regarding their properties. For conventional thermal sintering, the longer the annealing time, the larger the nanoparticles grow. In a well-sintered wire (for 30 min) the average nanoparticle size can reach easily over 200 nm. Therefore, only short sintering times should be employed for sub-micrometer wires. Heating to 150 °C even only for 1 min leads to strong nanoparticle growth. This leads to high LER, and even to huge undercuts in the line edge, especially from 20 min of sintering. Additionally, low sintering time lengths are harder to control, as the heating and cooling speeds are much slower than the speed during the actual 150 °C sintering. In contrast to this, during FLA the nanoparticle growth is limited (while the necking is close to complete) and average nanoparticle size can be kept under 100 nm, thus keeping the LER comparable with values before sintering. Electrical measurements reveal the low resistivity of the wires from 5 min of sintering at 150 °C, and also for 500 µs FLA from 750 V.

For some applications with long individual wires (such as wire arrays), interruptions of single wires may only reduce the effectivity, e.g., in case of a sensing or heating device. In contrast to this, in interdigitated electrode arrays, single shortcuts between two electrodes may lead to the failure of the entire device. Single nanoparticle residues, which have not assembled at the bottom of the groove, may be of no influence as long as they do not interfere with the wires or the further process steps. While wire interruption and shortcuts are typical defects for electronic devices, for optical gratings a defined line width and low LER may be of higher importance than avoiding interruptions and contacts between lines. The V-grooves have to be free from kinks and contamination, since the agglomeration at the bottom has to happen unhindered. Different V-groove sizes and shapes may be used to control the wire size along a long groove, and to control the period of the wires. For wire grid polarizers, V-grooves with only a period of twice the size of the intended line width need to be used, while for transparent electrodes a high ratio between transparent and silver coated areas would be needed.

With this method more complex shapes with angles can also be made, which makes it useful for applications such as wirings for printed electronics. **Figure 6** shows examples by spincoating on 90° and 150° corners. The V-grooves made by anisotropic etching of silicon has the advantage that circuits with sub-micrometer wide grooves can be designed on large, wafer sized areas. The shape of the V-grooves is given by the 54.74° inclined crystalline <111> planes of a <100> wafer which enables to generate smooth, defined grooves in a lithographic process following by anisotropic etching. While this favors orthogonal structures due to the crystalline orientation, other angles can be obtained as well, but with different sidewall angles and widths. With such method, at the meeting point of two crystallographic planes, the corner always has a distinguished edge. During spincoating the nanoparticles behave similarly on these edges as on the bottom of the V-groove: there is a tendency to deposit in the edges (see arrows in Figure 6a,b). However the higher the angle of the edge is, and thus the smoother the transition, the shorter is the agglomerated "tail," therefore, by avoiding 90° edges during the design of the circuits, this effect can be minimized. Additionally, since the different crystalline planes have different etching rates, V-grooves widths and depths need to
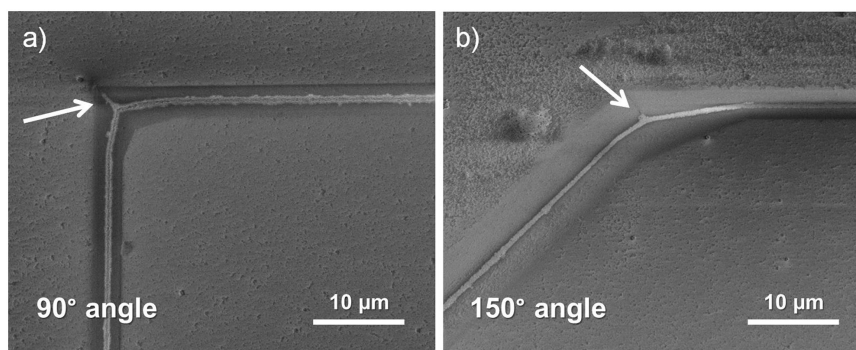
**ADVANCED
SCIENCE NEWS**
www.advancedsciencenews.com

**ADVANCED
MATERIALS
TECHNOLOGIES**
www.advmattechnol.de

Figure 6. SEM microscopy images of assembled Ag nanoparticles in V-grooves after spincoating with a) 90° and b) 150° angle corners. Image is made on unsintered samples; therefore, the V-groove structure around the wire is also visible. Arrows show the corner edge in the V-groove, which allows an additional tail to deposit.

be well controlled and aligned. Angles in between 30° and 45° degree orientations have stronger etching rates than the 0° and 90°, therefore the developed V-grooves are wider (as can be seen on Figure 6b).

Other V-groove developing methods can be considered in order to avoid the previously mentioned problems, V-grooves can also be manufactured with 3D lithography, such as direct laser writing or other grayscale lithography.[19] However, such methods are often restricted in throughput and thus area, and often do not provide the sharp edges and sidewall smoothness needed to enable the width reduction. These issues could be overcome with selective thermal reflow, where it was shown that various sidewall angles can be obtained in a single substrate.[25] It has to be noted that all these methods will become fully effective if molds are created with the 3D topographies from which polymer films can be imprinted in a straightforward, cost-efficient way.

3. Conclusion

Patterning silver nanoparticle inks down to sub-micrometer and even sub-200 nm opens the way for a range of low-cost processes where only high end lithography was used until now. By filling the grooves of pre-patterned substrates using a volume-confining additive coating process such as spincoating, and by reducing the line sizes according to topographic effects, it is possible to apply sintered metallic nanowires on large area consumer products. If surfaces of polymeric devices and foils are made by low-cost high volume processes (e.g., thermal injection molding or roll-to-roll nanoimprint) and combined with additive processes with locally defined volumes such as inkjet, entire but also confined areas of flat and even uneven surfaces could be covered with metallic gratings, meshes or possibly dot patterns. The fact that a commercial ink with a nondisclosed composition and large particle distribution could be used to make millimeter-long wires with homogeneous width shows the capability of the method. The combination with FLA may be the solution for limiting particle growth which minimizes sintering time and thus time for grain growth, and may even be used for inks with small

monodisperse particle sizes of ≈10 nm to enable resolution much smaller than the 120 nm achieved so far.

4. Experimental Section

Substrates with V-grooves used as stamps for nanoimprint were obtained by anisotropic etching of <100> silicon substrates in a potassium hydroxide (KOH)-based etchant. Initially, a 100 nm Si_3N_4 film was applied by low pressure chemical vapor deposition (LPCVD) on silicon wafers. A negative resist (AZ nLOF 2020, MicroChemicals) was spincoated on the wafers and prebaked at 110 °C for 90 s. Patterning was done by contact photolithography (wavelength 365 nm) with a mask with 2 μm wide 4 μm period lines in a SÜSS MA6 mask aligner, which was then postbaked at 110 °C for 120 s. The Si_3N_4 was etched by reactive ion etching (RIE) in a mixture of O_2 5 ccm, and CHF_3 40 ccm, at a 100 nm min⁻¹ etching rate and the residual resist removed by wet development. KOH etching was applied on the exposed silicon at 80 °C for 18 min, and the Si_3N_4 masking layer was then removed by RIE. With this method, 3.2 μm wide and 2.3 μm deep V-groove lines with an angle of 54.74° between the <100> and the <111> plane were formed, with a small plateau of 200 nm between two grooves. Replication has been done of these silicon originals by UV-assisted imprint, and the V-grooves were converted into Λ-ridges. For the final replication, the stamps with Λ-ridges were imprinted into a 2 μm thick poly(methyl methacrylate) (PMMA) layer (nominal molecular weight 120 kg mol⁻¹, $T_g = 128$ °C) which was previously spincoated on a 100 mm silicon wafer. Imprint for 10 min was performed at 180 °C and 10 kPa, demolding at 60 °C. Silver ink of Smart'Ink S-CS31506 (recommended for flexography) from Genes'Ink was used that contained silver nanoparticles with a specified nanoparticle loading of 55 ± 5% in a carrier vehicle (solvent) of alcohol and glycol, and was further thinned down with isopropyl alcohol (IPA). Taking into account that silver is about 10 times denser than the typical solvents (10.49 g cm⁻³ for silver with respect to 0.79 g cm⁻³ for ethanol, 1.11 g cm⁻³ for ethylene glycol) a 50% weight content would result in a ≈10% volume content. The diluted high viscosity ink results in a much lower volume content, e.g., of about 1:590 for the 1:59 ratio dilution, as used here in the experiments. These solutions were then spincoated on the silicon samples with a patterned PMMA layer for 120 s at 5000 rpm. Sintering of the created samples was done either on a hotplate with the following heating profile: 3 min heating up to 95 °C, standby for 2 min at 95 °C (for solvent evaporation), then heat up to 150 °C in 5 min; keeping at 150 °C for 1–30 min (for sintering), then slow cooling (≈2 h) back to room temperature. Other samples were annealed by a flash light photonic curing system (PulseForge 1300 with peak radiant power of 24 kW cm⁻²). The annealed samples were observed with a Zeiss Supra
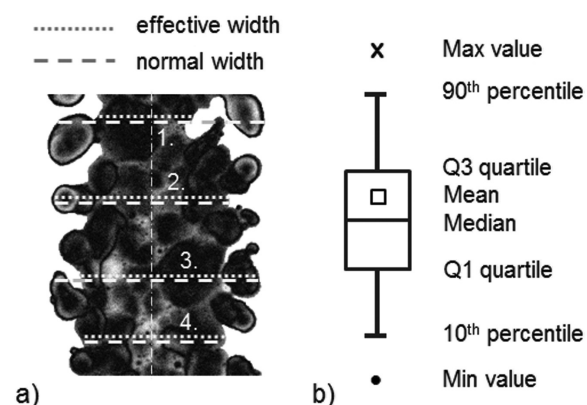
**ADVANCED
SCIENCE NEWS**
www.advancedsciencenews.com

**ADVANCED
MATERIALS
TECHNOLOGIES**
www.advmattechnol.de

Figure 7. a) Different measuring methods for measuring normal width and effective width (for electrical purposes); b) box plot method applied in this study for determining LER from measuring the line width at defined distances along the wire.

VP55 SEM at an acceleration voltage of 0.5–1.0 kV. The cross-sections of samples were made by conventional cleaving of silicon wafers after cooling the samples down in liquid N_2 in order to enhance the brittleness of PMMA and minimize deformity.

To determine the variation of the line width particularly of lines with granular edges, the box plot method was used to visualize statistical results of the LER.[31] The line widths were measured at every 50 nm throughout a line length of 4 µm, therefore all statistical results were determined by 80 measurement points. Due to the rugged granular boundary of the wire with large undercuts, the edge of the wire can cross a horizontal measuring line multiple times. **Figure 7**a shows such examples of calculation. At Case 1 and Case 3, the values of the normal and effective width are different. The edge of the wire crosses the horizontal measuring line multiple times (at Case 1 on both sides, at Case 3 on one side of the wire). In our measurements two different calculations are used at every width line: A. normal width where the furthest crossing points are considered compared to the middle of the line, and B. effective width where the closest crossing points are considered. At Case 2 and Case 4, the values of the normal and effective width are identical as the edge is crossing the horizontal measuring line only once. The box plot method is shown in Figure 6b. Box plots display the variation of the measured LER statistical data (Figure 7b). The horizontal line in the middle of the box is the median while the square is the mean. The top and bottom sides of the box represent the Q3 and Q1 quartile (meaning 75th and 25th percentile) of the data set, and the top and bottom whiskers are the 90th and 10th percentile. The maximum and minimum values are also shown as × and ●.

Resistivity measurements were done after sputtering 100 nm silver contact pads onto the silver wires using a Balzers BAE-250 thermal evaporator. Silicon wafer pieces with 700×700 µm^2 square windows were used as stencil masks. The distance between two pads was between 200 and 400 µm. Resistance measurement between the pads was conducted by connecting the sample with a microampere source of 10 µA since it was very important to not generate electrical sintering due to a too high current.[32] The average cross section area of a wire was calculated based on assuming an isosceles triangular shape of a 36° angle from the surface (based on measuring the average angle of 25 cross sections) with the effective width as the surface side. The effective width varied depending on the sintering type and condition, as seen in Figure 3d. The number of individual lines between two pads was counted by SEM, as broken wires had to be ruled out. The average resistivity of an individual wire was calculated by multiplying the measured resistance between the pads by the number of intact lines, taking into account geometrical sizes such as the length of wire and the cross section area.

Conflict of Interest

The authors declare no conflict of interest.

[1] P. B. Catrysse, S. Fan, *Nano Lett.* **2010**, *10*, 2944.
[2] H. Schift, *J. Vac. Sci. Technol., B: Microelectron. Nanometer Struct.–Process., Meas., Phenom.* **2008**, *26*, 458.
[3] H. Schift, *Appl. Phys. A* **2015**, *121*, 415.
[4] T. Borzenko, M. Tormen, G. Schmidt, L. W. Molenkamp, H. Janssen, *Appl. Phys. Lett.* **2001**, *79*, 2246.
[5] X. D. Huang, L. R. Bao, X. Cheng, L. J. Guo, S. W. Pang, A. F. Yee, *J. Vac. Sci. Technol., B: Microelectron. Nanometer Struct.–Process., Meas., Phenom.* **2002**, *20*, 2872.
[6] K. S. Park, B. Cho, J. Baek, J. K. Hwang, H. Lee, M. M. Sung, *Adv. Funct. Mater.* **2013**, *23*, 4776.
[7] J. Jang, B. G. Hyun, S. Ji, E. Cho, B. W. An, W. H. Cheong, J.-U. Park, *NPG Asia Mater.* **2017**, *9*, e432.
[8] S. Hong, H. Lee, J. Lee, J. Kwon, S. Han, Y. D. Suh, H. Cho, J. Shin, J. Yeo, S. H. Ko, *Adv. Mater.* **2015**, *27*, 4744.
[9] P. Kou, L. Yang, C. Chang, S. He, *Sci. Rep.* **2017**, *7*, 42052.
[10] M. Gao, L. Li, Y. Song, *J. Mater. Chem. C* **2017**, *5*, 2971.
[11] G. Grau, J. Cen, H. Kang, R. Kitsomboonloha, W. Scheideler, J. V. Subramanian, *Flexible Printed Electron.* **2016**, *1*, 023002.
[12] Q. Hu, H. Wu, J. Sun, D. Yan, Y. Gao, J. Yang, *Nanoscale* **2016**, *8*, 5350.
[13] K. Fukuda, T. Someya, *Adv. Mater.* **2017**, *29*, 1602736.
[14] D. Xia, A. Biswas, D. Li, S. R. J. Brueck, *Adv. Mater.* **2004**, *16*, 1427.
[15] T. Kraus, L. Malaquin, H. Schmid, W. Riess, N. D. Spencer, H. Wolf, *Nat. Nanotechnol.* **2007**, *2*, 570.
[16] D. Virganavičius, M. Juodėnas, T. Tamulevičius, H. Schift, S. Tamulevičius, *Appl. Surf. Sci.* **2017**, *406*, 136.
[17] R. K. R. Venkata, K. A. Venkata, P. S. Karthik, P. S. Surya, *RSC Adv.* **2015**, *5*, 77760.
[18] FOXIP Project—Functional OXIdes Printed on Polymers and Paper, Strategic Focus Area (SFA) Advanced Manufacturing.
[19] R. Kirchner, H. Schift, *Mater. Sci. Semicond. Process.* **2018**, https://doi.org/10.1016/j.mssp.2018.07.032.

[20] N. Chidambaram, R. Kirchner, R. Fallica, L. Yu, M. Altana, H. Schift, *Adv. Mater. Technol.* **2017**, *2*, 1700018.

[21] K. A. Schroder, S. C. McCool, W. R. Furlan, presented at *NSTI Nanotechnology Conference and Trade Show*, Boston, MA, May **2006**.

[22] K. A. Schroder, presented at *NSTI Nanotechnology Conference & Expo*, Boston, MA, June **2011**.

[23] R. Abbel, T. van Lammeren, R. Hendriks, J. Ploegmakers, E. J. Rubingh, E. R. Meinders, W. A. Groen, *MRS Commun.* **2012**, *2*, 145.

[24] J. West, M. Carter, S. Smith, J. Sears, https://doi.org/10.5772/33519, in *Sintering—Methods and Products* (Ed: V. Shatokha), IntechOpen **2012**.

[25] A. Schleunitz, V. A. Guzenko, M. Messerschmidt, H. Atasoy, R. Kirchner, H. Schift, *Nano Convergence* **2014**, *1*, 7.

[26] D. Dancila, R. Moossavi, J. Siden, Z. Zhang, A. Rydberg, *Microwave Opt. Technol. Lett.* **2016**, *58*, 754.

[27] J. Perelaer, P. J. Smith, D. Mager, D. Soltman, S. K. Volkman, V. Subramanian, J. G. Korvink, U. S. Schubert, *J. Mater. Chem.* **2010**, *20*, 8446.

[28] B. Ingham, T. H. Lim, C. J. Dotzler, A. Henning, M. F. Toney, R. D. Tilley, *Chem. Mater.* **2011**, *23*, 3312.

[29] J. Dryzek, M. Wróbel, E. Dryzek, *Phys. Status Solidi B* **2016**, *253*, 2031.

[30] B. Horváth, *Microelectron. Reliability* **2013**, *53*, 1009.

[31] R. McGill, J. W. Tukey, W. A. Larsen, *Am. Stat.* **1978**, *32*, 12.

[32] M. Hummelgård, R. Zhang, H.-E. Nilsson, H. Olin, *PLoS One* **2011**, *6*, e17209.
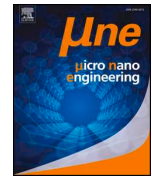
Research paper

Nanoimprint meets microfluidics: Development of metal wires from nanoparticle ink filled capillaries

Barbara Horváth[a], Barbora Křivová[a,b], Helmut Schift[a,*]

[a] Paul Scherrer Institute (PSI), Laboratory for Micro- and Nanotechnology, 5232 Villigen PSI, Switzerland
[b] Palacký University Olomouc, Department of Experimental Physics, 77147 Olomouc, Czech Republic

ARTICLE INFO

ABSTRACT

We demonstrate the use of prepatterned polymer substrates with µm-sized grooves to enhance the low resolution of additive methods such as inkjet and gravure printing by a factor of 10. This enables their use for low cost flexible electronics. Droplets of ink dispersions with < 50 nm Ag nanoparticles with volumes in the nanoliter range were deposited on imprinted receiver pads and drawn into grooves by capillary action in an open-fluidics approach. Using this method, up to 2 mm long, 2 to 5 µm wide wires were created in U- and V-groove capillaries. The characterization of wire thickness before and after sintering revealed that ink supply of the already filled grooves continues from the reservoir during evaporation. By this, higher thickness is achieved than expected from the initial nanoparticle loading, and thus wires with sufficient electrical conductivity are formed.

1. Introduction

Printed electronics uses a range of processes to generate conducting electrical wires, pads or devices such as transistors. There are different strategies to place high resolution silver (Ag) nanowires on surfaces, such as photo-, electron or nanoimprint lithography (NIL) [1] however they require the use of pattern transfer methods (physical vapor evaporation, etching or lift-off) to convert a resist pattern into metallic wires. Inkjet [2] and gravure printing [3,4] are low-cost additive methods used for printed electronics with low resolutions often in the range much larger than 20 µm [5]. In these two cases, after deposition of individual droplets of ink on the surface, either by jetting or by mechanical transfer from wells to a substrate, each droplet assumes the shape given by interaction of the droplet with the surface. This results in a small contact angle on hydrophilic surfaces and thus merging with neighboring droplets, forming a line or area necessary for a transistor, a wire or a connection pad [6]. For electrodes, Ag particle-based inks are used typically with 10 to 50 nm particles dispersed in a suitable solvent [7]. After drying, the nanoparticles merge into a densely packed agglomerated line, and a sintering step is needed to remove organic additives and to convert nanoparticles into grains. During heating a metal wire is formed by diffusion of Ag atoms with conductivity close to bulk Ag. The individual process steps need to be controlled to achieve high resolution, low line etch roughness (LER) and homogeneous thickness.

In order to lower the resolutions of these low-cost processes,

different efforts have been undertaken to shrink dimensions. Either by advancing inkjet technology (using smaller droplet volumes and enhance placement accuracy) or by confining inks by additional means. In the case of inkjet printing, 400 nm wide lines were achieved with 1 µm wide nozzles, using an electrohydrodynamic jet printing setup which is still far from any industrial inkjet head [8,9]. In the case of gravure printing, high-resolution printing below 5 µm was achieved in a roll-to-roll setup with printing speeds on the order of 1 m/s. Also here best results have been obtained by using silicon (Si) wafers as printing plates, which is not a standard material for gravure printing [3,10,11]. Further efforts were undertaken to shrink dimensions of structures to 2 µm [12]. Apart from these developments, another strategy is to pre-pattern the substrate with µm-sized grooves, and to deposit ink with established concepts. In case of nanoimprint assisted inkjet printing [13] sub-µm gaps between Ag electrodes are generated by lift-off of a converted Ag film deposited on an imprinted PMMA film. In cases, when a polymer substrate is patterned by NIL and an ink droplet is much larger than the grooves, it spreads anisotropically on top of the line patterns but also inside grooves [14,15]. The concept is well known in control of wetting behavior and basically relies on the fact that ink spreading can be controlled by surface topography [16,17]. In contrast to this, open microfluidics focuses on ink spreading within capillaries and enables fluid transport over long distances by choosing appropriate solvents, surface energies and topographies [18,19]. Here the aim is that the ink is entirely confined within the grooves and does not wet the

---

surrounding flat surfaces or spill into neighboring grooves. Most surface topographies consist of open channels with vertical sidewalls (for simplicity, here called U-grooves) or with slanted sidewalls which narrow down to the bottom of the channel (V-grooves). These channels exert high pulling forces on the viscous liquid due to Laplace pressure and surface tension and drag them along the capillaries [20]. Such open microfluidics is attractive because of its easy manufacturing (no bonding of lids) and accessibility; however, significant evaporation along channels and the formation of a meniscus forming on top of the liquid has to be taken into account [21].

The method of open microfluidics has already been applied to the fabrication of top-gate thin-film transistors on plastic by using the concept of self-aligned capillarity-assisted lithography [22–24]. A functional liquid ink is deposited into the receivers (landing areas confined by high boundaries) by inkjet printing, and transported into the channels through openings by capillary action. We use a similar approach in the research presented here by pre-patterning the substrate both to control the spreading on surfaces used as receiver pads as, and to transport Ag ink in open grooves. The grooves are fabricated using NIL, either directly in the thermoplastic foils such as poly(ethylene) terephthalate (PET), polyethylene naphthalate (PEN), poly(methyl methacrylate) (PMMA), polycarbonate (PC) or cyclic olefin copolymer (COC), or into a polymer coating layer. Cross linkable materials can be used for this purpose such as Ormocers (inorganic-organic hybrid polymers) which are known for high chemical stability and low surface roughness, and therefore used as "banking" layers for printed electronics. NIL is upscalable to large area and high throughput by using roll-to-plate (R2P) or roll-to-roll (R2R) techniques [1,25–28]. Eventually, paper based printed electronics becomes the goal of low-cost manufacturing [29]. After filling these patterned polymer substrates with Ag ink, a last sintering step is needed where the ink is converted into a solid metallic wire.

The aim is to present a simple concept which goes much below the current > 20 μm resolutions for conventional inkjet printing and even below the 5 μm suitable for open microfluidics. The applications are either electrodes, which are capillaries attached to one contact pad, and wires which connect two contact pads. The questions we were looking for in this research were the following: Up to which length can we fill capillaries with sizes around 2–5 μm, and what is the role of the solvent and its evaporation? How homogeneous is the wire thickness along the capillary? Are U- or V-shaped grooves more favorable to filling and post-processing? These results will help to choose suitable strategies for making transistors, sensors and transparent conductive electrodes by high throughput printing methods.

2. Experimental section

In order to create stamps for nanoimprinting U-grooves, rigid substrates containing inverse U-ridges with vertical sidewalls and flat top were obtained by spincoating a positive resist (Shipley 1805 G2, MicroChem Corp.) on ⟨100⟩ silicon (Si) wafers and prebaked at 115 °C for 90 s. Patterning was done by contact photolithography (365 nm) with a mask with the designed structures on a SÜSS MA6 mask aligner. Then, without postbake, grooves were etched into Si with reactive ion etching (RIE) in an Oxford Plasmalab 100 ICP in a mixture of C_4F_8 5 sccm, and SF_6 23.3 sccm, at a 1250 nm/min etching rate. Stamps to create V-grooves were obtained by initially applying a 100 nm Si_3N_4 film by LPCVD on ⟨100⟩ Si wafers. A negative resist (AZ nLOF 2020, MicroChem) was spincoated on the coated wafers and prebaked at 110 °C for 90 s. Patterning was also done by contact photolithography, and the resist was then postbaked at 110 °C for 120 s. Si_3N_4 was etched by RIE in a mixture of O_2 5 sccm, and CHF_3 40 sccm, at a 100 nm/min etching rate. Potassium hydroxide (KOH)-etching was applied on the exposed Si at 80 °C for 3 min and the Si_3N_4 masking layer removed by RIE. With UV-assisted NIL, the stamp with V-grooves was inverted into working stamp with Λ-ridges.

With these methods, 2.1 μm and 4.9 μm wide, 2 μm deep U-grooves, and 3.1 μm and 5.9 μm wide and 2.2 μm and 4.1 μm deep V-groove lines with an angle of 54.74° between the ⟨100⟩ and the ⟨111⟩ crystalline planes were formed in the silicon wafer surface case from 2 μm and 5 μm lines on the mask, respectively. For the final replication, the stamps with square and Λ-ridges were imprinted into a 150 μm thick poly(methyl methacrylate) (PMMA) (T_g = 105 °C) and a 50 μm thick polycarbonate (PC, T_g = 148 °C) foil using a Jenoptik HEX03 thermal imprint machine. Imprint for 10 min was performed at 180 °C for PMMA and 160 °C for PC at 10 kPa for both materials, demolding at 60 °C. Smart'Ink S-CS01130 dispersions from Genes'Ink, France, in a carrier vehicle of alcohol and alkane with a specified nanoparticle loading of 20 ± 1 w/w% were used (resulting in ~1.4 v/v% concentration). The Ag inks were deposited using a Biospot BT-600 from BioFluidiX or by placing the droplets on the pads manually with a needle. The droplet sizes were between 500 pL – 5 nL volume.

Sintering of the created samples was done on a hotplate with the following heating profile: 3 min heating up to 95 °C, standby for 2 min at 95 °C (for solvent evaporation), then heat up to 150 °C in 5 min (for sintering); keeping at 150 °C for 30 min, then cooling back to room temperature. For height measurements of the deposited Ag nanoparticles, the grooves were analyzed using a confocal laser scanning microscope (CLSM) VK-X1000 from Keyence Corp., Osaka, Japan to determine the homogeneity of the Ag ink before and after sintering in V- and U-grooves. In case of PMMA, we observed thermal reflow, therefore in most cases we chose PC for which sintering did not lead to an apparent change in geometry. Individual defects were observed in optical microscope (OM) and a Zeiss Supra VP55 scanning electron microscope (SEM) at an acceleration voltage of 0.5–1.0 kV. Resistivity measurements were done after voltage was measured by connecting the sample with a microampere source of 10 μA since it was important to not generate electrical sintering due to a too high current [30].

3. Results and discussion

Capillary networks consist of surfaces where macroscopic droplets of a functional liquid can be deposited on and spread. These channels are filled by depositing an ink droplet on the source of the channel without contact by using inkjet printer, or via contact by gravure printing. The ink reception surface at the source of the wires should allow the droplet to spread in a confined area and should serve as a reservoir for filling adjacent fluidic channels. Therefore it is typically hydrophilic or in case of special solvents receptive for that liquid. Since we intend to fabricate wires that are much smaller than the droplet size, we generate pads that serve both as an ink reservoir as source for the capillaries from which the channels are filled but also as electric contact pads (see Fig. 1).

3.1. Capillary filling of single channels

3.1.1. Microcapillaries and open microfluidics

Capillary action has been extensively studied using closed cylindrical microtubes [31]. This approach was used for microfluidic devices with lithographically patterned grooves made by photolithography or replication techniques such as nanoimprint lithography [32]. Filling is achieved by through holes in the lid or by using lateral infiltration of inks or liquids into channels, like with the MIMIC process [33,34]. In open microfluidics, however, the liquid-air interface generates a different boundary condition for capillary transport. By tailoring the size and shape of such channels, fluids can be transported in these channels over long distances, typically much longer than the channel width and can be even used for capillary pumps [35]. For filling channels with metal inks (i.e. solvents loaded with nanoparticles), it is important to fill such channels reliably (defined thickness over wire length and width), without interruptions and shortcuts to neighboring wires after drying. In U-grooves, particularly with flat bottom and vertical
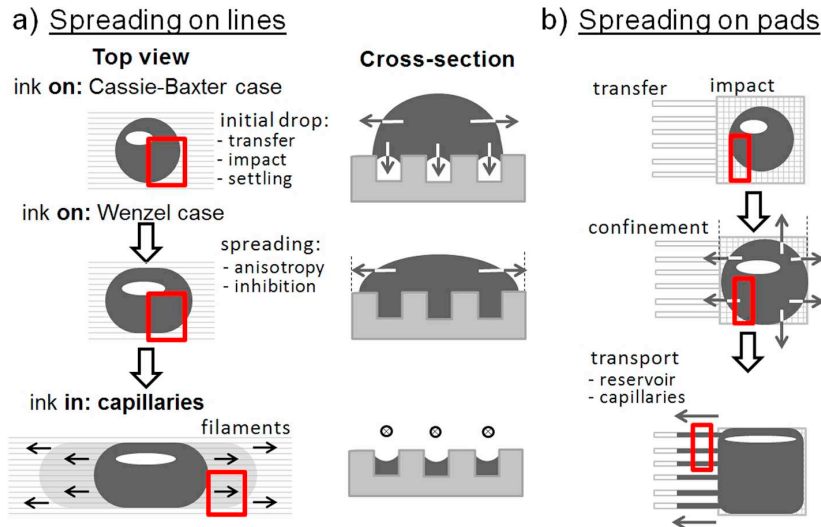
Fig. 1. Concept of droplet deposition on a) prepatterned substrates with cross section and b) analogy with fluidic reservoirs and linked capillaries to be converted into contact pads and wires.

sidewalls, particles tend to accumulate in the corners and connect at the bottom. In V-grooves the nanoparticles sink and accumulate in the bottom vertex resulting in a triangular shaped wire with maximum thickness in the center. Additionally we have observed that wire width reduction is further possible after solvent evaporation in case of inks with extremely low nanoparticle loading [36]. Certain cross-sectional shapes should be maintained along the channel, which might be hampered if significant solvent evaporation happens during the spreading of the nanoparticle dilution, leading to increasing viscosity and starvation of flow.

3.1.2. Wetting of prepatterned substrates

By dispensing of a droplet on top of an array of parallel microcapillaries, the dissipation of kinetic energy enables the liquid to penetrate and fill the trenches. We observed the same wetting states for the nanoparticle inks. There is an immediate transition from the Cassie-Baxter state (where the droplet sits on the capillaries on air pockets) to the Wenzel state (completely wetted surfaces) (Fig. 1). After landing, the droplet immediately begins to spread anisotropically in the direction parallel to the lines due to pinning of the droplet to the groove edges during spreading towards the perpendicular direction. The initial droplet lands on and therefore covers several grooves simultaneously, and then spreads into an extended tubular shape [37]. This is a clear sign that spreading is inhibited laterally and since the drop tries to assume an energetically favorable shape, it spreads along the capillaries until reaches a contact angle assumed by the Wenzel case. The inks used in this research had a very low contact angle on flat surfaces, therefore when placing them on grooves with micrometer period; the contact angles were very low and not measurable.

In our case, since the wetting is very good, we also observe extensions of ink from the droplet continuously flowing in the capillaries beyond the droplet. Fig. 2 shows the spreading of the ink into the capillary trenches at different times after the initial deposition. While the droplet assumes an almost stable shape in longitudinal and lateral dimension, the ink spreads inside the capillaries over several hundreds of μm. Although several groups report similar results of droplets reaching out into the grooves, such long extensions were rarely seen, e.g. in [38]. The extensions are quite frequent if highly favorable wetting conditions occur and evaporation is limited. This is the case for solvent-based Ag inks. While contact angles for water are 87° and 89° on flat PC and PMMA, respectively, 6° is measured for the Smart'Ink S-CS01130 based

on a carrier vehicle of alcohol and alkane. Similarly, extensions reported by Brinkman et al. were induced by electrowetting, but retracted due to the Laplace pressure if the electric field is switched off [39].

Since the ink in the capillaries does not obey the rules of surface energy conservation of the large droplet, it advances until it reaches a second equilibrium of the open capillary. The droplet on one end, now acting as a reservoir, is typically much larger than the volume of the capillary to be filled, therefore provides an almost unlimited supply of ink. Therefore, as long as the wetting in the channels allows the liquid supply to be continuous, the ink advances in the channel without wetting the surfaces outside of the trench. Only when solvent evaporation in the capillary becomes significant the spreading starves along the capillary, leading to particles depositing on the bottom and sidewalls of the grooves during drying.

In order to achieve a homogeneous wetting of a receiver pad that serves as a reservoir for extensions, we dispensed ink on top of an array of parallel microcapillaries that has been designed to help confining and spreading the ink droplet (Fig. 3a). The structures enable ink transport towards the capillary or capillaries attached to the reservoir, and the ink proceeds into the trench without overspill. Furthermore the placement accuracy does not have a strong influence on the filling of the capillary (Fig. 3c), as soon as a small portion of the droplet touches the reservoir, the ink will be directed to the exit trench due to the design of the pad with guiding lines.

In Fig. 3b, it can be seen for 5 μm wide U-grooves printed in PC that identical spreading lengths of about 700 μm were achieved independent from the amount of liquid placed on the structured square receivers. The amount of ink filled in the reservoir has no influence on the spreading, as long as it is not depleted before the ink would stop spreading in the U-groove. An identical spreading length was achieved for arrow-shaped pads (see Fig. 3c), which was designed for directed flow of ink towards the tip. The ink droplet volumes were typically in the range of 1 nL that results in spherical droplet of 0.12 mm diameter, fitting well for the $500 \times 500 \, \mu m^2$ receiver pads. The receiver pads work both for U-groove and V-groove topographies and for the attached capillaries of the same shape.

3.1.3. Spreading in single capillaries

For closed cylindrical channels, capillary-driven flow is well-described by the classical Washburn equation [40]. It balances the driving force provided by the decrease in free energy as the fluid wets the walls
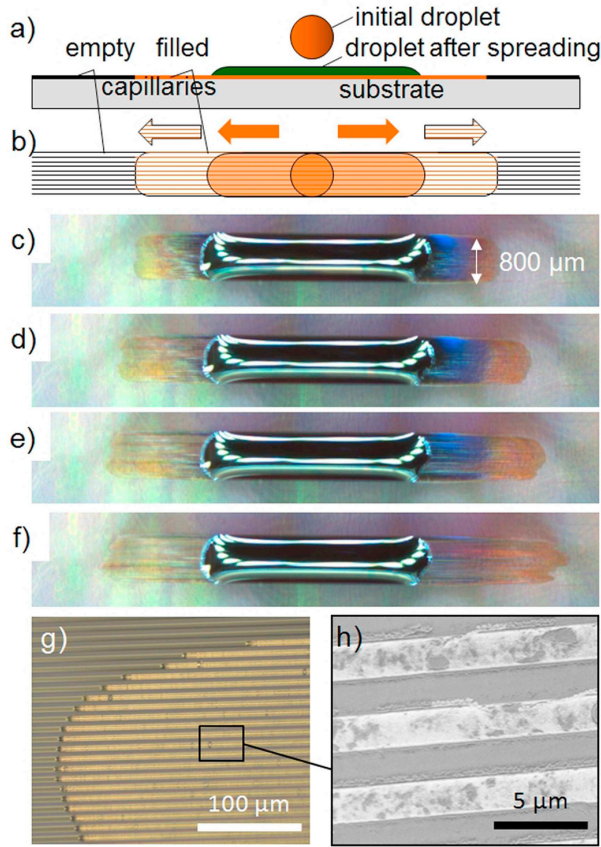
Fig. 2. Schematics (a, b) and optical micrographs (c–g) of spreading of ink droplets in pre-patterned substrates with U-grooves: (a, b) Schematics and (c–f) optical micrographs of an elongated droplet 16, 28, 40 and 70 s after initial deposition (0 s, not captured) where the central part (dark) is the area of the droplet covering the entire surface and on the sides (light) is the spreading of ink within the capillaries. Period 10 μm, width 5 μm, depth 2 μm. g) Magnification of the end after sintering. h) SEM micrograph with a close up of the sintered wires.

of the channel against the viscous drag of the liquid. For capillary flow in a circular capillary tube, (1) provides an analytical solution:

$$x^2 = \frac{D \cdot cos\theta}{4} \cdot \frac{\gamma}{\mu} \cdot t, \tag{1}$$

where x is the liquid penetration length in the tube, D is the tube diameter, γ and μ are the liquid surface tension and the viscosity, θ is the static contact angle characterizing the liquid/solid interaction at their interface. The Washburn's equation is valid when the capillary force is balanced only by the viscous force, which is true after the momentum associated with the initiation of the capillary flow dissipates away. Therefore, only Poiseuille flow and static advancing contact angles are assumed. Deviations from the Washburn equation have been observed in capillary flow, especially at short time-scales. Theoretical studies have shown that in early stages of capillary flow inertial effects dominate leading to $x \sim t^2$ followed by $x \sim t$, while at later stages, these effects are negligible and the dependence $x^2 \sim t$ is observed.

Open microfluidics has been extensively investigated by Yang et al. [41] for different groove geometries. The presented simulations are showing a common agreement between closed and open capillaries, and a general Eq. (2) was found to describe the liquid penetration x in these capillaries, where C is a function of the groove size, shape, and contact angle.
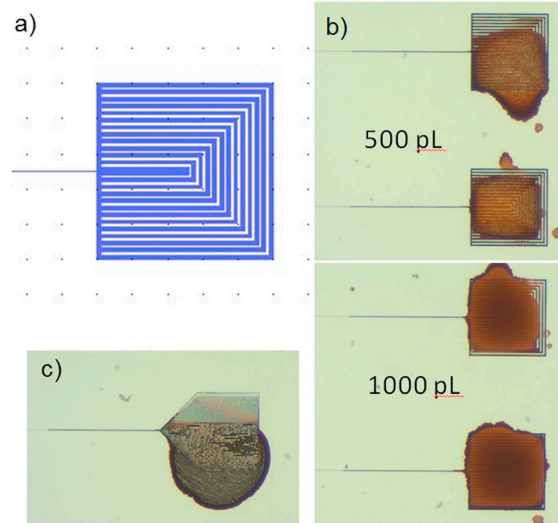

Fig. 3. Design a) and optical micrographs (b, c) of receiver pad for spreading and confining ink droplets with a single capillary attached, here about 700 μm in 5 μm wide U-grooves printed in PC. b) Square receiver pads (500 × 500 μm²). c) Arrow-shaped receiver pad with an ink droplet placed with low accuracy.

$$x^2 = C \cdot (\gamma/\mu) \cdot t \tag{2}$$

However, for non-circular capillaries C cannot be calculated in a straightforward way. Open capillaries with certain groove shapes with constant cross-section, e.g. wedges with flattened bottom or U-shaped or rounded shapes do lead to these simple flow kinetics and are more difficult to calculate than V-grooves [42]. Corner flow (or edge wetting) becomes significant in a capillary with multiple edges at low contact angles ($< 30°$) and can significantly precede bulk flow in the microchannel depending on channel aspect ratio [43]. Rye et al. [44] conducted experiments of capillary flow in V–shaped grooves, featuring a geometry with a single vertex, where they found that C can be expressed as (3).

$$C = K(\alpha, \theta) \cdot h_0 \tag{3}$$

where h_0 is the groove height, $K(\alpha, \theta)$ is a shape dependent parameter with α being the vertical angle of the groove. Chen has presented the hypothesis (4) that a non-circular cross section has an equivalent diameter.

$$D_{eq} = L_{contact}/\pi \tag{4}$$

with $L_{contact}$ the contact line length at the air/liquid/solid interface. For a circular tube, the equivalent diameter is the actual tube diameter, and the contact line length is the corresponding circumference [45]. For V-grooves, the following formula (5) is valid.

$$K(\alpha, \theta) = [(cos\theta - cos\alpha)/2\pi \cdot sin\alpha] \tag{5}$$

And for other geometries, he referred to another study, by Rye et al. [46], who showed (6) that.

$$C = (S \cdot cos\theta - w)/4\pi \tag{6}$$

with w being the groove width at its opening and S being the total arc length of the groove on a plane perpendicular to the groove axis. This would apply for shapes with square, trapezoid or rounded shapes (see Fig. 4). These calculations are often for microcapillaries in a typical microfluidic device with several 10 μm wide channels. We are here however presenting results for the channels with 2.1 μm width and for typical solvents used for Ag nanoparticles inks.

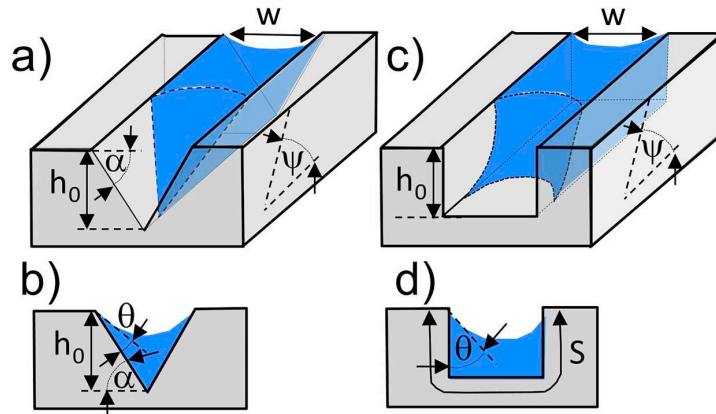For grooves with V- shape, using the contact angle $\theta = 6°$ for the Ag

Fig. 4. Groove geometries and liquid spreading characteristics for a) V-grooves and b) U-grooves with flat bottom.

ink on PMMA and PC, and a silicon groove opening ($\alpha = 54.74°$, resulting in a groove vertex angle of 70.52°) of w = 3.1 μm (resulting in a depth $h_0 = 2.2$ μm), we can calculate from (1), (3) and (5) C = 0.18 μm and (4) $D_{eqV} = 0.71$ μm. By using formula (6) with the arc length, we calculate $D_{eqVarc} = 0.72$ μm, which is in accordance with the former calculation. It has to be noted that the first formula is only valid for small θ (with a convex meniscus) and does not give sound results for e.g. water with a contact angle of 89° on PC. Therefore, results only give very rough indication about filling speeds.

For the U-grooves tested in this work, with an approximation of the liquid penetration front profile shown in Fig. 4b and the contact line length of $L_{contact} = w_U + 2·h_U/\sin45°$, and for 2.1 μm wide and 2.0 μm deep rectangular channels, this would result in an equivalent diameter (4) $D_{eqU} = 2.5$ μm, which is much larger than that of the V-groove with 3.1 μm opening but only 78% of the cross-sectional area. The $\psi = 45°$ stem from the fact that the meniscus advances with measured tilt angle of the meniscus plane. Using the data sheet values for the Smart'Ink S-CS01130 dispersion (for 20 °C) we calculated filling speeds in Table 1. The main conclusion is that while the U-groove a 0.4 mm long channel is filled already after 0.1 s, for a V-groove it takes 10 times longer. However, for larger grooves in the experiment, and for reasons we explain later, differences are difficult to observe experimentally.

3.1.4. Filling homogeneity of V- and U-grooves

The capillary is designed to be filled in a controlled way due to the confining properties of the patterned reservoir pads. If excess material on the pads need to be avoided (e.g. for restrictions of roughness in further process steps), the droplet volume needs to be adapted to the available pad volume. The capillary volume of a 500×500 μm^2 large,

Table 1

Spreading in single open capillaries according to Washburn Eq. (1) with equivalent tube diameters and estimated capillary filling speeds for two channel geometries and widths using (5) for V-grooves and (6) for the U-grooves. The comparison was made for Smart'Ink S-CS01130 dispersions with a specified nanoparticle loading of 20 ± 1 w/w% and surface tension $\gamma = 29 \pm 3$ mN/m and viscosity $\eta = 13 \pm 3$ mPa·s given in the supplier's data sheets, resulting in $\gamma/\eta = 2.23$ m/s, and a measured contact angle of $\theta = 6°$ on PMMA and PC.

Groove w/h	μm/μm	V 3.1/2.2	V 5.9/4.1	U 2.1/2.0	U 4.9/2.0
C	μm	0.18	0.33	0.61	0.84
D_{eq}	μm	0.71	1.33	2.45	3.38
x (t)					
0.1 s	mm	0.20	0.27	0.37	0.43
1.0 s	mm	0.40	0.74	1.37	1.86
10.0 s	mm	2.00	2.73	3.70	4.31

2 μm deep pad is 250 times larger, a 100×100 μm^2 pad is 10 times larger than a 0.5 mm long, 2 μm wide and 2 μm deep single rectangular capillary. This volume is further reduced if the pad is internally patterned, (i.e., only 50% area consists of capillaries) or if several capillaries are attached to one pad, and the ink volume available for spreading could get close to the volume remaining in the pad. Nevertheless, the Laplace pressure of a small droplet (due to the small radius of curvature) is very small, and even smaller for a structured pad.

In Fig. 5, the filling of a single U-shaped capillary is shown. The height of the filling is initially 1.5 μm and reduces to 1.0 μm after 480 μm to the right, where it abruptly stops. However, from the nanoparticle load aspect assuming a capillary that is only filled with ink with the volume of the trench, taking a ~1.4 v/v% nanoparticle concentration and assuming a homogeneous coverage of the bottom, a 2 μm deep U-groove should be deposited with a 30 nm thick Ag film, which is in the range of the initial Ag nanoparticle size. The fact that we have > 1 μm wire thickness up to the point where the ink stopped means that more liquid ink is transported continuously along the capillary from the reservoir pad during the evaporation of the solvent. The evaporation at the open surface of the liquid inside the channel induces a convective flow of ink from the reservoir, until the particles concentrate to form a densely packed metallic deposit starting at the end of the channel and propagating all the way back to the reservoir [21,47].

Calculation of filling speeds only gives rough estimates, which coincide with the observations of filling times made in fractions of seconds. In comparison to the larger capillaries used until now in the cited literature, we are in a regime where speed seems to be in a range which makes filling observable (0.4 mm in 1 s for V-grooves). However, in contrast to the $x^2 \sim t$ relation given by the Washburn equation, filling does not just slow down but stops abruptly and the liquid front does not continue to advance. The liquid supply from the reservoir of the already filled grooves continues during evaporation. If the filling can be re-supplied, then the thickness of this layer can be increased. Therefore, it is probable that with the channel sizes we are currently using, evaporation is in the same time range as filling. Currently it is difficult to say whether much smaller channels, for which particle sizes would become more critical, would enable faster drying while filling would slow down. In contrast to this, larger channels would fill faster, and ink would take more time to dry.

3.1.5. Maximum filling lengths of V- and U-grooves with different widths

Multiple pads were filled to determine the spreading abilities of different shaped grooves depending on the substrate material. Single U- and V-grooves joining an arrow shaped pad were examined. The average spreading (from approx. 40 samples per condition) can be seen
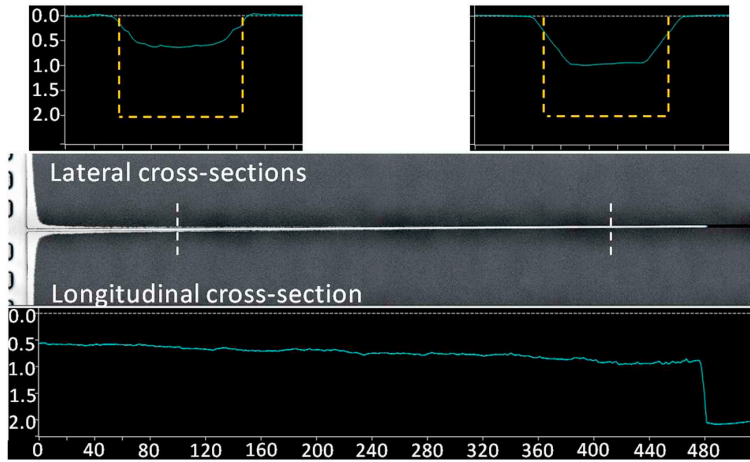
Fig. 5. CLSM micrograph and analysis of the Ag wire height along a ~500 μm long 2.1 μm wide and 2.0 μm deep U-groove in PMMA, filled with Ag nanoparticle ink from the reservoir from the left before sintering, resulting in a thick layer of loosely assembled nanoparticles. Dashed yellow lines indicate lateral U-groove cross-sections. (For interpretation of the references to colour in this figure legend, the reader is referred to the web version of this article.)

in the graphic in Fig. 6. The deviation was calculated after measuring the spreading length of every filled groove where no early spreading stop (e.g., due to embossing errors) were observed. For the wider channels, a length of ~500 μm can be filled with both U- and V-grooves,

and for both PC and PMMA. For the narrower channels, a length of > 300 μm can be filled for U-grooves in PC and PMMA, but only ~200 μm for the V-grooves. U-grooves generally have better spreading abilities than V-grooves due to their larger surface areas; Ag ink spreads
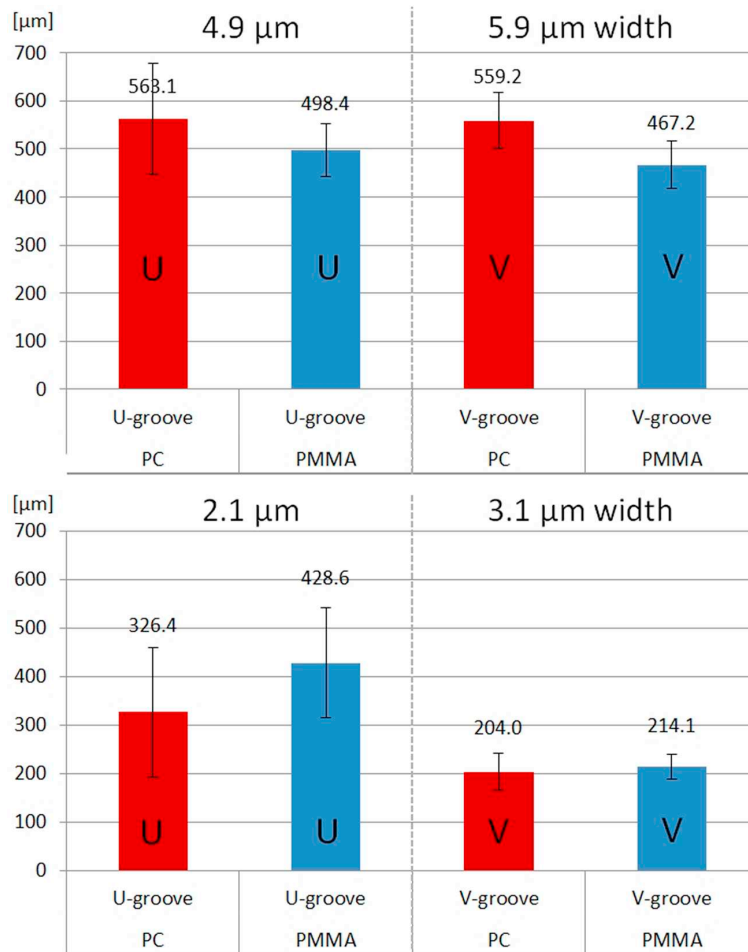

Fig. 6. Experimental analysis of the average spreading using optical micrographs. Multiple capillaries that were filled from receiving pads to determine the spreading abilities of different groove shapes depending and substrate materials. Shape and widths are indicated in the graph.
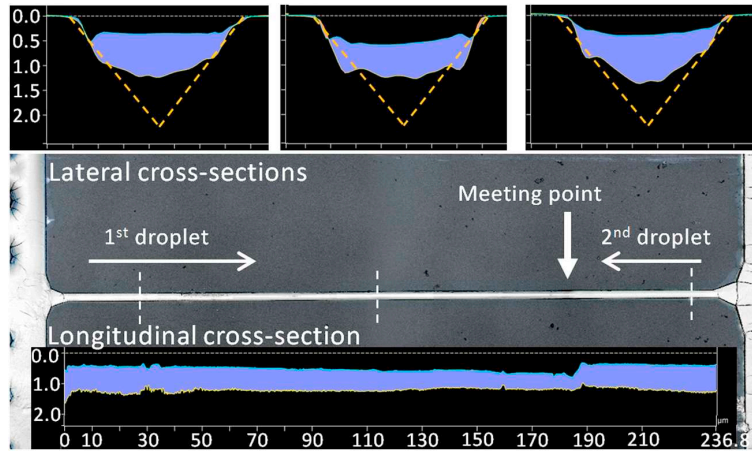
Fig. 7. CLSM micrographs of a 3.1 μm wide, 235 μm long V-groove filled from both sides, before and after sintering. Lateral V-groove cross-sections are indicated by dashed yellow lines. The blue area is the difference between the dried and sintered state. (For interpretation of the references to colour in this figure legend, the reader is referred to the web version of this article.)

1.5 and 2 times further in a U-groove in case of PC and PMMA material, respectively. The Ag ink spreads further on PMMA than PC in case of similar groove geometries, i.e., 39% and 7% further in U- and V-grooves, respectively.

The maximum spreading length has also to be taken into account for wires that are filled from both sides. In Fig. 7 a V-groove in PC with 235 μm length can be seen, which has been filled first from the left (1st droplet) and then the right (2nd droplet) side. The upper lines of the longitudinal and lateral cross-sections are valid for the non-sintered case, the V-groove shape is indicated by dashed yellow lines. Similarly to the U-grooves, the higher thickness can only be explained by a continuous filling from the reservoir, while drying of the ink goes on. Taking a 2.2 μm deep V-groove, initially the left side has a thickness of 1.8 μm and a constant thinning of ink is visible towards the right achieving a minimum value of 1.6 μm at about 20% from the right. From the right side, the height is almost constant at 1.9 μm. Additional to the decrease, a sharp decrease down to ~1.4 μm can be observed at the meeting point (but no interruption). We interpret the decreasing as the meeting point of the liquid flows. The filling from the left stopped abruptly (similarly as seen in Fig. 5), and acted as a barrier for the ink coming in from the right side. In many cases, the meeting point for the inks is visible coming from the two ends of the channels. If the channel length is less than twice the size of the average spreading, the meeting point will most probably move towards the end of the channel where the second ink droplet was placed (due to filling multiple pads there was usually over 30 s difference between placing droplets on the two ends).

3.2. Sintering self-assembled Ag nanoparticles into wires

Sintering is a process in which the nanoparticles merge by applying heat below the melting point. Adjacent particles partially coalesce due to diffusion and consequently the thickness decreases while the total surface area remains constant. During the heating process the solvent evaporates, organic coatings surrounding the individual nanoparticles are removed and the nanoparticles sinter into grains. This shrinkage determines the remaining thickness.

The homogeneity of the Ag ink was analyzed before and after sintering in V-grooves, and the shrinkage involved during the sintering step. This was compared to the geometry of the empty groove. Using this, we determined the degree of filling over the entire channel length. PC was used as a substrate, since PMMA is thermally reflowed at 150 °C thermal sintering and thus can compromise the shrinkage measurement. As discussed before, we can see in Fig. 7 that there is a thinning of the Ag nanoparticle layer from the left reservoir to distance of about

190 μm, which remains visible after sintering. The blue area is the height difference between the dried and sintered state indicated by the upper and lower line in the longitudinal and lateral cross-sections. At the middle of the capillary (at ~120 μm distance from both sides), the wire height in the center of the V-groove is reduced from 2.2 μm to ~1.6 μm before and to ~1.0 μm after sintering, which becomes almost constant over the entire capillary. The average volume of the V-groove was reduced to ~50% after drying and to ~20% after sintering, which is > 10 times larger than the expected volume reduction. The resulting wire is almost triangular-shaped with a concave meniscus.

By taking into account the minimum length of filling (depending on geometry, roughness, viscosity, wetting, corners and roughness/defects in a channel) we can either create open end electrodes by filling from one side, or fill from both sides to create wires between two pads. In the same way, we are able to create arrays of wires, (e.g. for heating devices) or interrupted wires (e.g. for capacitors and sensing). Fig. 8 shows an example of a double Ag wire with 5 μm distance between each other. Droplets were placed on four pads serving as reservoirs for capillary filling. Magnification shows that 5 μm wide trenches with 5 μm distance were filled without electrical connection between each other. Resistance was measured to be 37 Ω for an estimated Ag thickness of
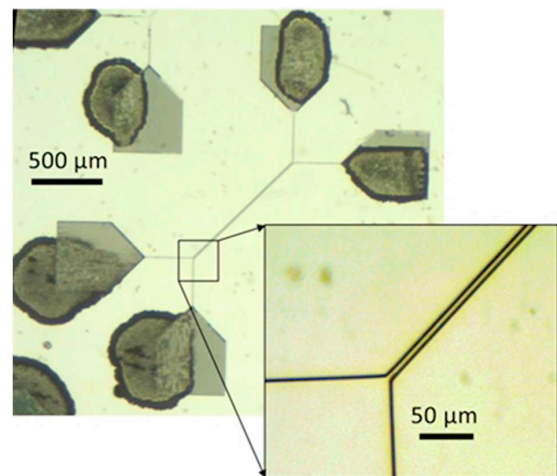

Fig. 8. Optical micrograph of a 2 mm long double line filled with Ag after filling two trenches from two sides each.

500 nm with U-grooves, which results in a resistivity of 4.6×10^{-8} Ωm, similar to the data provided by the ink supplier. Low placement precision of the droplet on the landing pad proved to be unproblematic and did not inhibit the filling, due to the self-assembling structure inside the reservoirs.

4. Conclusion

Open microfluidics is a viable approach to use low-resolution additive techniques in combination with prepatterned substrates. Different design elements were proven to be useful: Patterned landing pads which spread impinging ink and serve as reservoirs for capillary filling, capillaries with both U- and V-shapes which can be filled from one or both sides. Here, dynamic filling and drying enables to fill grooves to a higher level than that given by calculation of a static case taking into account a specific weight ratio of nanoparticles in the solvent. PMMA and PC were examined as substrates but results should be easily transferable to other materials such as PET and PEN, and Ormocer planarization layers. Since adjacent channels can be filled with no overspill, single electrodes can be used for interdigitated electrode arrays (IDEAs), or wire arrays for heating elements. The overall observations show that basic rules are valid for filling of capillaries with well-wetting inks, but the deposition of nanoparticles in the channels during and after filling have to be taken into account. The conductive wires are only formed during a sintering step, for which grain growth and possible deformation of the polymer substrate has to be considered. Overall, open microfluidics is a valid approach for shrinking dimension in printed electronics and reasonable wire lengths can be patterned for channel widths in the micrometer range.

Patent information

European Patent Application No. 18173943.4-1022, filed on 24 May 2018.

Acknowledgements

References

[1] H. Schift, Nanoimprint lithography: an old story in modern times? A review, J. Vac. Sci. Technol. B 26 (2) (2008) 458–480 (Measurement, and Phenomena).

[2] M. Gao, L. Li, Y. Song, Inkjet printing wearable electronic devices, J. Mater. Chem. C 5 (12) (2017) 2971–2993.

[3] G. Grau, J. Cen, H. Kang, R. Kitsomboonloha, W. Scheideler, J.V. Subramanian, Gravure-printed electronics: recent progress in tooling development, understanding of printing physics, and realization of printed devices, Flex. Print. Electron. 1 (2) (2016) 023002.

[4] Q. Hu, H. Wu, J. Sun, D. Yan, Y. Gao, J. Yang, Large-area perovskite nanowire arrays fabricated by large-scale roll-to-roll micro-gravure printing and doctor blading, Nanoscale 8 (9) (2016) 5350–5357.

[5] K. Fukuda, T. Someya, Recent Progress in the development of printed thin-film transistors and circuits with high-resolution printing technology, Adv. Mater. 29 (25) (2016) 2016 736.

[6] J. Perelaer, P.J. Smith, D. Mager, D. Soltman, S.K. Volkman, V. Subramanian, J.G. Korvink, U.S. Schubert, Printed electronics: the challenges involved in printing devices, interconnects, and contacts based on inorganic materials, J. Mater. Chem. 20 (39) (2010) 8446–8453.

[7] R.K.R. Venkata, K.A. Venkata, P.S. Karthik, P.S. Surya, Conductive silver inks and their applications in printed and flexible electronics, RSC Adv. 5 (95) (2015) 77760–77790.

[8] Z. Yin, Y. Huang, N. Bu, X. Wang, Y. Xiong, Inkjet printing for flexible electronics:

[9] B.H. Kim, M.S. Onses, J.B. Lim, S. Nam, N. Oh, H. Kim, K.J. Yu, J.W. Lee, J.-H. Kim, S.-K. Kang, C.H. Lee, J. Lee, J.H. Shin, N.H. Kim, C. Leal, M. Shim, J.A. Rogers, High-resolution patterns of quantum dots formed by electrohydrodynamic jet printing for light-emitting diodes, Nano Lett. 15 (2) (2015) 969–973.

[10] R. Kitsomboonloha, S.J.S. Morris, X. Rong, V. Subramanian, Femtoliter-scale patterning by high-speed, highly scaled inverse gravure printing, Langmuir 28 (48) (2012) 16711–16723.

[11] H. Kang, R. Kitsomboonloha, K. Ulmer, L. Stecker, G. Grau, J. Jang, V. Subramanian, Megahertz-class printed high mobility organic thin-film transistors and inverters on plastic using attoliter-scale high-speed gravure-printed sub-5μm gate electrodes, Org. Electron. 15 (12) (2014) 3639–3647.

[12] G. Grau, R. Kitsomboonloha, V. Subramanian, Fabrication of a high-resolution roll for gravure printing of 2μm features, SPIE Org. Photon. + Electron. (2015) 8 SPIE.

[13] L. Teng, M. Plötner, A. Türke, B. Adolphi, A. Finn, R. Kirchner, W.-J. Fischer, Nanoimprint assisted inkjet printing to fabricate sub-micron channel organic field effect transistors, Microelectron. Eng. 110 (2013) 292–297.

[14] Y. Chen, B. He, J. Lee, N.A. Patankar, Anisotropy in the wetting of rough surfaces, J. Colloid Interface Sci. 281 (2) (2005) 458–464.

[15] X.-M. Li, D. Reinhoudt, M. Crego-Calama, What do we need for a superhydrophobic surface? A review on the recent progress in the preparation of superhydrophobic surfaces, Chem. Soc. Rev. 36 (8) (2007) 1350–1368.

[16] K.J. Kubiak, T.G. Mathia, Anisotropic wetting of hydrophobic and hydrophilic surfaces–modelling by lattice Boltzmann method, Procedia Eng. 79 (2014) 45–48.

[17] P. Gravesen, J. Branebjerg, O.S. Jensen, Microfluidics-a review, J. Micromech. Microeng. 3 (4) (1993) 168.

[18] M. Zimmermann, S. Bentley, H. Schmid, P. Hunziker, E. Delamarche, Continuous flow in open microfluidics using controlled evaporation, Lab Chip 5 (12) (2005) 1355–1359.

[19] J.B. Berthier, A. Kenneth, Berthier, Erwin Open Microfluidics, Scrivener Publishing LLC. John Wiley & Sons Inc, 2016.

[20] L. Tie, Z. Guo, W. Liu, Anisotropic wetting properties on various shape of parallel grooved microstructure, J. Colloid Interface Sci. 453 (2015) 142–150.

[21] S. Lone, J.M. Zhang, I.U. Vakarelski, E.Q. Li, S.T. Thoroddsen, Evaporative lithography in open Microfluidic Channel networks, Langmuir 33 (11) (2017) 2861–2871.

[22] W.J. Hyun, E.B. Secor, F.Z. Bidoky, S.B. Walker, J. Lewis, A.M. Hersam, C.L. Francis, F.C.D. Frisbie, Self-aligned capillarity-assisted printing of top-gate thin-film transistors on plastic, Flex. Print. Electron. 3 (3) (2018) 035004.

[23] W.J. Hyun, F.Z. Bidoky, S.B. Walker, J.A. Lewis, L.F. Francis, C.D. Frisbie, Printed, self-aligned side-gate organic transistors with a Sub-5 μm Gate–Channel distance on imprinted plastic substrates, Adv. Electron. Mater. 2 (12) (2016) 1600293.

[24] A. Mahajan, W.J. Hyun, S.B. Walker, G.A. Rojas, J.-H. Choi, J.A. Lewis, L.F. Francis, C.D. Frisbie, A self-aligned strategy for printed electronics: exploiting capillary flow on microstructured plastic surfaces, Adv. Electron. Mater. 1 (9) (2015) 1500137.

[25] H. Schift, Nanoimprint lithography: 2D or not 2D? A review, Appl. Phys. A Mater. Sci. Process. 121 (2) (2015) 415–435.

[26] S.H. Ahn, L.J. Guo, Large-area roll-to-roll and roll-to-plate nanoimprint lithography: a step toward high-throughput application of continuous nanoimprinting, ACS Nano 3 (8) (2009) 2304–2310.

[27] A. Schleunitz, C. Spreu, T. Mäkelä, T. Haatainen, A. Klukowska, H. Schift, Hybrid working stamps for high speed roll-to-roll nanoreplication with molded sol–gel relief on a metal backbone, Microelectron. Eng. 88 (8) (2011) 2113–2116.

[28] M. Leitgeb, D. Nees, S. Ruttloff, U. Palfinger, J. Götz, R. Liska, M.R. Belegratis, B. Stadlober, Multilength scale patterning of functional layers by roll-to-roll ultra-violet-light-assisted nanoimprint lithography, ACS Nano 10 (5) (2016) 4926–4941.

[29] X. Li, D.R. Ballerini, W. Shen, A perspective on paper-based microfluidics: current status and future trends, Biomicrofluidics 6 (1) (2012) 011301.

[30] M. Hummelgård, R. Zhang, H.-E. Nilsson, H. Olin, Electrical sintering of silver nanoparticle ink studied by in-situ TEM probing, PLoS One 6 (2) (2011) e17209.

[31] R. Lucas, Ueber das Zeitgesetz des kapillaren Aufstiegs von Flüssigkeiten, Kolloid-Zeitschrift 23 (1) (1918) 15–22.

[32] F.F. Ouali, G. McHale, H. Javed, C. Trabi, N.J. Shirtcliffe, M.I. Newton, Wetting considerations in capillary rise and imbibition in closed square tubes and open rectangular cross-section channels, Microfluid. Nanofluid. 15 (3) (2013) 309–326.

[33] E. Kim, Y. Xia, G.M. Whitesides, Micromolding in capillaries: applications in materials science, J. Am. Chem. Soc. 118 (24) (1996) 5722–5731.

[34] C.R. Martin, I.A. Aksay, Microchannel molding: a soft lithography-inspired approach to micrometer-scale patterning, J. Mater. Res. 20 (8) (2005) 1995–2003.

[35] D. Juncker, H. Schmid, U. Drechsler, H. Wolf, M. Wolf, B. Michel, N. de Rooij, E. Delamarche, Autonomous microfluidic capillary system, Anal. Chem. 74 (24) (2002) 6139–6144.

[36] B. Horváth, B. Křivová, S. Bolat, H. Schift, Fabrication of large area sub-200 nm conducting electrode arrays by self-confinement of spincoated metal nanoparticle inks, Adv. Mater. Technol. 4 (3) (2019) 1800652.

[37] D. Xia, L.M. Johnson, G.P. López, Anisotropic wetting surfaces with one-Dimensional and directional structures: fabrication approaches, wetting properties and potential applications, Adv. Mater. 24 (10) (2012) 1287–1302.

[38] D. Xia, S.R.J. Brueck, Strongly anisotropic wetting on one-dimensional nano-patterned surfaces, Nano Lett. 8 (9) (2008) 2819–2824.

[39] M. Brinkmann, R. Lipowsky, Wetting morphologies on substrates with striped surface domains, J. Appl. Phys. 92 (8) (2002) 4296–4306.

[40] E.W. Washburn, The dynamics of capillary flow, Phys. Rev. 17 (3) (1921) 273–283.

[41] D. Yang, M. Krasowska, C. Priest, M.N. Popescu, J. Ralston, Dynamics of capillary-driven flow in open microchannels, J. Phys. Chem. C 115 (38) (2011) 18761–18769.

materials, processes and equipments, Chin. Sci. Bull. 55 (30) (2010) 3383–3407.

[42] L.A. Romero, F.G. Yost, Flow in an open channel capillary, J. Fluid Mech. 322 (2006) 109–129.

[43] A. Olanrewaju, M. Beaugrand, M. Yafia, D. Juncker, Capillary microfluidics in microchannels: from microfluidic networks to capillaric circuits, Lab Chip 18 (16) (2018) 2323–2347.

[44] R.R. Rye, F.G. Yost, J.A. Mann, Wetting kinetics in surface capillary grooves, Langmuir 12 (20) (1996) 4625–4627.

[45] T. Chen, Capillary force-driven fluid flow in open grooves with different sizes, J. Thermophys. Heat Transf. 29 (3) (2015) 594–601.

[46] R.R. Rye, F.G. Yost, E.J. O'Toole, Capillary flow in irregular surface grooves, Langmuir 14 (14) (1998) 3937–3943.

[47] L. Malaquin, T. Kraus, H. Schmid, E. Delamarche, H. Wolf, Controlled particle placement through convective and capillary assembly, Langmuir 23 (23) (2007) 11513–11521.

[48] FOXIP-Project, Functional OXIdes Printed on Polymers and Paper, within the Program of the Strategic Focus Area (SFA) Advanced Manufacturing, https://www.sfa-am.ch/foxip.html.